Bernhard Kretz, BSc

Wave-function tuning in self-assembled monolayers

MASTER THESIS

For obtaining the academic degree
Diplom-Ingenieur

Master Programme of
Technical Physics

Graz University of Technology

Supervisor:

Ao.Univ.-Prof. Dipl.-Ing. Dr.techn. Egbert Zojer

Institute of Solid State Physics

Graz, March 2014

Deutsche Fassung:
Beschluss der Curricula-Kommission für Bachelor-, Master- und Diplomstudien vom 10.11.2008
Genehmigung des Senates am 1.12.2008

EIDESSTATTLICHE ERKLÄRUNG

Ich erkläre an Eides statt, dass ich die vorliegende Arbeit selbstständig verfasst, andere als die angegebenen Quellen/Hilfsmittel nicht benutzt, und die den benutzten Quellen wörtlich und inhaltlich entnommenen Stellen als solche kenntlich gemacht habe.

Graz, am …… ……..
(Unterschrift)

Englische Fassung:

STATUTORY DECLARATION

I declare that I have authored this thesis independently, that I have not used other than the declared sources / resources, and that I have explicitly marked all material which has been quoted either literally or by content from the used sources.

…… ……..
date (signature)

Acknowledgments

I would like to thank my supervisor **Egbert Zojer** for kindly and patiently supporting me during my thesis, for all his ideas and for introducing me to scientific work.

David Egger taught me how to do scientific simulations properly, always patiently answered my questions and helped me with my problems. For all this I would like to thank him very much.

I would also like to thank my parents, **Klaudia** and **Richard**, for their support, financial and otherwise, during my studies.

For some very interesting and fruitful discussions and a lot of inspiring coffee breaks I would like to thank all the colleagues from my group (including former members, in random order): **David Egger**, **Elisabeth Wruss**, **Veronika Obersteiner**, **Manuel Vieider**, **Gernot Kraberger**, **Elisabeth Verwüster**, **Iris Hehn** and **Thomas Taucher**.

Tomáš Bučko from the *University of Bratislava* was a great help with the GADGET geometry optimizations.

Financial support by the **Austrian Science Fund (FWF)**: I937-N19

For providing computational resources and support for the simulations I would like to thank the **ZID** of the *TU Graz*.

Abstract

Self-assembled monolayers (SAMs) play an important role in the field of molecular electronics, since they posses the ability to tune the performance of electronic devices. During the last years, the potential of SAMs utilizing dipolar functional groups in terms of work-function modifications has been demonstrated. It has also been shown that the embedding of dipolar groups within the backbone of a SAM leads to the formation of a dipole layer, which causes energetic shifts of the orbitals above and below this layer relative to each other.

In this work, band structure calculations based on density functional theory were performed on different SAMs using the VASP code. Dipolar groups were distributed along the backbones of these SAMs. Difference influences on the localization of orbitals and on orbital shifts were investigated. Examples for investigated influences are structural, collective and interface effects. On base of the insight gained by this investigations, a way towards the engineering of organic molecular quantum-wells was pointed out for one of the used backbone molecules.

A variety of molecules with different backbones were investigated in order to determine the influence of the chemical structure on orbital localizations and energetic shifts. Additionally, the impact of different dipolar groups, conjugated and non-conjugated, were investigated.

The suitability of a spacer group for reducing the influence of the metal substrate on the monolayer was determined. Other spacer units were distributed within the backbone to identify their influence on the localization of the frontier orbitals.

Finally, monolayers that posses a magnetic moment due to doping with open shell atoms were investigated.

Kurzfassung

Im Bereich der molekularen Elektronik haben selbstorganisierte Monolagen (SAMs) große Bedeutung erlangt, da mit ihrer Hilfe die Eigenschaften von elektronischen Bauelementen fast beliebig modifiziert werden können. In den letzten Jahren konnte gezeigt werden, dass die Verwendung dipolarer funktioneller Gruppen in SAMs die Austrittsarbeit von Metallen stark beeinflussen kann. Es konnte auch nachgewiesen werden, dass der Einbau dipolarer Gruppen in Monolagen zur Ausbildung einer Dipolschicht führt. Durch diese Dipolschicht werden die Energien der Orbitale ober- und unterhalb von ihr relativ zueinander verschoben.

In dieser Arbeit wurden auf Grundlage der Dichtefunktionaltheorie Bandstrukturrechnungen verschiedener SAMs durchgeführt. Für diese Bandstrukturrechnungen wurde der VASP code verwendet. Entlang der Moleküle, die diese SAMs bilden, wurden dipolare Gruppen eingebaut. Verschiedene Einflüsse auf die Lokalisierung der Orbitale, z.B. strukturelle, kollektive und Grenzflächeneffekte, wurden untersucht. Auf Basis der gewonnenen Erkenntnisse konnte ein Weg zur Entwicklung von Quanten-Well Strukturen gezeigt werden.

Um den Einfluss der chemischen Umgebung auf die Lokalisierung der Orbitale zu bestimmen, wurden verschieden Molekülstrukturen untersucht. Zudem wurde der Einfluss verschiedener dipolarer Gruppen auf die elektronische Struktur von SAMs analysiert.

Die Möglichkeit den Einfluss des Metalls auf den organischen Teil der Monolage mittels einer nicht konjugierten Gruppe zu reduzieren wurde untersucht. Außerdem wurde deren Potenzial bei Einbau in die Moleküle zur Verbesserung der Lokalisierung der Orbitale ermittelt.

Zum Abschluss wurden die elektronischen Eigenschaften dotierter SAMs untersucht.

Contents

Chapter 1

Introduction

1.1 Motivation

The functionality and efficiency of a molecular electronics device is defined mainly by the underlying electronic structure of the used molecule.[1, 2, 3] Some of the device properties, such as electronic transport, strongly depend on the localization of the molecular orbitals.[4, 5, 6] While the flow of electric current is significantly enhanced by using fully conjugated molecules with strongly delocalized orbitals, for other devices, e.g. quantum-wells, the orbitals need to be localized in a specific way.[7, 4] Thus being able to manipulate the electronic structure at will is very important for the design of new devices and device concepts as well as for the improvement of existing devices. Therefore, the aim of this work is to develop a molecular toolbox for the engineering of electronic wave-functions and consequently for the design of the orbital structure of molecules and self-assembled monolayers (SAMs). Parts of this toolbox are eventually used to build organic molecular quantum-well structures.

1.1.1 General Overview of Molecular Electronics

The field of molecular electronics was "started" by Aviram and Ratner in the year 1974 when they published their paper about molecular rectifiers.[8] In this work they proposed that a donor-acceptor system incorporated between metal electrons could be used as a rectifier.[8] Newer concepts for molecular rectifiers rely on asymmetric and dipolar molecules.[9, 10] Besides rectifiers, over time a great variety of different devices and device concepts were developed. In 1998, Tour et al proposed a new concept for molecular electronics devices. They demonstrated that a small change in the charge density of a molecule, induced due to an external electric field applied on one end of the molecule, could be detected at the other and of the molecule.[11] Thus, they showed that an information transfer through a molecule can be realized without the need of charge transfer.[11] Based on this concept different devices, like switches and logic gates, were build and characterized experimentally as well as theoretically.[11] Joachim et al suggested that the integration of elementary functions and interconnections required for computing into single molecules could simplify the fabrication of molecular electronics devices.[1] The molecules they introduced in their work act as molecular wires, switches, rectifiers or

storage devices.[1]

1.1.2 Organic Quantum-well Structures

The history of organic quantum-well structures dates back at least to the year 1993, when Burrows and Forrest published their observations of organic crystalline quantum-well structures.[12] They showed, that the process of organic molecular beam deposition could be used for the engineering of van-der-Waals bonded thin film materials.[12] In more recent work, the possibility of using organic quantum-well structures to build light emitting devices was demonstrated.[13, 6] These quantum-wells consist of organic hetero-structures and show a remarkable performance as white light emitting diodes.[14, 15] Organic molecular quantum-wells also have potential applications in fundamental research, as Bittner and Silva demonstrated by estimating the conditions necessary for the condensation of polaritons.[16] According to their calculations, it should be possible to observe this condensation in an anthracene-based thin film system.[16]

1.2 Localization

A localization of the electron wave-functions can be achieved through a variety of different methods. Which of these methods is best suited always depends on the material in use,certain approaches work only for certain materials.

The classical approach, which can be used in inorganic as well as organic materials, is to build so-called hetero-structures. This means, that neighboring parts of the structure have different frontier energy levels. In 1980, a design for a laser, based on inorganic quantum-well hetero-structures, was presented.[4] It was proven that a step-like density of states (DOS), as it can be established in a quantum-well hetero-structure, improves the operation of a semiconductor laser and leads to a threshold current density with a lower temperature sensitivity.[4] For organic hetero-structures often co-polymers are used the alternation of different organic building blocks provides the necessary differences in the energy levels.[17, 18, 19] A strong modification of excitonic properties, like the transition energy between the ground state and the lowest singlet excited state, and an improvement of the efficiency of charge- and energy-transfer processes for certain co-polymers was reported.[19] It has been demonstrated that the efficiency of organic solar cells can be improved by tuning the band gap in organic hetero-structures.[18] Lately, a modern version of organic hetero-structures was synthesized in the form of so-called covalent organic frameworks (COFs).[20] Theoretical investigations suggest that in some of these COFs a good localization and an excellent spatial separation of the highest occupied molecular orbital (HOMO) and the lowest unoccupied molecular orbital (LUMO) can be obtained.[21]

Another way to localize orbitals relies on morphological and geometrical effects. In Si-nanowires a shift between conduction- and valence-band edges in different parts of the structures occurs when the diameter of the nanowire differs along the long axis of the wire.[22] Varying the diameter of a nanowire along the long axis is called tapering and it leads to a localization of the HOMO at the end with the smaller diameter while th

LUMO us localized at the side with the larger diameter.[22] By using nanowires with a smaller diameter in the middle than at the outer sides, it is possible to build quantum-well structures using tapered nanowires.[22] The application of small amounts of strain or stress, both of which cause a slight distortion of the crystal structure, also leads to a separation of HOMO and LUMO in Si-nanowires.[23] It is believed that with this method morphology controlled solar cells can be manufactured.[23] A theoretical investigation shows that the termination of nanowires with different functional groups can also lead to a confinement of HOMO and LUMO in different parts of a nanowire.[24] Likewise, different functional end-groups used to terminate nanoflakes of graphene, a material at the borderline between organic and inorganic 'world', can be used for the confinement of HOMO and LUMO states.[25] This confinement is caused by a net dipole moment induced by the terminal group.[25]

A quite promising method to confine orbitals is to utilize collective electrostatic effects. A strong influence of collective electrostatic effects resulting from the electrostatic fields of intrinsic molecular dipoles on the electronic structure of oligopyrimidine SAMs has been demonstrated theoretically.[26, 27] It has been shown that such oligopyrimidine SAMs could be used to localize frontier orbitals on different ends of the monolayer.[27]

Amongst these localization, methods not all are very well suited for the design of organic molecular quantum-well structures. The most promising approach is the utilization of collective electrostatic effects. By embedding small dipolar units, such as pyrimidine, into the backbone of a monolayer it should be possible to localize frontier orbitals in an arbitrary way.

1.3 Collective Effects

As mentioned above, collective electrostatic effects exert influence on the orbital localization in SAMs.[26, 27] Besides these effects, a variety of collective effects are known to strongly influence the electronic structure of monolayers. As the name indicates, these effects are not occuring in a single molecule, but prevail only in a molecular assembly. They get stronger as the coverage is increased until a perfect, densly-packed, monolayer is reached.

The dependence of intra-molecular dipole coupling and depolarization on collective electrostatic effects can differ significantly for different molecules.[28] It has been reported that the electrostatic properties of monolayers composed of alkanethiol only weakly depend on collective electrostatic effects.[28] In contrast, the depolarization in monolayers which are assembled from molecules with dipolar head- and tail-groups show a strong dependence on intra-molecular dipole coupling.[28] Embedding dipolar building blocks in a monolayer can lead to the formation of a dipole layer. Such dipole layers display a very different behavior compared to single dipolar molecules.[27] For example, the global gap of a dipolar monolayer decreases linearly with the length of the monolayer, while in the isolated molecule the gap decreases with 1/length.[27] For the formation of a dipole layer a parallel alignment of the dipolar molecules is necessary. This can be accomplished by using a thiol docking group for the bonding of the molecules to the substrate.[29] It has also been demonstrated experimentally that such a dipole layer, formed by esther-groups

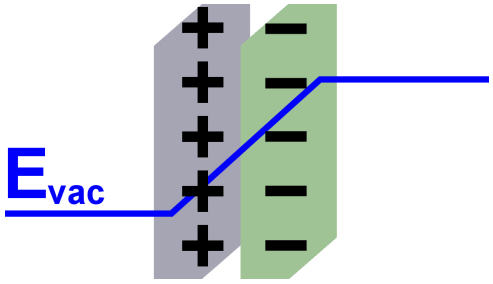

Figure 1.3.1: Illustration of a 2D dipole layer dividing vacuum into regions of different energies

embedded into alkanethiol SAMs, can energetically shift the states below and above the dipole layer.[29] In addition, two dimensional dipole layers are able to modify the shape of the electrostatic potential within the monolayer and divide the vacuum into regions of different energies (as illustrated in Figure 1.3.1).Therefore, they are well suited to modify the electronic structure of molecules at will.[30]

In molecular assemblies the ionization energy can get dependent on the orientation of the molecules, i.e. a different energy is needed to remove an electron from the organic molecule depending on whether the molecules lie on the substrate or form a SAM of upright standing molecules.[31, 32, 33] This can only be due to a collective effect, since for a molecule in gas phase the ionization potential is independent of the direction in which it is measured.

Collective effects should also be taken into account when it comes to electron transport in organic molecules.[34, 35, 36, 37, 38, 39, 40] While the conductance per molecule is lower in monolayers than in isolated molecules, the total current through the junction is higher in the case of the monolayer than in the case of the isolated molecule.[34] A part of the explanation is that thermal and electrostatic effects depend on the molecular environment and that these two effects have a big influence on the electronic transport.[34] Transport calculations and measurements of molecules with either one backbone or two parallel backbones show that the conductance for the "two-backbone" molecule can be more than twice that of the "one-backbone molecule". This indicates the occurrence of constructive interference.[39] The influence of cooperative effects on inelastic tunneling processes has been studied and the results suggest that cooperative effects can affect these processes even when intermolecular interactions do not need to be considered.[38] It has been shown that collective electrostatic effects can have an change the polarity of charge transport from electron to hole transport and vice versa.[40] The results of theoretical investigations of the influence of collective effects on the conductance suggest that several effects influence the conductance of molecular wires.[35, 37] Amongst others, these are energetic splitting, phase interference, substrate-mediated coupling and inter-wire coupling.[35, 37]

Collective effects in a monolayer can have a significant influence on the properties of a substrate material. For example, the so-called cooperative molecular field effect (COMFE) can be utilized for sensing applications.[41] Due to the COMFE, the accumulation of debris, in form of atoms or molecules, on a monolayer can induce substantial changes in the conductivity of a substrate material.[41]

Egbert Zojer and David Egger formulated the idea of utilizing collective electrostatic

effects and orbital localization methods for the development of a molecular toolbox for the engineering of electronic wave-functions. The building blocks of this toolbox will be introduced in the following section.

1.4 The Molecular Toolbox for Wave-function Engineering

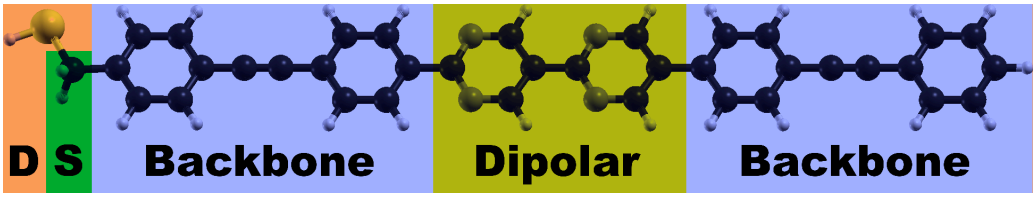

Figure 1.4.1: Example of an arrangement of different building blocks to a simple molecule. D: docking group, S: spacer unit.

In this section, the molecular building blocks that were used in this work will be introduced. They are divided into different groups depending on their intended functionality. The most simple molecules characterized in this work have the following base composition: *'D-Backbone-Dipolar-Backbone'*. Here 'D' denotes the thiol docking group, 'Backbone' refers to the backbone units used and 'Dipolar' stands for the shifting unit introducing the dipole moment into the monolayer. The introduction of a spacer unit ('S') between the docking group 'D' and a backbone unit leads to a *'D-S-Backbone-Dipolar-Backbone'* arrangement. An example for this kind of setup is shown in Figure 1.4.1. Putting spacer units between the backbone and dipolar units results in the following setup: *'D-Backbone-S-Dipolar-S-Backbone'*. Quantum-well and cascade-like structures are build using a *'D-S-Backbone-Dipolar-Backbone-Dipolar-Backbone'* setup. The backbone units are just organic semiconductors while the dipolar units are functional elements. These functional elements have the purpose of shifting the energy-levels within the backbone units relative to each other and to localize the frontier orbitals.

Dipolar units: The dipolar units used in this work are based on carbon rings, either conjugated or non-conjugated, in which C-H groups were asymmetrically substituted with elements possessing a higher electronegativity than carbon. This asymmetric substitution with elements of higher electronegativity is partially responsible for the occurrence of a dipole moments in these units. Besides this effect and amongst others, also lone-pairs of electrons in the elements replacing the C-H groups play an important role in the generation of dipole moments.

Bipyrimidine: Figure 1.4.2a shows the chemical structure of bi-pyrimidine. Bi-pyrimidine is a molecule based on bi-phenyl with two C-H groups of each phenyl-ring substituted by nitrogen. Without additional methyl-subtituents, bi-pyrimidine is fully conjugated and planar (see Figure 1.4.2c). It possesses close-lying σ- and π-states with

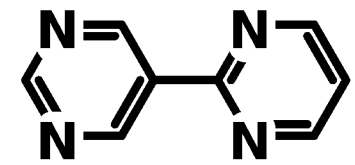

(a) Bipyrimidine

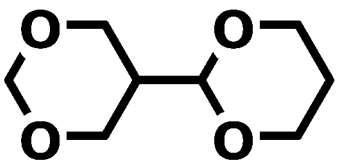

(b) Bidioxane

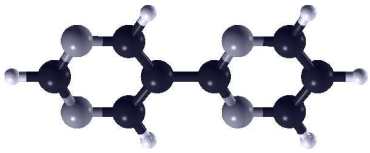

(c) Bipyrimidine

(d) Bidioxane

Figure 1.4.2: Chemical structures (a,b) and geometries (c,d) of the dipolar units.

their relative order being difficult to reproduce by common computational approaches.[26] The dipole moment of bi-pyrimidine in gas phase is circa 4.41 Debye according to a Gaussian03[42] calculation using the PBE[43] functional for exchange and correlation and the 6-31G* basis set.

Bidioxane: The chemical structure of bi-dioxane is shown in Figure 1.4.2b. It is based on a molecule consisting of two cyclohexane rings. Quite contrary to phenyl, cyclohexane is a saturated, non-conjugated carbon ring. Since cyclohexane is not conjugated and, therefore, not planar, the same is true for the dioxane. Thus, it provides some geometrical challenges for the simulation, e.g. a zig-zag like conformation, resulting in the necessity for a larger unit cell compared to planar systems. Here the element with the electronegativity higher than carbon introduced to produce a dipole moment is oxygen. The dipole moment along the long molecular axis is about 3.02 Debye, determined by a Gaussian03[42] calculation with the PBE[43] functional and the basis set 6-31G*.

Backbones: Different backbones were used, all of which were well conjugated but posses different electronic properties, including different gaps. The motivation for trying different backbones was to find out in which of them the localization is best and, therefore, which one is the most suited for the engineering of quantum-wells. Figure 1.4.3 depicts the chemical structures of the different molecular backbones studied here. In Figure 1.4.3a the Tour-wire based backbone is displayed. This was chosen because of the popularity that Tour-wires enjoy in the field of molecular electronics. Such backbones are also included in different structures.[11] Another advantage of the Tour-wire based backbone is that it has no sterical hindrance. It consists of two carbon rings separated by ethynylene. The next two backbones, biphenyl(b) and bithiophene (c), were selected since they are also used for different purposes in molecular electronics. Additionally bithiophene has a smaller gap, consequently a better localization was expected for this backbone. Biphenyl is composed of two phenyl rings. Bithiophene is build up from two carbon five-ring structures where

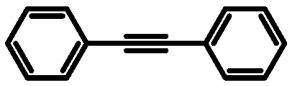

(a) Tour-wire based backbone molecule

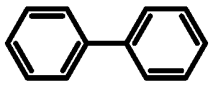

(b) Bi-phenyl

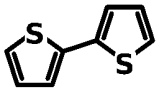

(c) Bithiophen

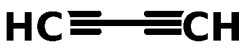

(d) Butadiyne

Figure 1.4.3: Chemical structures of backbone units

in every ring one carbon is substituted by a sulfur atom. The motivation to try butadiyne as backbone was its size, since it could allow higher packing densities and, therefore, potentially an improvement of the localization and an increase in orbital shifts.Spacer units:

A spacer unit has the task to prevent influences from the substrate on the organic parts or to decouple different units of the organic part of the monolayer. For the first task a methyl spacer has been used.[7] The second task is more complex, since a decoupling of conjugated units requires a spacer that is able to break the conjugation. Therefore, non-conjugated units have to be put between the conjugated backbone units. One might think about using a methyl spacer for this task too. But a simple geometry optimization of a system with methyl spacers between phenyl-backbone and bi-pyrimidine shifting units has ruled out the mentioned methyl as its bonding angles in this setup are between 111 and 114 degrees. On the other hand, methyl could be used for side-chains that should lead to a twist in between the units it is attached to and therefore reduce the conjugation. For other non-conjugated spacers the challenge is to overcome the geometric issues, e.g. different conformations in the case of cyclohexane. Two more exotic spacer units that where tested are cyclohexane and magnesium. The usage of the first one was suggested by Elisabeth Verwüster because it is a non-conjugated carbon ring and still allows almost planar structures. The idea to test magnesium as spacer was motivated by the fact that magnesium can make exactly two bonds. Therefore, by bonding it to two different units it brakes the conjugation.

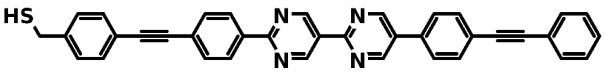

(a) Molecule with Tour-wire based backbone, bipyrimidine shifting unit and methyl spacer.

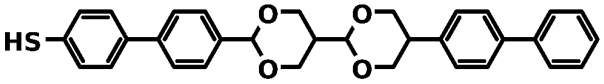

(b) Molecule with biphenyl backbone, bi-dioxane shifting unit.

Figure 1.4.4: Examples of molecules assembled from the different building blocks.

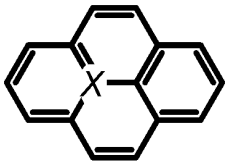

Figure 1.4.5: Chemical structure of pyrene. The X denotes the substituted atom.

Figure 1.4.4 shows two examples of molecules that were assembled from components described in this section.

Pyrene: Figure 1.4.5 displays the chemical structure of pyrene with the X denoting the atom that was substituted by boron and nitrogen. This doping of a conjugated structure like pyrene leads to a monolayer exhibiting radical behavior.[44, 45] In such doped structures a singly occupied molecular orbital at the Fermi-energy occurs, enabling zero-bias conduction.[44]

1.5 Theoretical Background: Density Functional Theory and the Slab Approach

Density functional theory: This part follows the Chapters 3, 6, 7 and 8 of reference [46].

The Hamilton operator for any system of interacting electrons and nuclei in the Born-Oppenheimer approximation can be written as the sum of four terms [46, page 53]:

$$\hat{H} = \hat{T} + \hat{V}_{ext} + \hat{V}_{int} + E_{II} \tag{1.5.1}$$

Here $\hat{T}$ is the kinetic energy of the electrons, $\hat{V}_{ext}$ is interaction between nuclei and

electrons, $\hat{V}_{int}$ is the electron-electron interaction and E_{II} denotes the nuclei-nuclei interactions.

In 1964, Hohenberg and Kohn formulated a new theory for interacting many-body systems called density functional theory (DFT). They based their new theory on two theorems, nowadays entitled as Hohenberg-Kohn-theorems. The first of these theorems states that the ground state density $n_0(\mathbf{r})$ uniquely determines the external potential $\hat{V}_{ext}$, except for a constant, for any interacting particle system in this external potential.[47] From this theorem it follows that for a given ground state density $n_0(\mathbf{r})$ all properties of the system are completely determined.[46, page 122] The second theorem states the possibility of a definition of a universal functional for the energy $E[n]$, which is valid for every external potential[47]. It also states that the global minimum value of this functional corresponds to the ground state energy and that the density belonging to this energy is the ground state density $n_0(\mathbf{r})$.[47] Therefore, the determination of the ground state requires only this universal functional $E[n]$. With these two theorems and their implications it is now possible to rewrite the Hamiltonian from above as a total energy functional:[46, page 124]

$$E_{HK}[n] = T[n] + E_{int}[n] + \int d^3r\, V_{ext}(\mathbf{r})n(\mathbf{r}) + E_{II} \tag{1.5.2}$$

The disadvantage of this Hohenberg-Kohn density functional theory is that results derived using it are difficult to interpret since it only delivers the ground state density. In principle, the ground state density is sufficient for the understanding of the properties of a material.[46, page 131] Nevertheless, the relation between the density and the properties are very subtle and so far no way of extracting a general set of properties from the density alone has been found.[46, page 131] This problem was solved through the introduction of the Kohn-Sham auxiliary system in the year 1965.[48] The main idea behind this auxiliary system was to replace the interacting many-body problem by a system of non-interacting particles. In this Kohn-Sham theory, all of the interactions are put into an effective potential which is a functional of the density while the kinetic energy of the electrons is treated by an independent particle approach.[48] Kohn and Sham constructed the auxiliary system under the assumption that the ground state density of a non-interacting system can reproduce the exact ground state density.[46, page 136] So far no rigorous proof of this assumption has been provided for real systems of interest.[46, page 136] The Hamiltonian for the auxiliary system can the be written as:[46, pages 135-137]

$$\hat{H}^{\sigma}_{aux} = -\frac{1}{2}\nabla^2 + V^{\sigma}(\mathbf{r}) \tag{1.5.3}$$

In Kohn-Sham theory, the charge density is constructed by a summation over all single particle wave-functions:[46, page 137]

$$n(\mathbf{r}) = \sum_{\sigma}\sum_{i=1}^{N^{\sigma}} |\psi_i^{\sigma}(\mathbf{r})|^2 \tag{1.5.4}$$

As a next step, on basis of the equations 1.5.3 and 1.5.4 Kohn and Sham rewrote the total energy functional from Hohenberg-Kohn theory (equation 1.5.2):[46, page 137]

$$E_{KS} = T_s[n] + \int d^3r\, V_{ext}(\mathbf{r})n(\mathbf{r}) + E_{Hartree}[n] + E_{II} + E_{xc}[n] \tag{1.5.5}$$

In this equation, $E_{Hartree}[n]$ is the so-called Hartree energy.It describes the Coulomb interactions of the charge density with itself[46, page 137], also termed self-interaction energy.[46, page 56] In this formulation, all exchange and correlation effects of the many-body problem are grouped in the exchange-correlation energy $E_{xc}[n]$. An expression for the exchange-correlation energy can be derived by a comparison of the Hohenberg-Kohn and Kohn-Sham expressions for the total energies. The derived expression for the exchange-correlation energy reveals that it is the difference of the kinetic energies and internal interaction energies of the exact interacting many-body system and the auxiliary system. The exchange-correlation energy is given by the following expression:[46, page 138]

$$E_{xc}[n] = \left\langle \hat{T} \right\rangle - T_s[n] + \left\langle \hat{V}_{ext} \right\rangle - E_{Hartree}[n] \tag{1.5.6}$$

So far both approaches, Hohenberg-Kohn and Kohn-Sham, lead to the exact ground state density. Therefore, the solution for the interacting many-body problem could be obtained by solving the independent particle equations, at least if the exact functional for the exchange-correlation energy were known. Since this is not the case one has to use approximations for $E_{xc}[n]$. Several different approximations were proposed leading to a big variety of exchange-correlation functionals. The simplest approximation is the so-called *local density approximation (LDA)*. In this approximation the exchange-correlation energy only depends on the local charge density $n(\mathbf{r})$. As long as the charge density of the investigated system does not vary too much, i.e. for charge densities similar to a homogeneous electron gas, LDA works quite well.[46, pages 152-154] For many interesting systems, the charge density fluctuates too much to approximate them by a homogeneous electron gas. For this reason, functionals that take the gradient of the charge density into account have been proposed. They are grouped under the term *generalized gradient approximation (GGA)*.[46, pages 154-156] A GGA functional, which is currently very popular, and was used in this work, was proposed by Perdew, Burke and Enzerhof.[43] They derived the so-called PBE[43] functional using only fundamental constants as parameters. It delivers an accurate description of the linear response of the homogeneous electron gas, as well as a correct behavior under uniform scaling.[43] *Hybrid functionals* combine the exact exchange energy calculated with Hartree-Fock theory with the exchange and correlation energies of LDA or GGA.[46, page 165] This type of functionals cause a high computational cost when combined with periodic boundary conditions, as it requires the calculation of the Hartree-Fock exact exchange energy. All in all, for solids GGA functionals like PBE[43] provide a good compromise between computational cost and accuracy of the results. It enables the investigation of larger systems consisting of a few hundred atoms.

A major drawback of Kohn-Sham theory is that the auxiliary system of non-interacting electrons has no rigorous physical meaning.[46, pages 135-137]

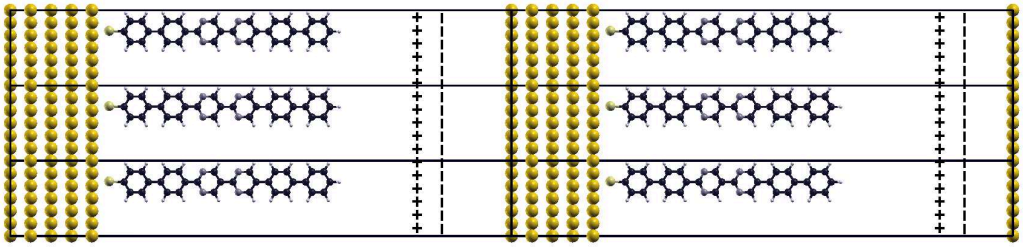

Figure 1.5.1: Repeated slab approach with artificial dipole layer

Repeated slab approach:[49] The computational treatment of molecules on surfaces is not straightforward when using codes or methods that make use of periodic boundary conditions in all three spatial directions. The fact that surfaces are periodic only in two spatial dimensions presents a problem for codes using 3D periodic boundary conditions. In the direction perpendicular to the surface the periodicity is lost in the actual system. An often used solution to regain periodicity in the third direction is the so-called *repeated slab approach*. In this approach, the unit cell is repeated in all spatial directions including the non-periodic one (see Figure 1.5.1). Several layers of the substrate material, e.g. gold, are used to act as slab on which the molecules are adsorbed. To prevent electronic interactions between two consecutive images of the slab, a vacuum gap has to be introduced. This gap needs to be large enough to ensure that the electrostatic potential of the slab and the adsorbed molecules reaches the vacuum level within the unit cell. The introduction of dipolar molecules in the backbone of a SAM leads to the formation of a 2D dipole layer which introduces a step in the electrostatic potential (as described in section 1.3). Since in this case the vacuum energies on the left and right sides of the dipole layer are different and never going to adopt the same value, no matter how large the vacuum gap is, it is necessary to introduce an artificial dipole jump within the vacuum region when simulating such systems. This artificial dipole layer is depicted in Figure 1.5.1, indicated by the plus and minus signs. The magnitude of the dipole moment of this artificial layer is determined self-consistently. The artificial dipole layer suppresses spurious electrostatic interactions between consecutive slab images along the non-periodic direction. A favorable side effect of this approach with an artificial dipole layer is that it allows the simulation of the properties of free-standing monolayers. Such 2D molecular crystals cannot be manufactured and analyzed experimentally. The repeated slab approach provides a handle to study properties of such systems theoretically. Additionally, the slab approach enables the investigation of interface effects.These can be identified by a comparison of the properties of the free-standing monolayer with the SAM.

Modern DFT codes are able to determine the position and dipole moment of this artificial dipole layer automatically. In addition, they often provide a variety of settings for the manual positioning the artificial dipole layer. No matter whether the positioning is done manually or automatically, the size of the vacuum gap needs to be large enough and the dipole layer far enough away from the molecules to assure that this artificial dipole moment does not have any undesired influence on the electronic properties of the system. During this work tit was found that when using VASP[50] the vacuum gap needs to be at least 20 Å (for some systems even significantly larger). .

1.6 Methodology

1.6.1 DFT-codes (Gaussian03[42], VASP[50])

The first step for studying each of the used molecules was to perform a geometry optimization in gas phase. This optimization step was done with the Gaussian03[42] code and the PBE[43] functional. As Gaussian03 is a so-called LCAO (linear combination of atomic orbitals) code, one has to specify a basis set to carry out DFT calculations.[51] For this work, the basis set 6-31G* was chosen. The basis set 6-31G* uses a single basis function per atomic orbital for the inner shells of the molecules.[51] For the valence orbitals, two basis functions per atomic orbitalare used.[51] Therefore this basis set is classified as a split-valence basis set.[51] Linear combinations of primitive Gaussian-functions are used to build up the basis functions. The basis set 6-31G* uses a linear combination of 6 Gaussian-functions for the inner shell orbitals and 3 respectively 1 Gaussian-functions for the valence orbitals.[51] 6 primitive Gaussian-orbitals of d-symmetry are used in this basis set to model polarization-functions (displayed by the * in the name).[51]

For the calculations with periodic boundary conditions and single point calculations of isolated molecules, the Vienna ab-inito simulation package (VASP)[50] was used. VASP[50] is a plane wave code designed for simulations with periodic boundary conditions in all three dimensions. Interfaces, like SAMs, are only periodic in two dimensions (x- and y-dimension). Therefore, it is necessary to use the repeated slab approach, as described in section 1.5. For this purpose VASP[50] provides two tags, the `IDIPOL`-tag specifies the spatial direction orthogonal to the dipole layer and the `LDIPOL`-tag is used to turn the dipole-correction on or off.[52] The standard procedure for performing calculations for this work was to first perform a calculation without dipole correction and then use the converged `CHGCAR` and `WAVECAR` files as starting point for a calculation with the dipole correction activated in the z-direction (`IDIPOL=3`, `LDIPOL=.TRUE.`). The unit cell used for most of the calculations was a rectangular $2\sqrt{3} \times 3$ unit cell. In this unit cell, the monolayers were arranged in upright standing position. The top and the side view of the unit cell for a Tour-wire based SAM are shown in Figure 1.6.1. One can see that the unit cell contains only one molecule, consequently resulting in a low packing density.

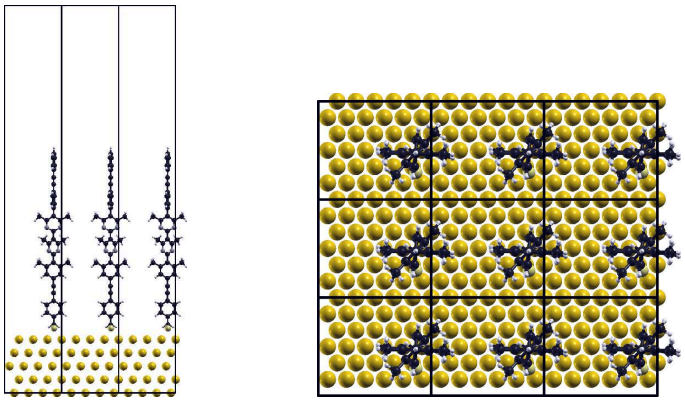

(a) side view *(b) top view*

Figure 1.6.1: Illustration of a rectangular $2\sqrt{3} \times 3$ unit cell for a Tour-wire based SAM.

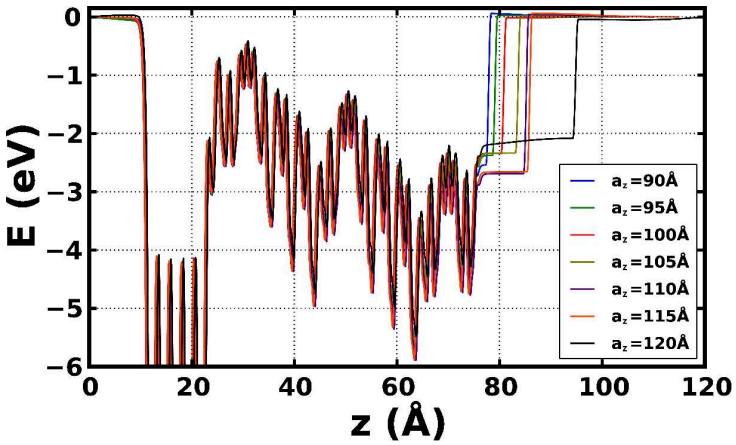

Figure 1.6.2: Plane averaged electron potential energy for the cascade system for different sizes of the unit cell in z-direction.

Due to the periodic boundary conditions in all three directions, performing single point calculations of isolated molecules requires a large unit cell in x- and y-direction, while for the z-direction the dipole correction is enabled. The size of the unit cell in x- and y-direction were set to 40 Å to simulate molecules in gas phase in VASP[50]. To ensure that the distance between the dipole jump and the molecule is large enough, the size of the unit cell in z-direction has to be increased as well. Figure 1.6.2 shows the electron potential energies of one system for different sizes of the unit cell in z-direction. One can see, that the size of the unit cell in z-direction has a huge influence on the work function modification. In addition, artifacts occur in the vacuum region. For the unit cell size of 120 Å in z-direction, before and after the dipole jump the potential exhibits a slight curvature. For the other unit cell sizes, a slight curvature occurs after the dipole jump only. This plot also shows, that for the unit cells with sizes less than 100 Å the dipole jump is very close to the molecule. The values for the work-function modifications and additional information about the test with different unit cell sizes can be found in Appendix A. The plane wave cutoff energy was set to 273.894 eV to be consistent with earlier work of the group. The functional that was used in this work was the PBE-functional.[43]

Even though VASP[50] provides routines to perform geometry optimizations of periodic systems itself, the VASP-based optimizer GADGET[53] was used in this work to conduct full geometry optimizations of SAMs. One of the reasons for this choice of the optimizer was that VASP[50] uses Cartesian coordinates for the optimization while GADGET performs the optimization in internal coordinates.[53] Performing the optimization using internal coordinates is more efficient and leads to more realistic results compared to an optimization in Cartesian coordinates. Additionally, GADGET[53] offers different optimization algorithms, namely *Direct Inversion in Iterative Subspace (DIIS)[54, 55]* and *Rational Function Optimization (RFO)[56, 57].* According to Tomáš Bučko the *RFO* algorithm works better for the investigated systems than *DIIS*. The fact that all of the geometry optimizations performed with the *DIIS* diverged confirms his statement. Therefore, the *RFO* algorithm was used.

1.6.1.1 Construction of the unit cell

The Gaussian03[42] optimized geometries of the molecules had to be converted to VASP[50] input geometries. For this purpose, first, the coordinates and atomic numbers of the optimized geometries of the molecules were copied from the Gaussian03[42] log-file to a spreadsheet. In this spreadsheet, the data were sorted by the atomic number. Then, the coordinates were copied to a VASP[50] geometry file containing the gold-slab and a sulfur atom to indicate the position of the docking group. As a next step, p4VASP[58] was used to move the molecules to their positions in the unit cell. The binding position of the sulfur atom was the *fcc hollow site* of the gold-slab. The molecules were rotated to be upright standing with respect to the surface. Finally, the size of the unit cell in z-direction was adjusted to provide a vacuum gap of not less than 20 Å.

1.6.2 Iso-density plots

Iso-density plots are a convenient way to display the shape of molecular orbitals or charge densities (or the local density of states(LDOS) when unoccupied states are involved). The term *LDOS* denotes the density of states in as a function of the spatial coordinates for a certain energy interval or band. An iso-density plot shows the contour of the LDOS for a certain value, the so-called iso-value. In this work, iso-density plots were used for visualizing the local density of states (LDOS) of a certain energy interval or a particular band. An example for an iso-density plot is shown in Figure 1.6.3. It displays the LDOS of the highest occupied band of a free-standing monolayer with Tour-wire backbone and bi-pyrimidine shifting unit. For the calculation of the LDOS, VASP[50] needs a converged `WAVECAR`-file of the particular system.[52] Therefore, the LDOS generation can only be done as a post-processing step after the performance of a single point calculation. VASP[50] provides several tags for the purpose of calculating the LDOS. The tags used in this work are listed in Table 1.1, further information and more tags can be found in the *VASP User guide*.[52]

The iso-density plots in this work were generated with *XCrysDen*.[59] To use the VASP[50] output files with *XCrysDen,* one has to convert them first with a script called *v2xsf*.

A big disadvantage of iso-density plots is that the iso-value has to be chosen carefully. With a particular choice for the iso-value, one can generate quite misleading impressions with an iso-density plot. Therefore, this kind of plots is not suited for quantitative statements but only to show the shape of the examined LDOS.

Figure 1.6.3: Iso-density plot of the LDOS of the highest occupied band of a free-standing monolayer with Tour-wire backbone and bi-pyrimidine shifting unit.

Table 1.1: VASP-tags for the calculation of the LDOS[52]

tag	used value	description
LPARD	.TRUE.	tells VASP[50] to calculate the LDOS
IBAND	# of one ore more bands (e.g. 80 81 82 ...)	define the bands (by their numbers) for which the LDOS should be calculated
EINT	energy interval in eV	defines the energy interval for which the LDOS should be calculated, only makes sense if IBAND is NOT defined
LSEPB	.TRUE.	if this tag is set to .TRUE., VASP[50] writes the LDOS for every band in a separate file, only useful if IBAND is used to specify the bands
LSEPK	.TRUE.	if this tag is set to .TRUE., VASP[50] writes the LDOS for every k-point in a separate file

1.6.3 Other plots

In this section, the generation of the DOS, electron potential energies, the Unit-DOS and the LDOS contour map plots will be explained. The generation of the latter two will be explained in more details as some non-trivial steps are required. The meaning of the term *Unit-DOS* will be explained in the corresponding subsection while the definition of the *LDOS* is given in the previous section.

With the exception of the iso-density plots, almost all plots for this work were made with the programming language *Python* and the Python-library *Matplotlib*[60]. This way the creation of similar plots for different systems is quite easy since only a few parameters, like the Fermi-energy, have to be adjusted in the *Python* scripts. For generating most plots, like the density of states (DOS) or potential energy plots, the procedure is quite straightforward. First the data is loaded into *Python* from the respective data files, then the data is aligned, e.g., to the Fermi-energy for the DOS plots, and in the last step it is plotted with the help of *Matplotlib*. The creation of the Unit-DOS plots and LDOS (local density of states) contour maps will be discussed in more detail in the next subsections. For these plots, the data is post-processed within the *Python*-scripts.

1.6.3.1 Unit-DOS plots: interpolation and integration

The molecules used in this work were divided into units of different functionalities indicated by different colors in the sketches of the chemical structures. As an example, Figure 1.6.4 shows the chemical structure of a molecule divided into different units. Here, the blue unit is the substrate-side backbone, the green one is the shifting unit and the red one is the vacuum-side backbone. For molecules with a different number of units, the color coding is different to the one shown here. The term *Unit-DOS* denotes the sum of the densities of states projected onto the atoms of a certain unit.

The Unit-DOS plots depict the Unit-DOS's for all the units in a waterfall plot following the color coding of the sketch of the chemical structure. Additionally, vertical lines indicate the energy intervals containing two electronic states, one spin up and one spin down state, of the net DOS of all three units. The reason for calculating these intervals was to determine which section of the DOS effectively corresponds to a single state (of course, not directly considering that states can overlap). Figure 1.6.5 shows the Unit-DOS plot for the molecule shown in Figure 1.6.4.

For the calculation of the energy intervals containing two states an interpolation and an integration step are necessary. These are explained in detail within the next two subsections. The plotting of the Unit-DOS itself is actually quite straightforward. A short remark: for the numerical integration it is necessary to avoid negative values of the DOS. Thus it is mandatory to use an appropriate smearing method, e.g. Gaussian

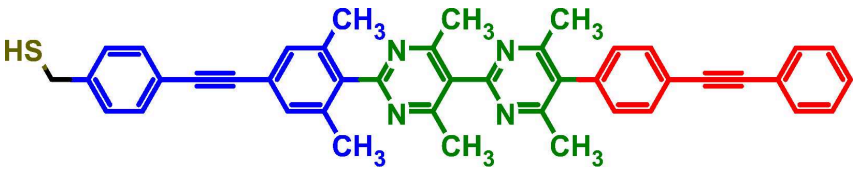

Figure 1.6.4: Example for the segmentation of a molecule into units indicated by the different colors.

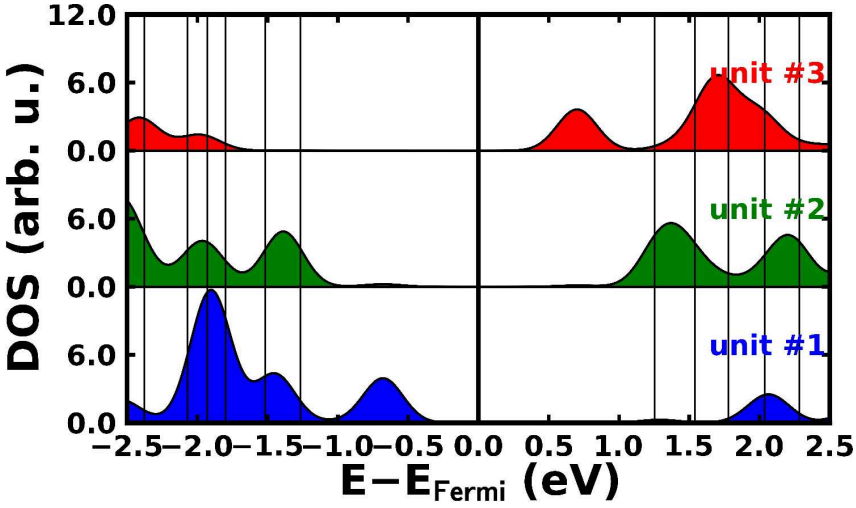

Figure 1.6.5: Unit-DOS plot for the molecule depicted in Figure 1.6.4. The black vertical lines indicate the energy intervals containing two states.

smearing (`ISMEAR=0`).

Interpolation: With the standard input parameters for the VASP[50] calculations that were used in this work, the output for the DOS contains about 5000 data points for energies ranging from $-40\,\text{eV}$ to $+20\,\text{eV}$. This amount of data points is enough for plotting the DOS but doing a numerical integration with that number of data points would lead to significant errors. Therefore, an interpolation step has to be made before the integration. For this purpose a function called `interpol` was defined and can be called by the following line:

```
E_int, U_int = interpol(E, U, E_fermi)
```

It possess the following input and output parameters:

Input parameters:

- `E`: a one dimensional array containing the *original* energy values
- `U`: a one dimensional array containing the *original* DOS values (naturally it has to have the same size as `E`)
- `E_fermi`: a scalar defining the Fermi-energy (or any arbitrary energy) to which the interpolated energy (`E_int`) values will be aligned

Output parameters:

- `E_int`: a one dimensional array containing the *interpolated* energy values
- `U_int`: a one dimensional array containing the *interpolated* DOS values

This function prepares the interpolated energy values and uses the `interp1d` function provided by scientific Python library *Scipy*[61, 62]. The complete source code of the `interpol` function is provided in the following listing:

Listing 1.1: Python source code of the `interpol` function

```
1  def interpol(E, U, E_fermi):
2      '''
3          inputs: E        ... list of energy-values
4                  U        ... list of quantity to
                       interpolate (e.g. DOS)
5                  E_fermi  ... Fermi energy
6          outputs:E_int    ... interpolated energy values
7                  U_int    ... interpolate quantity
8      '''
9
10     x = -39.0    #minimal energy
11     E_int = []   #list to save interpolated energy values
```

```
12      dx = 60.0 / 1600002.0   #energy interval for
           interpolation
13
14      #interpolate energy values from x to 19.0-dx
15      while x<=19.0-dx:
16          E_int.append(x-E_fermi)
17          x=x+dx
18
19      ip = interpolate.interp1d(E,U)  #generate
           interpolation function
20      U_int = ip(E_int)   #interpolate U
21
22      return E_int, U_int
```

Line 1 is the definition of the function and immediately thereafter are a few lines of comments explaining input and output parameters. In line 10 the minimal value for the energy interpolation `x` is defined. Since the method used to generate the interpolation function is not able to extrapolate one has to assure that the minimum and maximum values for the energy interpolation are higher respectively lower than minimal and maximal magnitudes of the original energy data. Line 11 shows the initialization of an empty list, later used to store the interpolated energy values. The energy interval for the interpolation is defined in line 12. Its value was arbitrarily chosen and represents a good compromise between computing effort and precision. The loop depicted in the lines 15 to 17 generates the interpolated energy values by subtracting the Fermi-energy from `x` and then incrementing `x` by `dx`. The generation of the *linear* interpolation function takes place in line 19 and uses the *Scipy* function `interp1d` with the original data as input. A linear interpolation function was chosen to reduce the computational costs. The interpolation of the DOS is done in line 20 by using the generated interpolation function with the interpolated energy values as input. In the last line (22) the interpolated data are returned to the program calling this function.

Integration: After the interpolation is completed, one can now integrate the DOS to determine the energy intervals containing two states. An integration function was defined and can be called by the following code line:

```
I = integrate(E, DOS)
```

The input and output parameters are as follows:

Input parameters:

- `E`: a one dimensional array containing the energy values
- `DOS`: a one dimensional array containing the DOS values (needs to have the same size as `E`)

Output parameter:

- `I`: a one dimensional array containing the energy values defining the intervals with 2 states in them (it DOES NOT contain the Fermi-energy which is assumed to be 0 eV due to alignment)

In principle, the input quantities do not have to be interpolated before the integration procedure but it is highly recommended. One also has to take into account that it is assumed that the input energies are aligned to the Fermi-energy and therefore the latter one is not included in the output. The source code of the integration method is shown in the following listing:

Listing 1.2: Python source code of integration function

```
1  def integrate(E, DOS):
2      '''
3          inputs: E   ... list of energies
4                  DOS ... list of DOS-values related to
                      energies in E
5          output: I   ... list of intervall containing 2
                  states
6      '''
7
8      I=[]     #list for intervalls containing 2 states
9
10     #find index of Fermi-energy
11     i=0
12     while True:
13         if E[i] > 0:
14             break
15         i+=1
16
17     #integrate below Fermi-energy
18     j=i-1
19     s=0          #sum of states in current interval
20     n_elec=0     #total number of occupied states
21     while j>0:
22         s = s + (E[j]-E[j+1])*(DOS[j]+DOS[j+1])/2 #
               integration
23
24         if fabs(s)>=2:  #if there are two states in the
               interval:
25             n_elec = n_elec + s #add s to number of
                   occupied states
26             I.append(E[j])  #append aktual energy to list
                   of intervals
27             s = 0   #set sum of states to zero
```

```
28          j = j -1
29
30      print fabs(n_elec) #print number of occupied states
           in closed intervals
31      print fabs(s)   #print number of occupied states in
           lowest (open) energy interval
32
33      #integrate above Fermi-energy, details see above ;)
34      k = i
35      s=0
36      while k<len(E)-1:
37          s = s + (E[k]-E[k+1])*(DOS[k]+DOS[k+1])/2
38
39          if fabs(s)>=2:
40              I.append(E[k])
41              s = 0
42          k = k + 1
43
44      I.sort() #sort energy intervals
45
46      return I
```

As for the interpolation function, line 1 is the definition of the function and immediately thereafter are a few lines of comments explaining input and output parameters. In line 8 a list variable `I` is defined, which in the end will contain the intervals. The task of determining the energy intervals containing two states was divided into three parts. First the index `i` of the Fermi-energy is identified (lines 10 to 15). The second step is to integrate below the Fermi-energy (lines 18 to 28). For this purpose a counting variable `j` is defined and initialized as `i-1` in line 18. In the lines 19 and 20, variables for the sum of states in the current interval `s` and for the total number of occupied states `n_elec` are defined and set to zero. Then a loop is executed with the exit condition `j>0` (line 21). In this loop the integration is carried out using the following equation to calculate the value of the integral *Int* in the energy interval $[E_j,E_{j+1}]$:

$$Int = \frac{(E_j - E_{j+1})}{2} * (DOS_j + DOS_{j+1}) \tag{1.6.1}$$

In the same step, where the value of the integral is calculated it is added to the sum of states `s in` the interval (line 22). In line 24 it is tested whether the number of states `s` is greater than or equal to two. If this is the case, the actual energy is added to the list of intervals `I` and `s` is reset to zero (lines 26 and 27). Additionally, `s` is added to the number of occupied states `n_elec` (line 27). The last step within the loop is to decrement the counting variable `j`. In lines 30 and 31 the number of occupied states and the number of occupied states in the lowest interval, which is downwards open, are printed on the screen. This is done to get an indication whether something went wrong. The sum of the two quantities should be close to the number of valence electrons in the corresponding VASP[50] calculation. The third step in the integration procedure is to integrate above

the Fermi-energy (lines 34 to 42). As this is very similar to step two, it will not be explained separately here. In the end, the list of intervals is sorted in ascending order (line 44) and returned (line 46).

1.6.3.2 LDOS contour map

The use of this kind of plots was inspired by a paper published by Segev et al.[63] The LDOS contour map depicts the local density of states as a function of the energy and the z-direction as a colored map. In these contour map plots, the LDOS is displayed in units of electrons per Å by colors ranging from blue for a value of 0.00 e/Å to red for values of 0.05 e/Å or higher. The LDOS plots are aligned to the chemical potential which is calculated from the HOMO and LUMO energies by the following equation:

$$\mu = \frac{E_{HOMO} + E_{LUMO}}{2} \tag{1.6.2}$$

Figure 1.6.6 shows the LDOS contour map for the free-standing monolayer composd of the molecule shown in Figure 1.6.4. In this plot, the electronic structure of the free-standing monolayer can be seen quite well. It gets clear that for this free-standing monolayer the highest occupied molecular orbital (HOMO) is localized on the left side (substrate-side) and the lowest unoccupied molecular orbital (LUMO) is localized on the right side (vacuum-side).

For the generation of such LDOS contour map plots, one has to calculate the LDOS for a large number of consecutive energy intervals and plane integrate it over the x-y-plane. Consequently, the plane integrated LDOS has an energy and a z dependence. The necessary input parameters are given in Table 1.1 of subsection 1.6.2. Since VASP[50] can calculate the LDOS only for a single energy interval at a time, a script was written to start the calculations for several intervals sequentially. The source code of this script is given

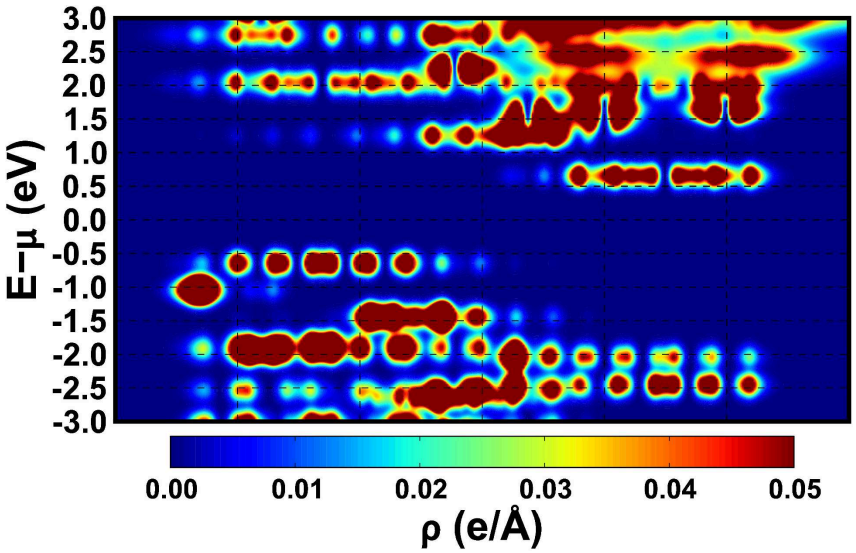

Figure 1.6.6: LDOS contour map of the free-standing monolayer for the molecule shown in Figure 1.6.4.

in Appendix C. The next step is to convolute the LDOS data with a Gaussian-function numerically. For this task a *Python* module was written in *Fortran* (see Appendix C) which uses the following equation for the convolution:

$$LDOS_{conv}[z,E] = \underbrace{\frac{\Delta E}{\sigma * \sqrt{2 * \pi}}}_{A} * \underbrace{\sum_{j=E_{min}}^{E_{max}} LDOS[z,j]}_{B} * \underbrace{\sum_{i=E_{min}}^{E_{max}} exp\left(\frac{-(E-i)^2}{2*\sigma^2}\right)}_{C} \tag{1.6.3}$$

In this equation $LDOS_{conv}$ denotes the convoluted LDOS, ΔE is the energy interval, σ is the standard deviation of the Gaussian-function and the value that defines the width of the smearing, $LDOS$ is the original LDOS. In equation 1.6.3, part A is the normalization factor of the Gaussian-function multiplied with the energy interval for the numerical convolution ΔE. Part B denotes the summation of the original LDOS over all energy values for a certain z-coordinate that is numerically convoluted with the Gaussian-function of part C. Last but not least, the convoluted LDOS can be plotted, e.g. using a *Python* script (for source code see Appendix C).

1.6.4 Definition of Energy Differences

The energetic shifts of orbitals were calculated by subtracting the energies of the peaks of the highest occupied state of the vacuum-side unit and the substrate-side unit. These energies were extracted from the densities of states projected on the two units. Figure 1.6.7 shows the selected peaks and their naming for the free-standing monolayer of the molecule shown above in Figure 1.6.4. Unit #1 is the substrate-side unit and unit #3 the vacuum-side unit.

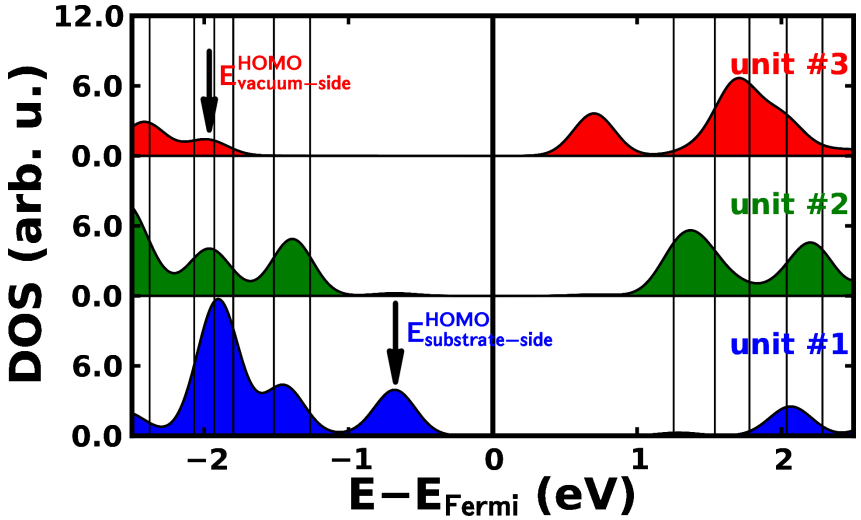

Figure 1.6.7: Unit-DOS plot for the free-standing monolayer of molecule depicted in Figure 1.6.4. The black vertical lines indicate the energy intervals containing two states. The arrows indicate the peaks for the calculatin of the orbital shift of the HOMO.

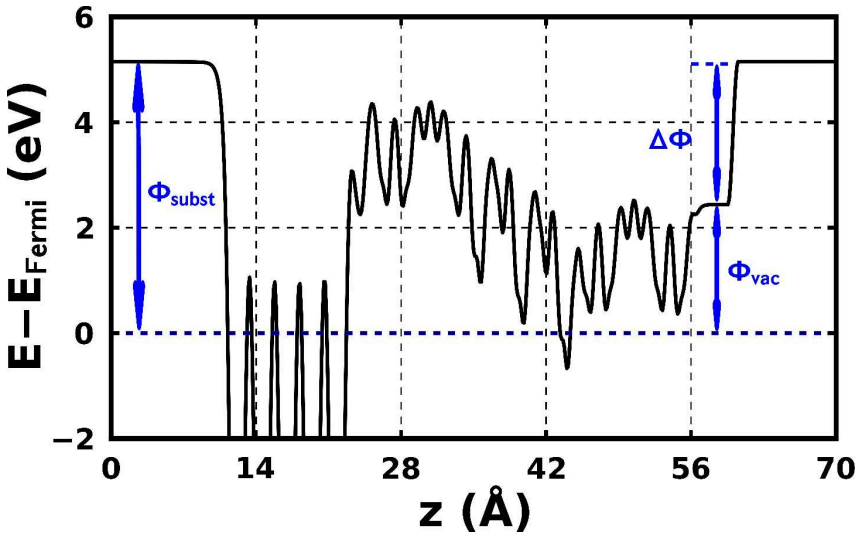

Figure 1.6.8: Definition of the work-function modification $\Delta\phi$

The orbital shifts were calculated for the HOMOs according to the following equation:

$$E_{shift} = E^{HOMO}_{vacuum-side} - E^{HOMO}_{substrate-side} \tag{1.6.4}$$

Here $E_{shift}$is the energy by which the orbital was shifted, $E^{HOMO}_{vacuum-side}$ is the energy of the peak of the highest occupied state on the vacuum-side unit and $E^{HOMO}_{substrate-side}$ is he energy of the peak of the highest occupied state on the substrate-side unit. The energy shift of the LUMO can be calculated in an analogous manner by selecting the peaks of the lowest unoccupied states of the respective units.

Figure 1.6.8 shows the definition of the work-function modification $\Delta\phi$ in a SAM as the difference between vacuum-side work-function ϕ_{vac} and the substrate-side work-function ϕ_{subst} graphically.

From the graphic definition of the work-function modification follows the following equation for its calculation:

$$\Delta\Phi = \Phi_{vac} - \Phi_{subst} \tag{1.6.5}$$

The calculation of the change in the vacuum-energy ΔE_{vac} for a free-standing monolayer is defined and calculated analogous to the work-function modification in a SAM. It is the difference between the vacuum-side vacuum-energy E^{vac}_{vac} and the substrate-side vacuum-energy E^{subst}_{vac}:

$$\Delta E_{vac} = E^{vac}_{vac} - E^{subst}_{vac} \tag{1.6.6}$$

1.6.5 Measurement of the Twist Angles

The carbon atoms of a phenyl ring can be used to define a plane, namely the one they are all lying in. The angle between the such defined planes of two neighboring phenyl rings is called *twist angle*.For the measurements of the twist angles XCrysDen was used. Figure 1.6.9 illustrates the atoms used for twist angle measurements (light green colored). The atoms were selected from right to left (from substrate-side to vacuum-side).

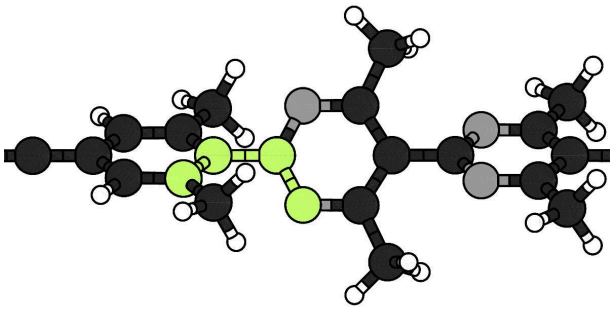

Figure 1.6.9: Illustration of atoms used for twist angle measurements. The atoms were selected from right to left (from substrate-side to vacuum-side).

Chapter 2

From Molecule to Quantum-well

In this chapter, the path from a single molecule to quantum-well structures in monolayers will be elucidated. The starting-point for this venture is a molecule with a Tour-wire based backbone and pyrimidine as shifting unit. To achieve bonding when used as a SAM on metal substrate, a thiol group is attached, separated from the backbone via a methyl-spacer group. Additionally, methyl side-chains are attached to the carbon atoms next to the nitrogens in the pyrimidine-rings, as well as to the carbon atoms in the backbone-ring closest to the nitrogen atoms of the pyrimidine-rings. In N_{down}, the nitrogens of the pyrimidine-rings pointing towards the thiol-bonding-group, in N_{up}, the nitrogens of the pyrimidine-rings pointing away from the thiol-bonding-group. The corresponding configurations are shown in Figure 2.0.1. In this chapter, often free-standing monolayers will be considered. The free-standing monolayer is a purely hypothetical case, since in reality a substrate, which is omitted here, is necessary for a monolayer to build up. The advantage of studying such a strictly hypothetical construct is, that the situation can be investigated without the influence of interface effects or other substrate induced influences. Of course, the monolayer has to be saturated, i.e. a hydrogen atom is bonded to the sulfur of the thiol group, to prevent problems in the simulation induced by the radical behavior of the unsaturated monolayer.

At first, the influence of changing the number of pyrimidine-rings as shifting units will be discussed (section 2.1). On the basis of the molecule in Figure 2.0.1 and a similar molecule without the methyl side-chains, structural effects will be discussed (section 2.2). The differences between the isolated molecule and a hypothetical free-standing monolayer

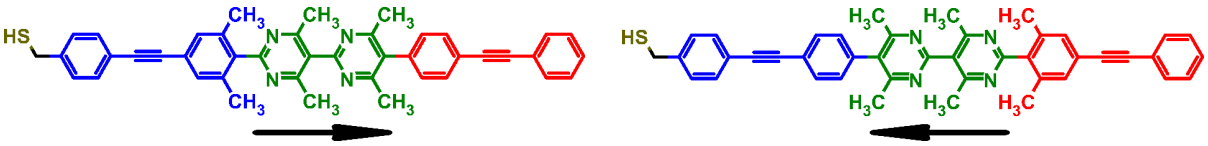

(a) N_{down} *(b) N_{up}*

Figure 2.0.1: Schematics of the basic molecule with Tour-wire based backbone, bi-pyrimidine as shifting unit and a methyl-spacer group between backbone and the thiol-bonding group. Colors indicate the segmentation into different units. The arrows indicate the directions of the dipole moments.

will be pointed out (section 2.3). In the context of the discussion of the SAM on metal substrate, interface effects, like Fermi-level pinning, and the influence of a geometry optimization on the full system are explained (section 2.4). The last point in this chapter will be the discussion of larger structures, namely cascades and quantum-wells (section 2.5). If not otherwise mentioned, the size of the unit cell used in this chapter is $2 * \sqrt{3} \times 3$.

2.1 Different Numbers of Shifting Units

The effect of inserting different numbers of pyrimidine rings into the backbone of the molecule shown in Figure 2.0.1a will be discussed.

Figure 2.1.1a shows the energies of the peaks of the frontier states of the SAM on metal substrate for a changing number of pyrimidine rings. The blue lines indicate peaks of the frontier states of the substrate-side unit while the red lines indicate the corresponding states on the vacuum-side units. Unoccupied states are depicted as dashed lines and occupied states as solid lines. The peaks selected for this plot are indicted by little arrows in the DOS plot in Figure 2.1.1b. From the energies in Figure 2.1.1a, one can clearly see that the energy difference between the highest occupied states of the substrate-side unit and the vacuum-side unit of the SAM increases with the number of pyrimidine rings. The energy difference between the lowest unoccupied states of the substrate-side unit and the vacuum-side unit for the SAM with three pyrimidine rings is lower than for the SAM with two pyrimidine rings. While the local gap of the particular units stays nearly constant with changing numbers of pyrimidine rings, the global gap decreases with an increasing number of shifting units. The SAMs with two and three pyrimidine rings exhibit Fermi-level pinning, as one can see from the density of states projected onto the substrate-side and vacuum-side units depicted in Figure 2.1.1b. Consequently, the global gaps for these two SAMs are almost the same.

In the free-standing monolayer the situation is quantitatively similar to the situation in the SAM. This can be verified by looking at the energies of the peaks of the frontier states of the free-standing monolayer for a changing number of pyrimidine rings in Figure 2.1.2a and at the density of states projected onto the substrate-side and vacuum-side units desplayed in Figure 2.1.2b. The energy differences between the highest occupied states of the substrate-side and vacuum-side units increases with the number of pyrimidine rings. For the lowest unoccupied states, the energy difference between the substrate-side and the vacuum-side units are nearly identical for the free-standing monolayers with two and three pyrimidine rings. The global gap strongly decreases with an increasing number of pyrimidine rings.

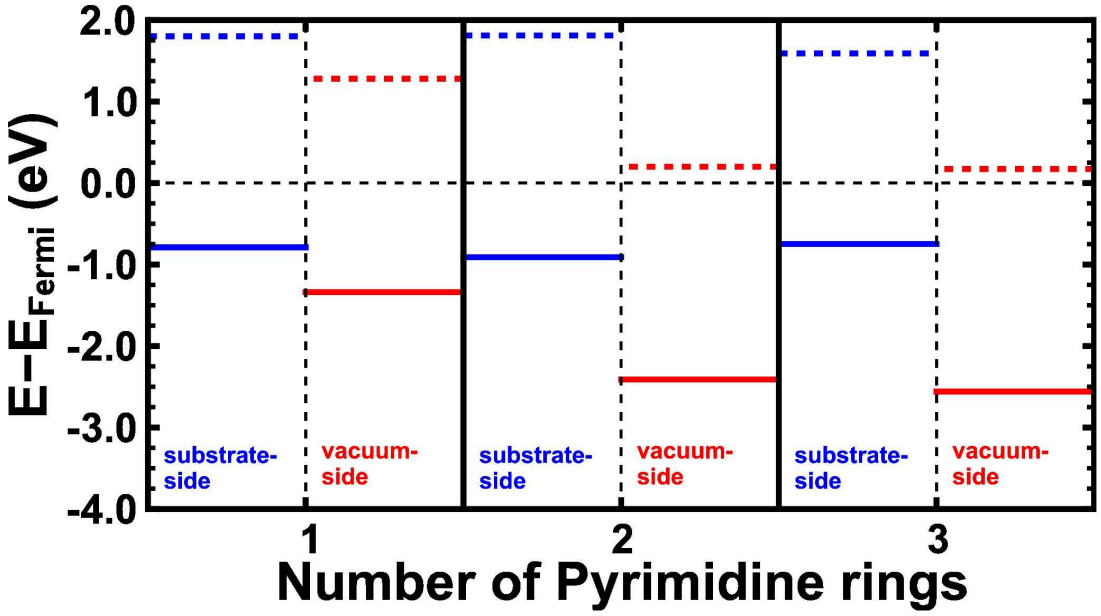

(a) Peak energies of the frontier states of the SAM

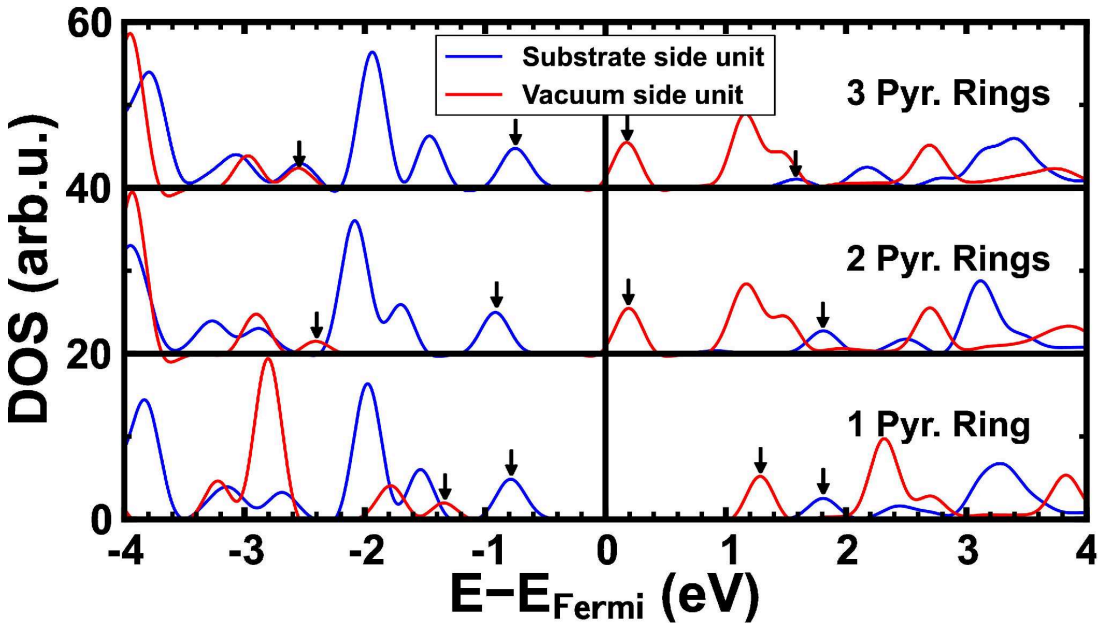

(b) DOS of SAM

Figure 2.1.1: (a) Energies of the peaks of the highest occupied (solid lines) and lowest unoccupied states (dashed lines) of the substrate-side (blue) and vacuum-side (red) units of the SAM on metal for a changing number of pyrimidine rings. (b) DOS projected on the substrate-side and vacuum-side units for the SAM on metal. In this plot, the small arrows indicate the peaks used for the extraction of the energy values depicted in (a).

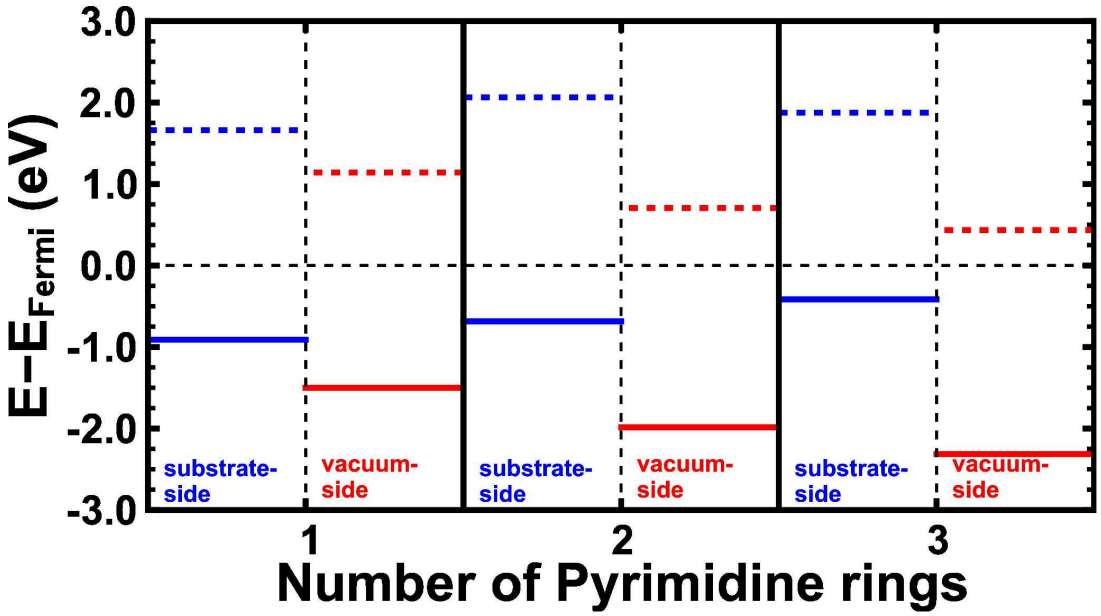

(a) Peak energies of the frontier states of the free-standing monolayer

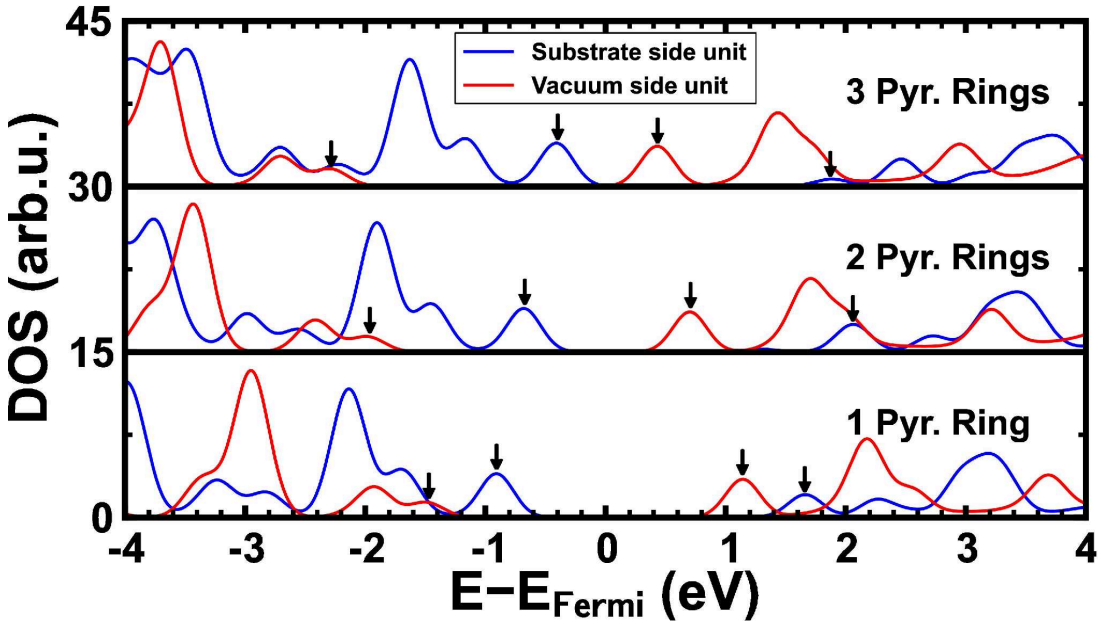

(b) DOS of free-standing monolayer

Figure 2.1.2: (a) Energies of the peaks of the highest occupied (solid lines) and lowest unoccupied states (dashed lines) of the substrate-side (blue) and vacuum-side (red) units of the free-standing monolayer for a changing number of pyrimidine rings. (b) DOS projected on the substrate-side and vacuum-side units for the free-standing monolayer. In this plot, the small arrows indicate the peaks used for the extraction of the energy values depicted in (a).

2.2 Structural Effects: Planar vs. Twisted

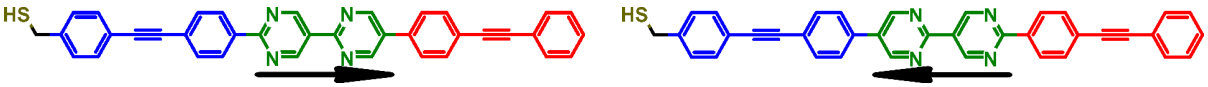

(a) N_{down} (b) N_{up}

Figure 2.2.1: Schematics of the molecule as in Figure 2.0.1 above but without the side-chains. Colors indicate the segmentation into different units. The arrows indicate the directions of the dipole moments.

Figure 2.2.1 shows the schematics of the "basic" molecules without the methyl substituents in N_{down} and N_{up} configuration. The chemical structure of the reference molecules in N_{down} and N_{up} configuration is shown in Figure 2.0.1. From these sketches of the chemical structures, the differences in the geometries of the planar and twisted molecules are not obvious. Since the geometries of all molecules were optimized with Gaussian03[42] using the PBE[43] functional and the 6-31G* basis set, these differences can be made clear by looking at the output geometries (for the construction of the unit cell from the Gaussian03[42] geometries see subsubsection 1.6.1.1). The input geometries for the molecules with methyl substituents, as well as for the molecules without methyl substituents, were planar. In the output geometries, large differences appear. While the molecules without methyl substituents stay planar, the substituents cause significant twists between the pyrimidine-rings and between the backbone and the pyrimidine-rings (see Table 2.1). These twists cause a breaking of conjugation. A closer look at the implications of a broken conjugation reveals two significant effects that affect the localization of the HOMO and LUMO. On the one hand, due to the broken conjugation, the wave-functions of the electrons cannot spread out over the whole backbone any more. This improves the localization. The second effect concerns the dipole moment of the bi-pyrimidine unit. Since electron flow between the pyrimidine-rings is prevented by the reduced conjugation, the dipole moment of the bi-pyrimidine is significantly increased. As a larger dipole moment results in a higher orbital shift in the backbones, the localization is further improved.

These structural effects, of course, are not of collective nature and, thus, already occur in the gas phase calculations. For a comparison of the isolated molecule and the free-standing monolayer see section 2.3. Collective electrostatic effects enhance especially the role of the dipole moment. In this section, the results for the hypothetically free-standing monolayers and SAMs on metal substrate are shown. The influence of interface effects is discussed later in section 2.4.

Table 2.1: Twist angles in the monolayers with side-chains as shown in Figure 2.0.1

Angle	Value N_{down}/ degrees	Value N_{up} / degrees
substrate side backbone - bi-pyrimidine	50.6	77.9
pyrimidine - pyrimidine	47.2	47.6
bi-pyrimidine - vacuum-side backbone	83.7	51.4

Figure 2.2.2 and Figure 2.2.3 show the electron potential energies and the Unit-DOS plots for the planar (a,c) and twisted (b,d) free-standing monolayer in the N_{down} and N_{up} configuration. From the electron potential energies, one can see that in N_{down} configuration the change in the vacuum energy ΔE_{vac} in the planar monolayer is $-0.76\,eV$, while for the twisted monolayer it is $-1.50\,eV$. In the N_{up} configuration, ΔE_{vac} has a value of $0.91\,eV$ for the planar monolayer and of $1.51\,eV$ for the twisted one. The huge differences in ΔE_{vac} between the planar and twisted monjolayers is equivalent to the difference in the dipole moments per unit cell. In N_{down} configuration, the dipole moment per unit cell for the planar monolayer has a value of $-1.82\,Debye$ and the dipole moment per unit cell of the twisted monolayer is $-3.60\,Debye$. The dipole moments per unit cell for the free-standing monolayers in N_{up} configuration are $2.21\,Debye$ for the planar one and $3.65\,Debye$ for the twisted monolayer. For comparison, the dipole moments of the N_{down} molecules in gas phase were calculated to be $-4.19\,Debye$ for the planar and $-6.96\,Debye$ for the twisted molecule. In gas phase, the dipole moments of the molecules in N_{up} configuration are $4.71\,Debye$ for the planar one and $6.88\,Debye$ for the twisted molecule. These dipole moments were calculated using Gaussian03[42] with the PBE[43] functional and the 6-31G* basis set. One can see that the magnitudes of the dipole moments decrease in the monolayers compared to the molecules in gas phase. This is due to a depolarization effect, i.e., the electric field caused by a molecular dipole layer induces a dipole moment in neighbouring molecules counteracting their intrinsic dipole moments.[49] A look at the plots of the Unit-DOS for the planar (c) and the twisted (d) geometry in Figure 2.2.2 and Figure 2.2.3 reveals that the localization , in N_{down} and N_{up} configuration, is improved for the monolayers with 6 methyl substituents. In contrast to the change in vacuum energy, the improvement of the localization is not solely caused by the larger dipole moment, but also, as explained above, by preventing the electron wave-functions from spreading out over the whole molecule as consequence of breaking the conjugation. The Unit-DOS also indicates the energetic shift of the highest occupied and lowest unoccupied orbitals of the vacuum-side unit (unit #3) compared to the substrate-side unit (unit #1). The peaks used to compute these energy differences are indicated by the black arrows in the Unit-DOS plots. For the planar monolayer in N_{down} configuration, the shift between the highest occupied states on the substrate-side and the vacuum-side is $-0.75\,eV$. The respective shift in the twisted monolayer in N_{down} configuration adds up to $-1.32\,eV$. The shift between the lowest unoccupied states on the substrate-side and the vacuum-side is $-0.67\,eV$ for the planar monolayer. For the twisted monolayer the corresponding shift assumes a value of $-1.36\,eV$. For the N_{up} configuration, the shifts of the highest occupied and lowest unoccupied orbitals have virtually the same magnitude as for the N_{down} configuration. From a comparison of the orbital shifts with the changes in vacuum energy it is clear, that these shifts closely follow the jump in the potential energy.

From the results presented above, it is evident that there are no qualitative differences between the N_{down} and N_{up} configurations as long as only free-standing monolayers and molecules in gas phase are considered.

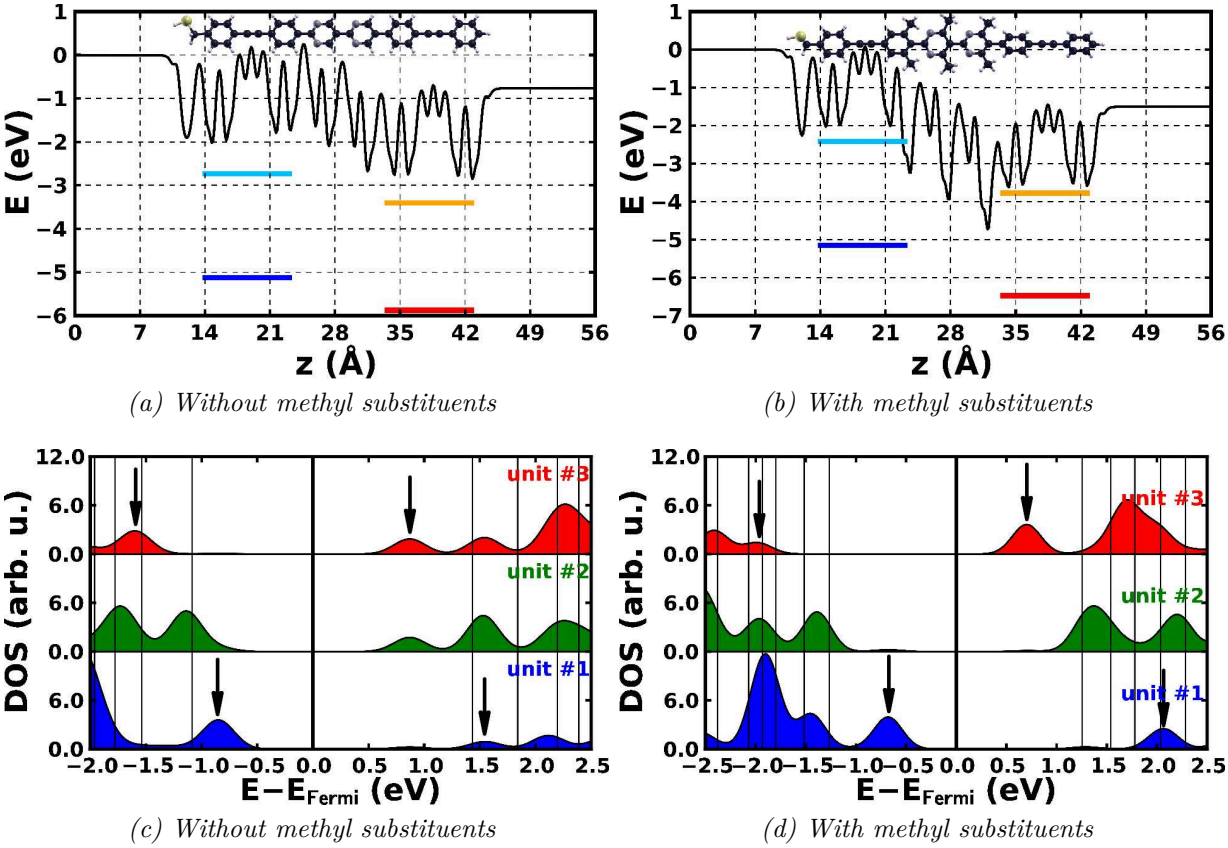

(a) Without methyl substituents

(b) With methyl substituents

(c) Without methyl substituents

(d) With methyl substituents

Figure 2.2.2: Electron potential energy of the free-standing monolayer without (a) and with 6 (b) methyl substituents. In these plots, the horizontal lines indicate the energies of the frontier states of the substrate-side and vacuum-side units. Unit-DOS of the free-standing monolayer without (c) and with 6 (d) methyl substituents. The vertical lines in the Unit-DOS plots indicate the energy intervals containing two electronic states. The arrows mark the peaks of those the energies are indicated in the potential energy plots and that were used to calculate the energy differences between frontier states of the substrate-side and vacuum-side units. The numbering and coloring of the units follows the color code in the sketches of the chemical structures in Figure 2.0.1 and Figure 2.2.1. All plots shown in this figure refer to the free-standing monolayers in N_{down} configuration.

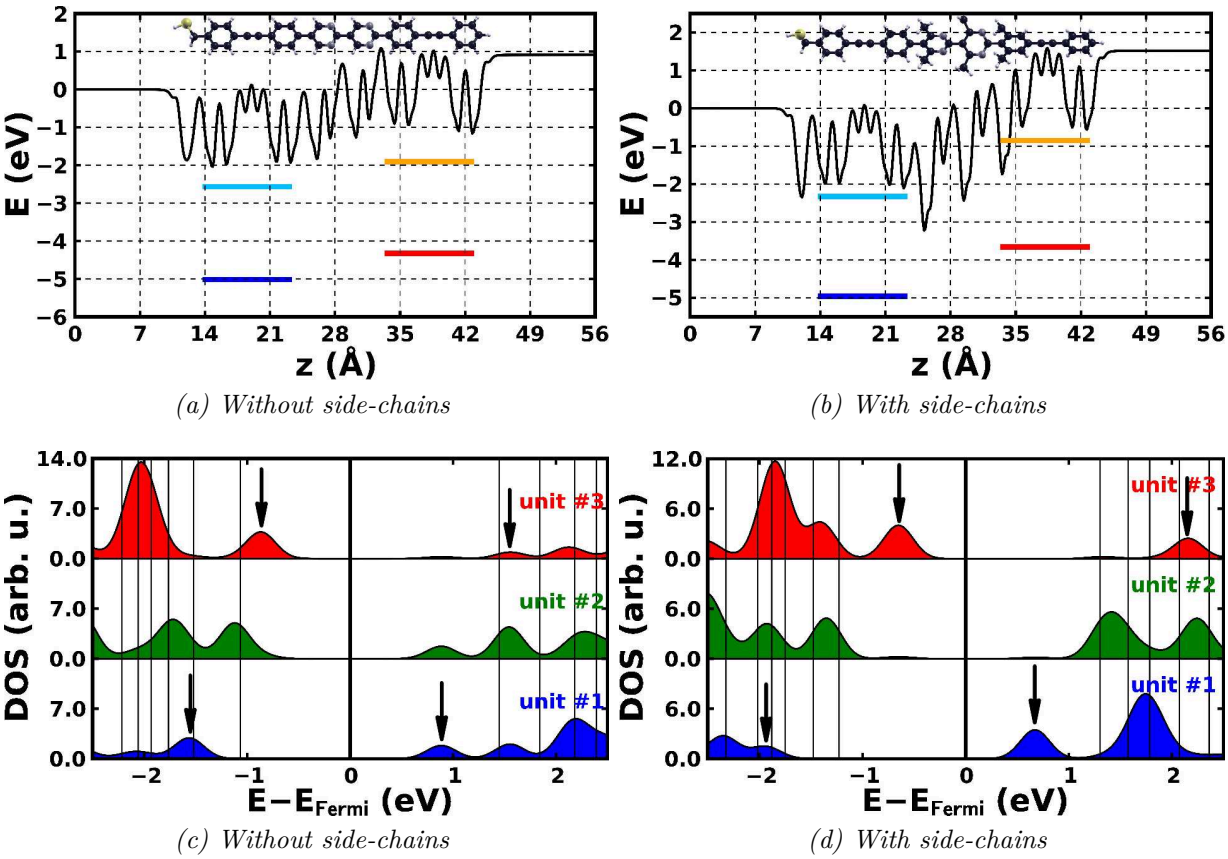

(a) Without side-chains

(b) With side-chains

(c) Without side-chains

(d) With side-chains

Figure 2.2.3: Electron potential energy of the free-standing monolayer without (a) and with 6 (b) methyl substituents. In these plots, the horizontal lines indicate the energies of the frontier states of the substrate-side and vacuum-side units. Unit-DOS of the free-standing monolayer without (c) and with 6 (d) methyl substituents. The vertical lines in the Unit-DOS plots indicate the energy intervals containing two electronic states. The arrows mark the peaks of those the energies are indicated in the potential energy plots and that were used to calculate the energy differences between frontier states of the substrate-side and vacuum-side units. The numbering and coloring of the units follows the color code in the sketches of the chemical structures in Figure 2.0.1 and Figure 2.2.1. All plots shown in this figure refer to the free-standing monolayers in N_{up} configuration.

In Figure 2.2.4 and Figure 2.2.5, (a) and (b) show the electron potential energies for the SAMs on the metal substrate without and with methyl substituents in N_{down} and N_{up} configuration respectively. The horizontal lines indicate the energies of the frontier states of the substrate-side and vacuum-side units. From these plots, one can see, for the N_{down} configuration, that the work-function modification as well as the energy difference between the frontier states on the substrate-side and vacuum-side unit are stronger for the SAM with the methyl substituents. In this configuration, the planar SAM induces a work-function modification of $-1.31\,\text{eV}$. The work-function modification of the SAM with the methyl substituents in N_{down} configuration is $-2.71\,\text{eV}$. In N_{up} configuration, the work-function modifications of both SAMs are $-0.17\,\text{eV}$.

The Unit-DOS plots for the SAMs are shown in Figure 2.2.4(c) and (d) for the N_{down} configuration and in Figure 2.2.5 (c) and (d) for the N_{up} configuration. The arrows indicate the peaks used to calculate the energy shifts between the frontier states of the substrate-side and vacuum-side units. In N_{down} configuration, the shift between the highest occupied state of the substrate-side unit (#1) and the vacuum-side unit (#3) is $-0.77\,\text{eV}$ for the planar SAM and $-1.49\,\text{eV}$ for the twisted SAM. For the systems in N_{up} configuration, the energy differences between the highest occupied states of the substrate-side unit (#1) and the vacuum-side unit (#3) are $+0.44\,\text{eV}$ for the planar one and $+0.78\,\text{eV}$ for the twisted system. The corresponding shifts for the lowest unoccupied states are $-0.67\,\text{eV}$ for planar and $-1.62\,\text{eV}$ for the twisted SAM in N_{down} configuration. The energy difference between the lowest unoccupied states of the substrate-side unit and the vacuum-side unit of the planar SAM in N_{up} configuration is virtually zero. The peak of the DOS projected onto the vacuum-side unit selected for the calculation of this energy difference has a very low density. Thus, it might not represent the lowest unoccupied state but a numerical artifact. For the twisted SAM in N_{up} configuration, the energy difference between the lowest unoccupied states of the substrate-side and the vacuum-side unit is circa $+0.30\,\text{eV}$.

Like for the free-standing monolayers, for both configurations the localization is much better in the SAM with the methyl substituents. For example, in N_{up} configuration, the LUMO of the planar SAM is localized on all three units. The Unit-DOS plots also show that in N_{up} configuration both SAMs exhibit Fermi-level pinning. In N_{down} configuration only the SAM with methyl substituents shows this behavior. Fermi-level pinning occurs when a frontier orbital, HOMO or LUMO, gets close to the Fermi-energy of the metal substrate. This will be discussed in more detail in subsubsection 2.4.1.1.

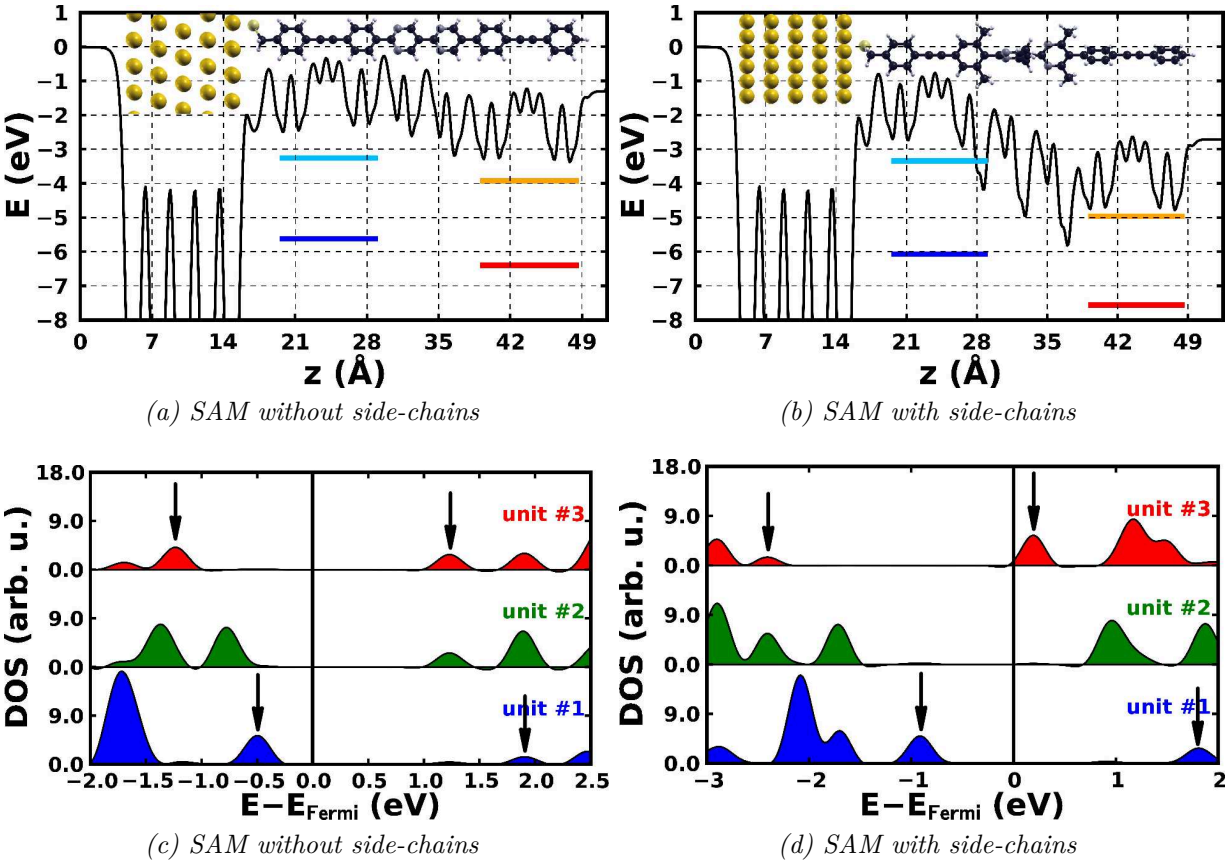

(a) SAM without side-chains

(b) SAM with side-chains

(c) SAM without side-chains

(d) SAM with side-chains

Figure 2.2.4: Electron potential energy of the SAM on metal substrate without (a) and with 6 (b) methyl substituents. In these plots, the horizontal lines indicate the energies of the frontier states of the substrate-side and vacuum-side units. Unit-DOS of the SAM without (c) and with 6 (d) methyl substituents. The arrows mark the peaks of those the energies are indicated in the potential energy plots and that were used to calculate the energy differences between frontier states of the substrate-side and vacuum-side units. The numbering and coloring of the units follows the color code in the sketches of the chemical structures in Figure 2.0.1 and Figure 2.2.1. All plots shown in this figure refer to the SAM in N_{down} configuration.

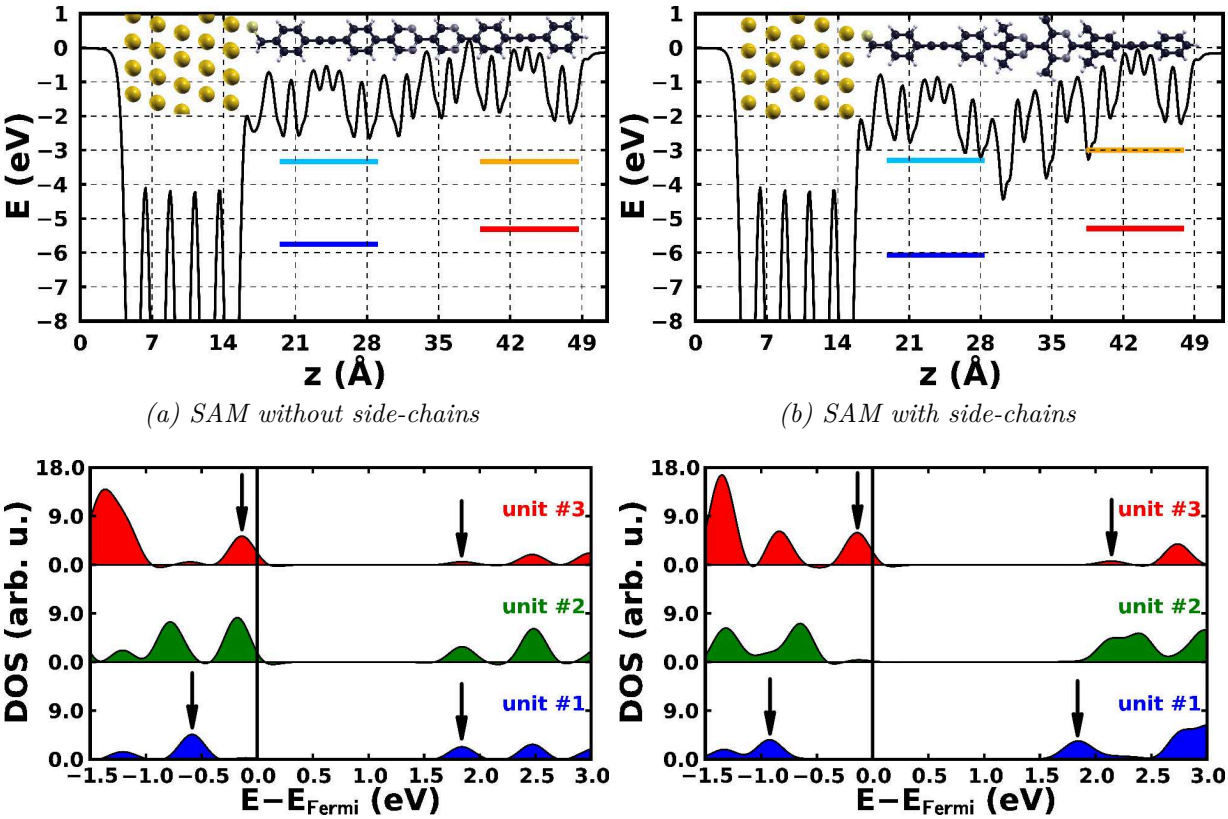

(a) SAM without side-chains

(b) SAM with side-chains

(c) SAM without side-chains

(d) SAM with side-chains

Figure 2.2.5: Electron potential energy of the SAM on metal substrate without (a) and with 6 (b) methyl substituents. In these plots, the horizontal lines indicate the energies of the frontier states of the substrate-side and vacuum-side units. Unit-DOS of the SAM without (c) and with 6 (d) methyl substituents. The arrows mark the peaks of those the energies are indicated in the potential energy plots and that were used to calculate the energy differences between frontier states of the substrate-side and vacuum-side units. The numbering and coloring of the units follows the color code in the sketches of the chemical structures in Figure 2.0.1 and Figure 2.2.1. All plots shown in this figure refer to the SAM in N_{up} configuration.

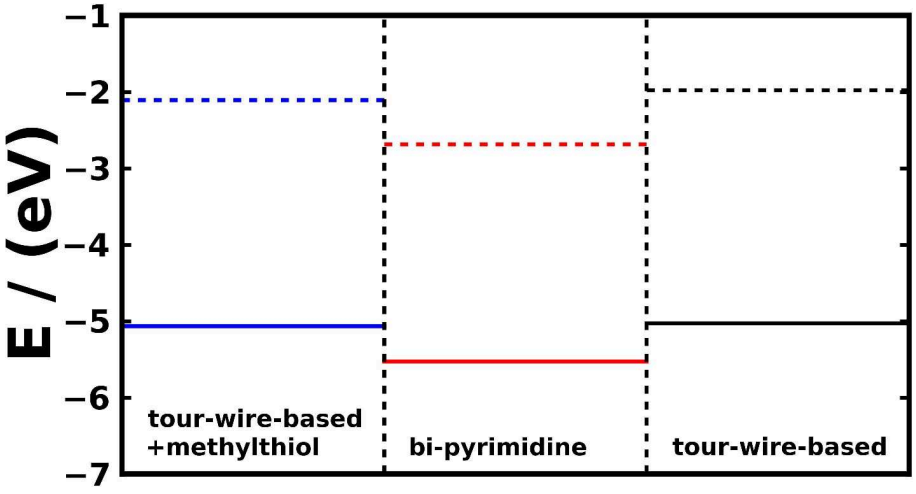

Figure 2.2.6: HOMO (solid lines) and LUMO (dashed lines) energies of the Tour-wire-based backbone unit with (blue) and without (black) methylthiol docking unit and of the bi-pyrimidine shifting unit (red).

Apparently, in the planar SAMs on the metal substrate and free-standing monolayers, the LUMO always extends onto the bi-pyrimidine unit. This can be explained by the very low lying LUMO of the bi-pyrimidine unit. Figure 2.2.6 shows the energies of the HOMOs (solid lines) and LUMOs (dashed lines) of the Tour-wire-based backbone unit with (blue) and without (black) methylthiol docking unit and of the bi-pyrimidine shifting unit (red). Clearly, the LUMO of the bi-pyrimidine unit has a significantly lower energy than the backbone units. In the planar systems, apparently, the energy shifts of the LUMOs of the backbone units are not strong enough to shift the LUMO of the respective unit below the LUMO of the bi-pyrimidine.

2.3 Isolated Molecule vs. Free-standing Monolayer

In this section, the behavior of the isolated molecule, i.e. the molecule in gas phase, is compared to the hypothetical free-standing monolayer. First, the results for the isolated molecule will be shown, followed by a brief discussion of the free-standing monolayer and finally a comparison of the two.

2.3.1 Isolated Molecule

As VASP[50] uses periodic boundary conditions, one has to use a large unit cell to simulate isolated molecules, since the potential energy has to reach the vacuum energy within the unit cell. For this calculations, the chosen unit cell had a length of 40 Å in x- and y-direction.

For a molecule in gas phase, the electron potential energy reaches the vacuum energy level at a certain distance from the molecule independent of the direction and therefore, per definition, ΔE_{vac} is zero.[30] In Figure 2.3.1 the DOS and Unit-DOS for the isolated molecules in N_{down} and N_{up} configuration are depicted. From the iso-density

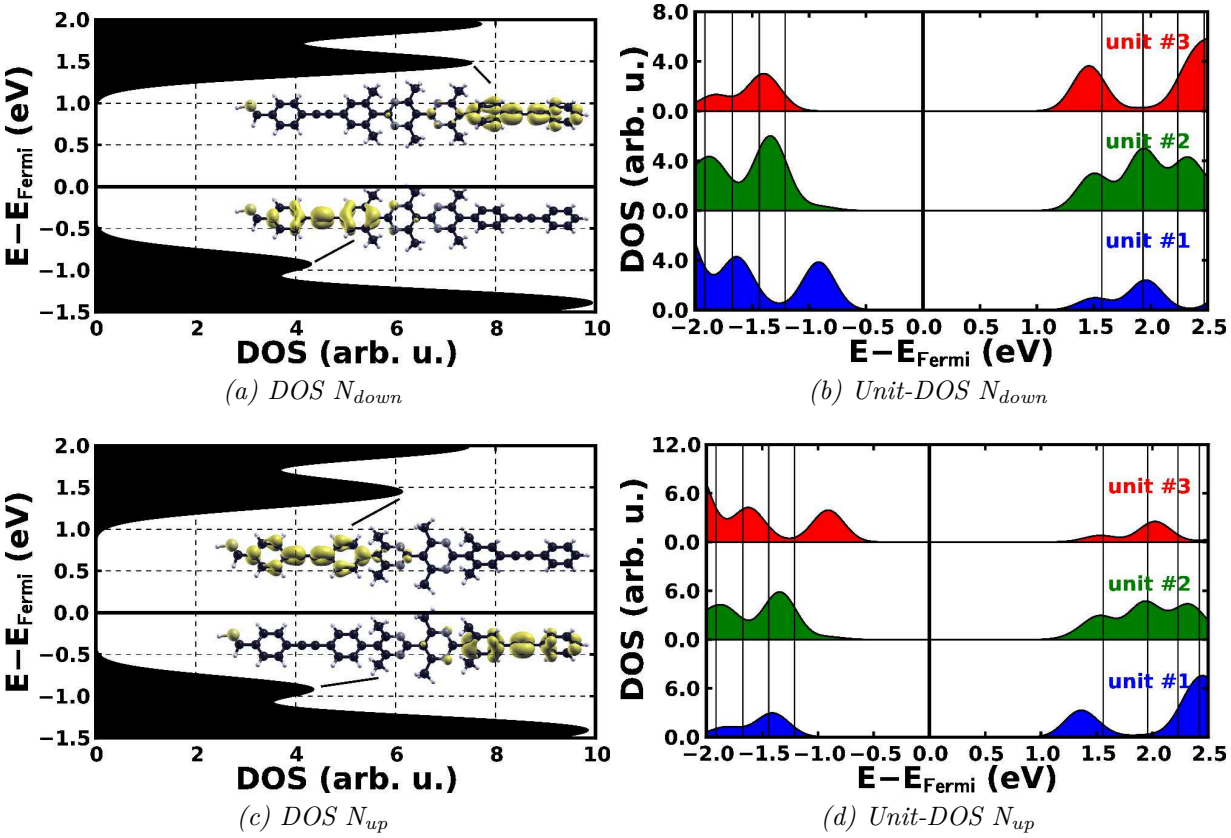

(a) DOS N_{down} (b) Unit-DOS N_{down}

(c) DOS N_{up} (d) Unit-DOS N_{up}

Figure 2.3.1: DOS and Unit-DOS of the isolated molecule in N_{down} and N_{up} configuration. Insets in the DOS plots show iso-density plots of the HOMO and LUMO. The vertical lines in the Unit-DOS plots indicate the energy intervals which contain two electrons. The numbering and coloring of the units follows the color code in the sketch of the chemical structures in Figure 2.0.1.

(Figure 2.3.1a) plots for the N_{down} configuration one can see, that the HOMO is localized on the substrate-side and the LUMO is localized on the vacuum-side. In the DOS, the peak corresponding to the LUMO (~1.5 eV) of this configuration is significantly higher than the HOMO-peak (~−0.9 eV). The reason for this is, that there are more overlapping states at the energy of the LUMO than at the HOMO energy. While the iso-density plots suggest a fairly good localization in the isolated molecule in N_{down} configuration, the Unit-DOS (Figure 2.3.1b) presents a slightly different picture. It shows that the energy interval corresponding to the HOMO and LUMO have densities on all three units. In the case of the HOMO, this density is very low on the vacuum-side unit (#3) and for the LUMO the substrate-side unit (#1) has less density than the other two units. The reasons for the two different pictures of the localization are that the HOMO and LUMO consist of a few overlapping bands, and, that for the iso-density plots, the LODS was calculated only for the highest occupied band and the lowest unoccupied band.

In the N_{up}-molecule, as is evident from the iso-density plots (Figure 2.3.1c), the HOMO is localized at the vacuum-side, while the LUMO is localized at the substrate-side. So,

HOMO and LUMO are localized on opposite ends compared to the N_{down} configuration. The DOS plot for the N_{up} configuration displays a similarity to the N_{down} case, namely, the LUMO-peak is higher than the HOMO-peak. This has the same reason as in the N_{down} case, i.e. different numbers of overlapping states at the energies of HOMO and LUMO. The Unit-DOS for the N_{up} structure (Figure 2.3.1d) illustrates that the HOMO and LUMO are not very well localized. This can be seen due to the vertical lines. These indicate the energy intervals containing two electronic states. All three units have at least a small amount of DOS in the intervals corresponding to the HOMO and the LUMO.

Altogether, it is evident that even in the isolated molecule the frontier orbitals are already slightly localized. This is due to the dipole moment of the bi-pyrimidine which shifts the orbitals in the backbone already in the single molecule situation.

2.3.2 Free-standing Monolayer

Within the free-standing monolayer, as well as within the SAM on metal substrate, the by-pyrimidine units build up a 2d dipole layer. This dipole layer divides the vacuum into 2 regions with different energies.[30] The results for the free-standing monolayers are already shown in section 2.2 (see Figure 2.2.2 on page 31 for the N_{down} configuration and Figure 2.2.3 on page 32 for the N_{up} configuration). Here, a short summary of the results will be given.

In the case of the N_{down} configuration the change in the vacuum energy ΔE_{vac} is circa $-1.50\,\text{eV}$. For the molecule with the nitrogen atoms pointing towards the vacuum-side (N_{up}), ΔE_{vac} is approximately $1.51\,\text{eV}$. The similarity of the magnitudes of these two values for the different configurations indicates that the influence from the dipole moment of the thiol group is rather insignificant in this case. The reason for the insignificant influence of the thiol group might be its orientation, which is influenced by the methyl spacer. The energy difference between the highest occupied orbital on the vacuum-side and the substrate-side is about $-1.32\,\text{eV}$ for the N_{down} configuration and circa $1.30\,\text{eV}$ for the N_{up} monolayer.

The localization of the HOMO and LUMO is quite good for both configurations, as is evident from the Unit-DOS plots in section 2.2. For the molecule in N_{down} configuration, the main part of the density of states of the HOMO is localized on the substrate-side unit (#1) and the LUMO is primarily localized in the vacuum-side unit (#3). The opposite is valid for the N_{up} monolayer, the HOMO is mostly localized on the vacuum-side unit (#3) and the LUMO is essentially localized on the substrate-side unit (#1). For both configurations, the HOMO and LUMO have a small amount of density of states on the middle unit (#2).

2.3.3 Comparison

The differences in the localizations for the HOMO and LUMO states between the isolated molecule and the free-standing monolayer are indicated in Figure 2.3.2 (for N_{down}) and Figure 2.3.5 (for N_{up}). These plots show the charge densities for the HOMOs and LUMOs of the molecule in gas phase and the free-standing monolayer as well as the differences

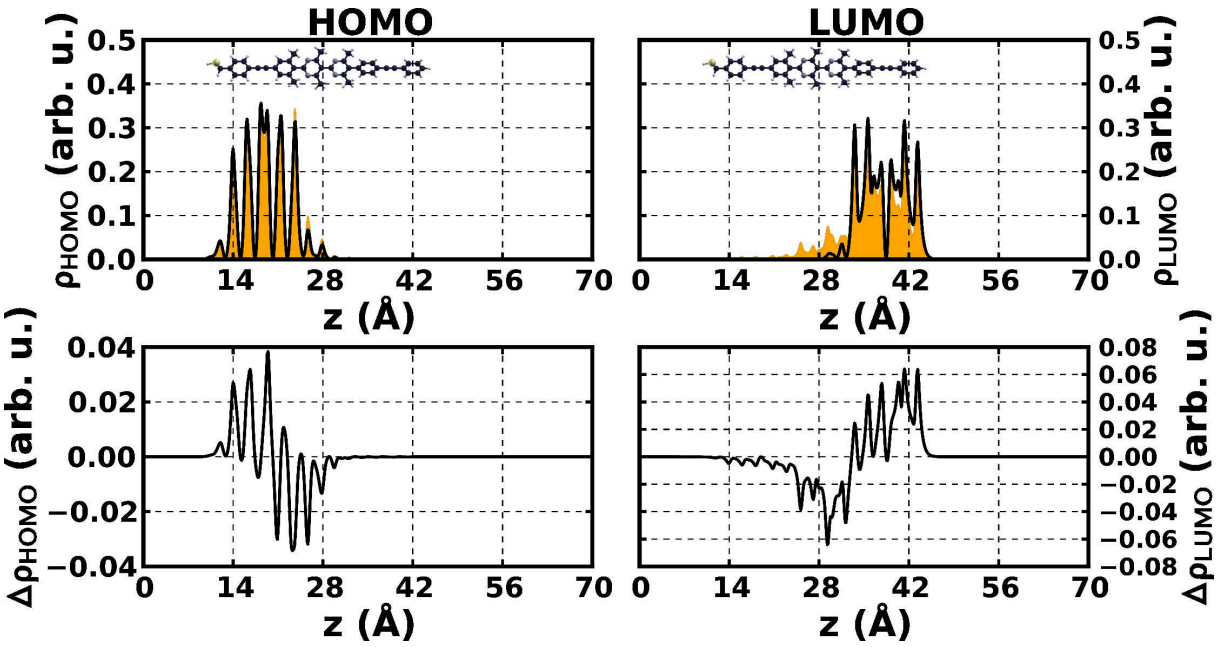

Figure 2.3.2: N_{down}: The upper plots show the charge densities integrated over the x-y-plane as a function of the position within the unit cell for the HOMO (left) and the LUMO (right) for the isolated molecule (orange shaded area) and the free-standing monolayer (black solid curve). For the HOMO and LUMO the charge densities of the highest occupied and the lowest unoccupied band were used. In the lower plots, the differences in the charge densities between isolated molecule and free-standing monolayer are depicted.

between the related charge densities. The highest occupied (lowest unoccupied) band was used to calculate the charge density of the HOMO (LUMO).

One short remark: using the term "charge density" for the description of unoccupied states is actually not quite accurate since unoccupied states actually have no charge. In this section, for reasons of convenience, the term "charge density" will, nevertheless, be used also for this case.

Figure 2.3.2 shows the situation for the N_{down}-monolayer. The localization of the HOMO is very similar for the isolated molecule and the free-standing monolayer, as can be seen in the left plots. The right plots indicate that the LUMO of the isolated molecule is somewhat more extended than the LUMO of the monolayer, which is localized on the vacuum-side. The lower two plots, depicting the charge density differences for HOMO and LUMO, illustrate that the influence of collective effects on the LUMO is stronger than on the HOMO. This can also be seen from the iso-density plots in Figure 2.3.3 and Figure 2.3.4. The first of these two figures shows the iso-density plots for the HOMOs of the free-standing monolayer and the isolated molecule. one can see that the HOMOs of the free-standing monolayer and the isolated molecule look very much alike. Figure 2.3.4 displays the iso-density plots for the LUMOs of the free-standing monolayer and the isolated molecule. Clearly, this way of representing the charge densities for the LUMOs confirms that the one of the isolated molecule extends more than the one of the free-standing monolayer.

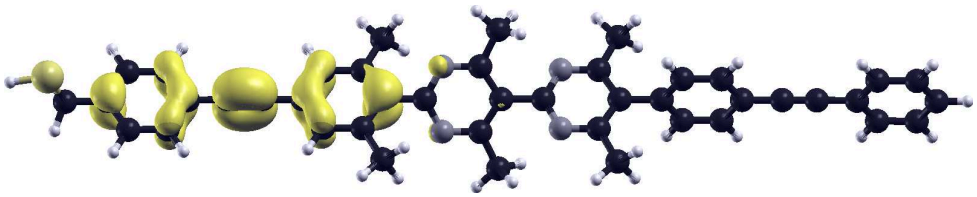

(a) Free-standing monolayer

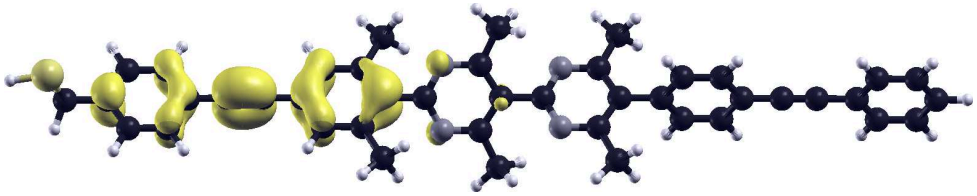

(b) Isolated molecule

Figure 2.3.3: N_{down}: iso-density plots for the HOMOs of the free-standing monolayer and the isolated molecule.

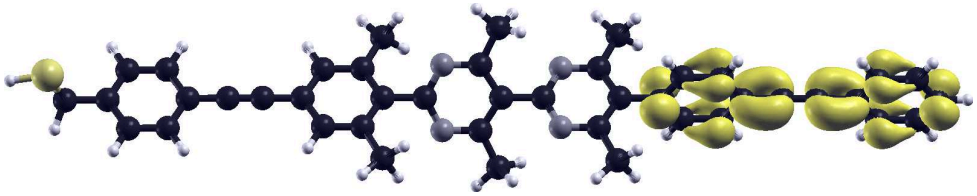

(a) Free-standing monolayer

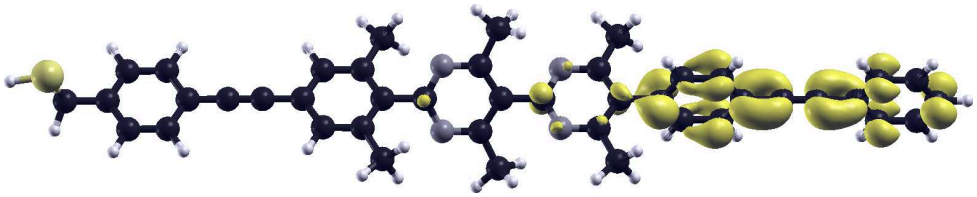

(b) Isolated molecule

Figure 2.3.4: N_{down}: iso-density plots for the LUMOs of the free-standing monolayer and the isolated molecule.

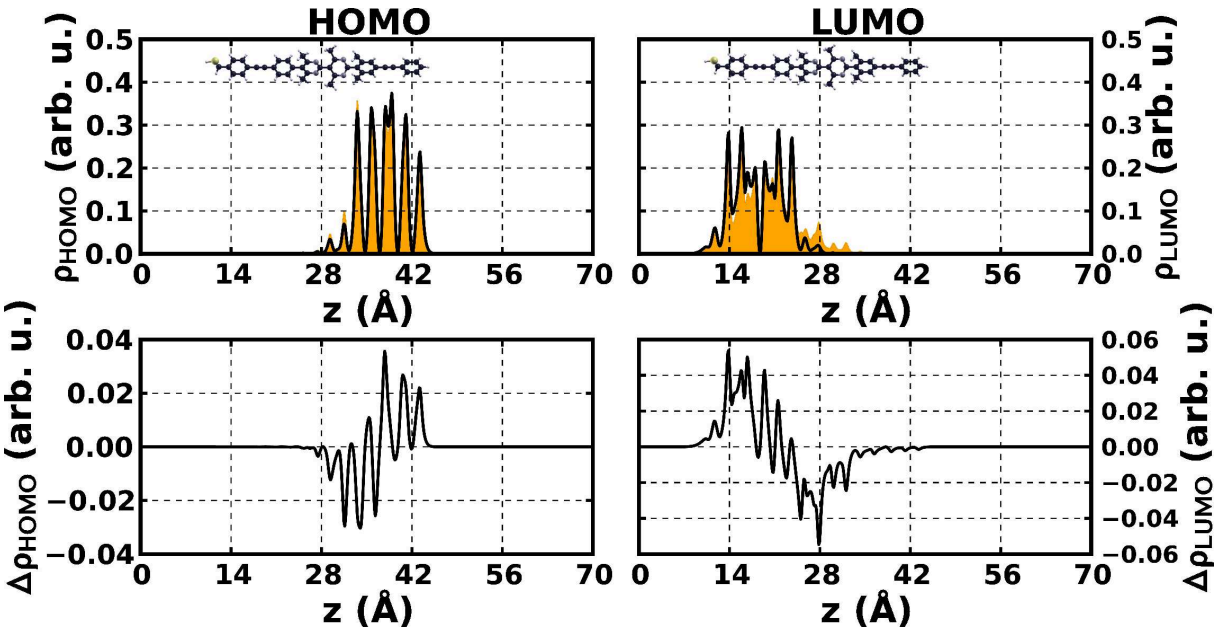

Figure 2.3.5: N_{up}: The upper plots show the charge densities integrated over the x-y-plane as a function of the position within the unit cell for the HOMO (left) and the LUMO (right) for the isolated molecule (orange shaded area) and the free-standing monolayer (black solid curve). For the HOMO and LUMO the charge densities of the highest occupied and the lowest unoccupied band were used. In the lower plots, the differences in the charge densities between isolated molecule and free-standing monolayer are depicted.

The situation is very similar for the N_{up} configuration (see Figure 2.3.5). Again, the HOMO is localized in a very similar way for the isolated molecule and the free-standing monolayer, while the LUMO extends more into the middle in the isolated molecule than in the free-standing monolayer. The lower plots indicate that the influence of collective effects on the localization of the LUMO is higher than on the localization of the HOMO, but a little bit lower than for the N_{down} configuration. Figure 2.3.6 and Figure 2.3.7 show the iso-density plots for the charge densities of the HOMOs and LUMOs of the free-standing monolayer and the isolated molecule in N_{up} configuration. One can see that they show the same results for the localization of these states as the plots of the integrated charge densities do.

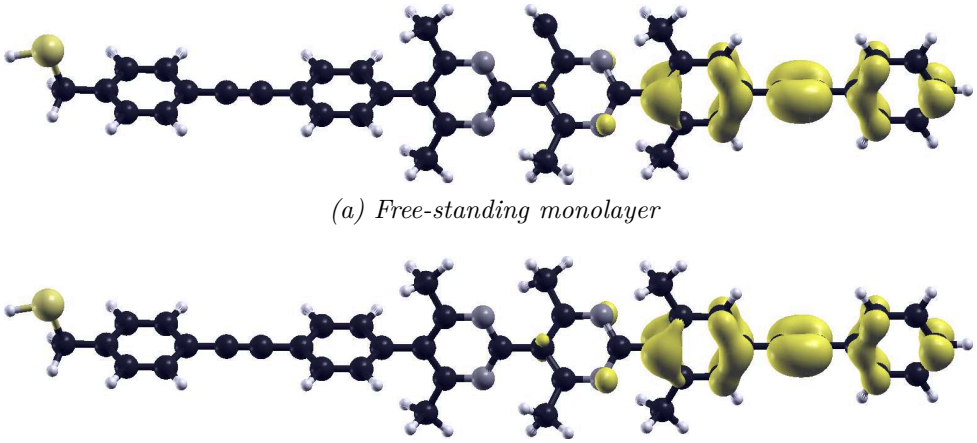

(a) Free-standing monolayer

(b) Isolated molecule

Figure 2.3.6: N_{up}: iso-density plots for the HOMOs of the free-standing monolayer and the isolated molecule.

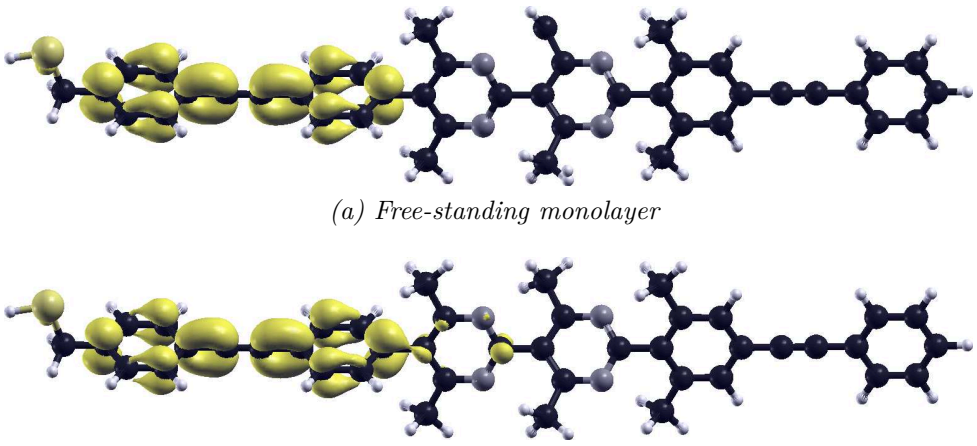

(a) Free-standing monolayer

(b) Isolated molecule

Figure 2.3.7: N_{up}: iso-density plots for the LUMOs of the free-standing monolayer and the isolated molecule.

The picture drawn by these plots seems to contradict the statements about the Unit-DOS's in the two sections above. This, however, can be clarified quite easily. While for the plots in this section, the charge densities were calculated just for the highest occupied and the lowest unoccupied bands, the peaks in the Unit-DOS plots can contain states from several bands. Therefore the Unit-DOS plots give a better overview over the complete situation concerning the localization, whereas the plots in this section establish a good understanding of the differences between isolated molecule and free-standing monolayer for individual states.

In contrast to the localization, the energetic shift of the orbitals is influenced strongly by collective electrostatic effects. For the N_{down} configuration, the energy difference between the highest occupied states on the vacuum-side unit and the substrate- side unit in the isolated molecule is about $-0.47\,eV$ and for the free-standing monolayer circa $-1.31\,eV$. The respective energy differences for the N_{up} configuration are approximately $0.51\,eV$ for the isolated molecule and roughly $1.30\,eV$ for the monolayer. Therefore, the orbital shift is enhanced by a factor of circa 2.8 for the N_{down} monolayer and about 2.5 for the N_{up} configuration due to collective electrostatic effects. This fact makes the need for collective effects for the engineering of molecular quantum-well structures evident, since in these quantum-well structures a good energetic separation of the frontier orbitals of spatially neighboring regions is mandatory.

2.4 SAM on Metal

Figure 2.4.1 shows the image of a SAM on metal substrate composed of a monolayer in N_{down} configuration on a Gold<111>-surface as substrate. The reason for the use of Gold as a substrate is that it is often used in experiments. As it is a metal with a lot of valence electrons, five layers of Gold atoms are sufficient to act as a metallic substrate in the calculations. The addition of a substrate in the calculations allows one to investigate interface effects such as Fermi-level pinning and charge rearrangements in the interface region.

The results for the SAMs on gold are shown in Figure 2.2.4 on page 34, b and d, for the N_{down} configuration and in Figure 2.2.5 on page 35, b and d, for the N_{up} configuration. The most important results will be shortly summarized here.

From the electron potential energies one can see, that for the N_{down} configuration the work-function modification $\Delta\phi$ is about $-2.71\,eV$ while for the N_{up} system it is approximately $-0.17\,eV$. Comparing these values with the changes in vacuum energy for the free-standing monolayers in section 2.2 it is evident that the magnitude of the work-function modification is much higher than the absolute value for ΔE_{vac}. Clearly, this means that an additional dipole moment occurs at the interface, since the only geometrical difference between SAM and free-standing monolayer is the addition of the substrate in the SAM. How the values for the work-function modifications differ from the ones for the changes in vacuum energy indicates a flow of electrons from the molecule into the substrate, leading to a partially positive charging of the organic parts. Therefore, the interface dipole points from the substrate to the organic part. The values for the change

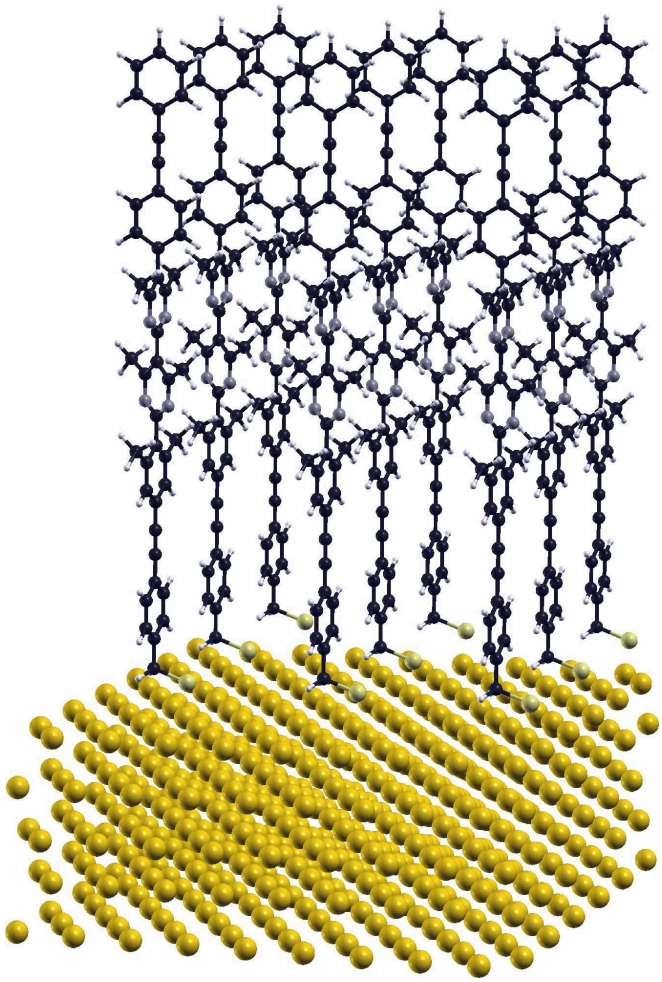

Figure 2.4.1: SAM on metal substrate composed of molecules in N_{down} configuration. The unit cell is repeated three times in the x- and y-directions.

of the work-function modification due to the interface dipoles are circa $-1.22\,\text{eV}$ for the N_{down} system and about $-1.65\,\text{eV}$ for the N_{up} SAM, these changes are called bond dipole. A more detailed discussion about the bond dipoles will follow in subsubsection 2.4.1.2. The influence of the interface dipole on the orbital shift between the highest occupied states on the substrate-side and the vacuum-side depends on the orientation of the dipole moments in the organic parts of the SAM. As one can see from the Unit-DOS plots in the sub-figures (b) and (d), the shift of the highest occupied state between the vacuum-side and the substrate-side for the N_{down} system is about $-1.50\,\text{eV}$, compared to $-1.32\,\text{eV}$ in the free-standing monolayer, and the shift for the N_{up} SAM is circa $0.78\,\text{eV}$, compared to $1.30\,\text{eV}$ for the monolayer.The different behavior of the two different configurations can be explained by another interface effect, so-called Fermi-level pinning. In detail this will be discussed in subsubsection 2.4.1.1. Briefly, when the orbitals are shifted and get energetically near to the Fermi-energy of the substrate, they can not be "shifted further" as establishing thermodynamic equilibrium triggers charge rearrangements. From the Unit-DOS plots it is evident that both configurations exhibit this pinning on the vacuum-side

unit (#3), in the case of the N_{down} SAM the lowest unoccupied orbital gets pinned while for the N_{up} system the highest occupied orbital displays this pinning behavior.

The Unit-DOS plots also indicate that, for the N_{down} configuration the HOMO is localized on the substrate-side, while the LUMO is localized on the vacuum-side. For the N_{up} SAM, the HOMO is clearly localized on the vacuum-side and the LUMO on substrate-side. Both configurations display an excellent localization behavior, similar to the free-standing monolayer.

2.4.1 Interface Effects

In this subsection two important interface effects will be discussed, namely *Fermi-level pinning* and the *bond dipole*.

2.4.1.1 Fermi-level pinning

This subsection builds on references [44] and [45].

Fermi-level pinning occurs when the HOMO or LUMO of the organic part of a SAM is shifted to the Fermi energy of a metallic substrate. If this happens, charge rearrangements between the involved molecular orbital and the metal take place, causing a dipole moment. When the HOMO is shifted up in energy and reaches the Fermi energy of the substrate, electrons from the HOMO will flow into the substrate and it cannot be shifted to above the Fermi-level as long as it is at least partially filled. On the other hand, if the LUMO of a SAM is shifted down in energy, as soon at it reaches the Fermi energy, the SAM gets polarized. This polarization, prevents the LUMO from getting shifted below the Fermi-level. Of course, this happens not only when the orbitals are shifted due to internal or external electric fields. Also, when HOMO or LUMO energy, i.e., the ionization potential or the electron affinity, of the unbound organic molecule has a value near the Fermi-level of the metallic substrate, it can get shifted to the Fermi-level due to the bond dipole. For the molecules used in this work, the bond dipole is caused by a charge transfer bewteen the sulfur and the substrate, as discussed in the next subsection.

In the Unit-DOS plots in section 2.2 the black vertical lines at 0.0 eV indicate the Fermi energies of the systems with twisted monolayers. One can see in Figure 2.2.4 on page 34, that for the N_{down} SAM the Fermi energy cuts the DOS of the lowest unoccupied state of the vacuum-side unit (#3). This is an indicator for the occurrence of Fermi-level pinning, in this case for a LUMO-level pinning. A look at the Unit-DOS of the N_{up} system (Figure 2.2.5 on page 35) reveals that in this system Fermi-level pinning occurs, too. Again, like for the N_{down} case, the vacuum-side unit (#3) exhibits this behavior, but this time it is HOMO-level pinning since the DOS of the highest occupied state of the vacuum-side unit cuts the energy. In these two cases, no charge transfer into the pinned states occurs. This will be explained in the next subsection about the bond dipole.

2.4.1.2 Bond Dipole

This subsection builds on reference [49].

The bond dipole (BD) is a result of two effects. On the one hand, charge rearrangements at the interface, caused by the replacement of the S-H bond of the docking group of the organic molecule through a S-Au bond with the surface, lead to an interface dipole. This effect occurs always when a molecule bonds to a metal substrate. On the other hand, in the case of Fermi-level pinning the bond dipole is affected by a polarization of the SAM, like it is the case for the SAMs discussed above. In spite of its name, the bond dipole actually is not a dipole but an energy. It is the energy by which the work-function modification gets changed due to the bonding process. This can be expressed in the following equation:

$$\Delta\Phi = BD + \Delta E_{vac} \tag{2.4.1}$$

The sign of the interface dipoles and, thus, the sign of BD depend on the direction of the charge transfer between substrate and organic molecule due to bonding. If electrons flow from the organic molecule to the substrate, the organic part will be partially charged positively. Therefore, the interface dipole points from the substrate to the organic molecule. In this case, the bond dipole will be negative and a decrease of the work-function modification will occur.

All of the systems discussed here exhibit Fermi-level pinning. These systems show a more interesting behavior in terms of charge rearrangements and polarization compared to systems that do not exhibit Fermi-level pinning. Discussions of charge rearrangements in systems without Fermi-level pinning behavior can be found ,e.g., in references [49] and [45].

Figure 2.4.2 and Figure 2.4.3 show the charge rearrangements $\Delta\rho$ (upper plots), the charge transfer Q (middle plots) and the change in the electrostatic potential energy ΔE (lower plots) due to the bonding process as a function of the z-coordinate for the systems in N_{down} and in N_{up} configuration. The transparent insets indicate the position of the SAM. The charge transfer Q at a certain point is the integral of the charge rearangements $\Delta\rho$ from the substrate side up to this point. A positive value of Q indicates a charge transfer from the vacuum-side to the substrate-side. For both configurations, the strongest charge rearrangements occur in the interface region, as is evident from the upper and middle plots. From these plots, one can see that charge rearrangements within the organic part occur, leading to a polarization of the monolayer. These charge rearrangements are caused by the Fermi-level pinning which occurs in both SAMs, as discussed above. The change in the electrostatic potential energy ΔE (lowest plots) drops at the interface but also slowly within the organic parts. Thus, it confirms the polarization of the SAM seen in the upper and middle plots. In the lowest plots, the bond dipole is indicated by the label BD and the black vertical line. For the N_{down} configuration the BD has a value of circa $-1.22\,\text{eV}$ and for the N_{up} configuration it is about $-1.65\,\text{eV}$.

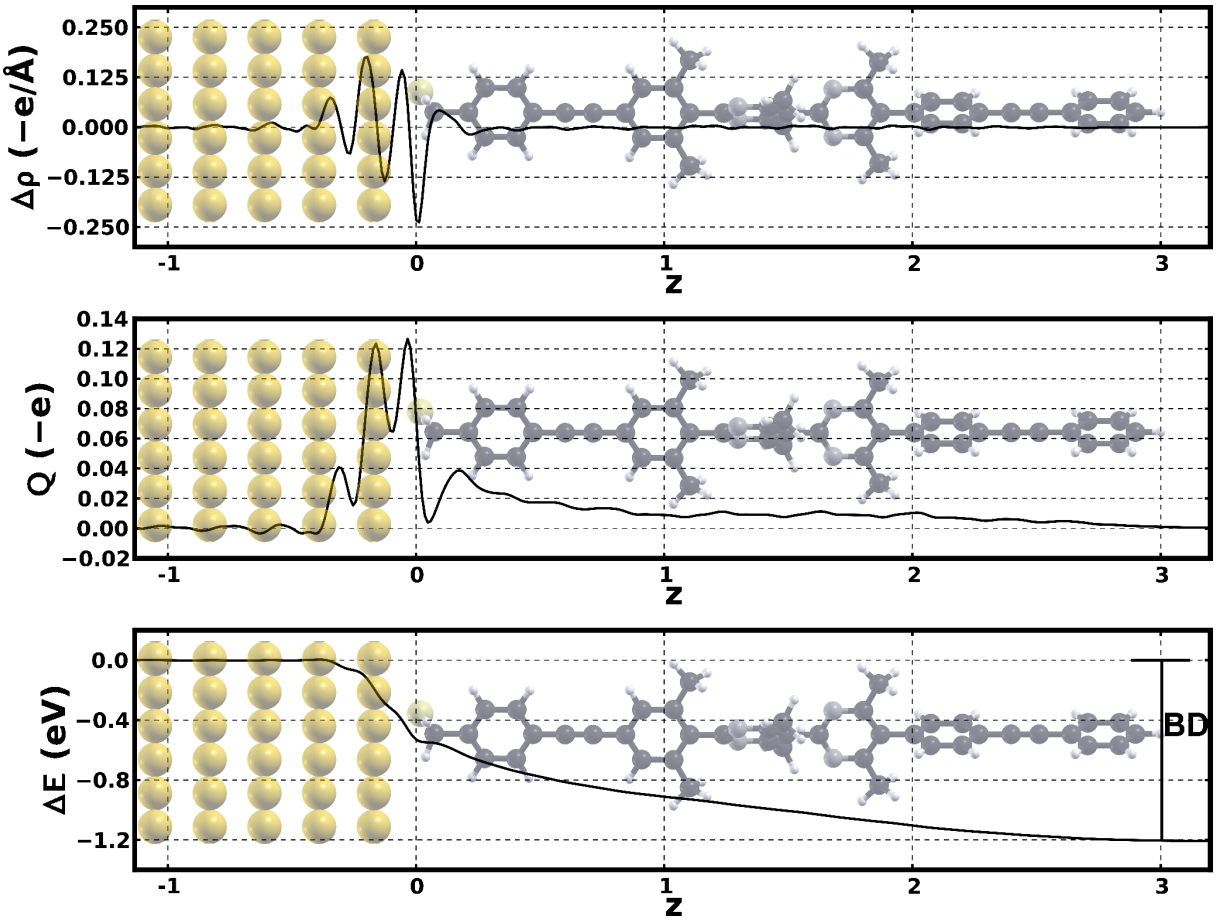

Figure 2.4.2: Plane integrated charge rearrangements $\Delta\rho$ (upper plot), charge transfer Q (middle plot) and change in electrostatic potential energy due to the charge rearrangements ΔE (lower plot) of the N_{down} SAM

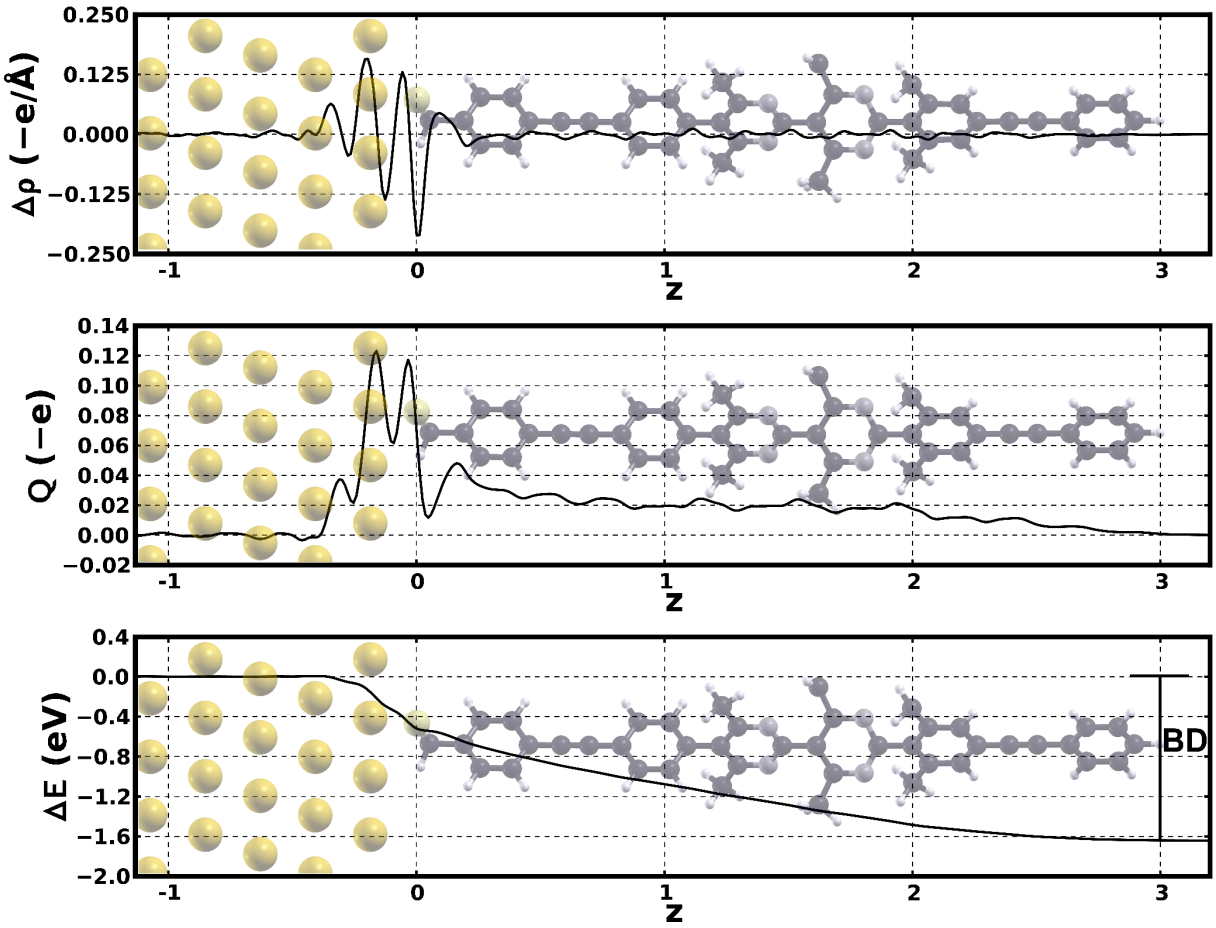

Figure 2.4.3: Plane integrated charge rearrangements $\Delta\rho$ (upper plot), charge transfer Q (middle plot) and change in electrostatic potential energy due to the charge rearrangements ΔE (lower plot) of the N_{up} SAM

Clearly, the BD can change the work-function modification quite dramatically and, therefore, has to be taken into account when investigating interfaces. Since the focus of this work lies rather on the design of new molecules than on the investigation of interfaces, and because the interface effects do not change the qualitative behavior of the systems, mostly the situations of free-standing monolayers will be discussed from now on (except for the next subsection).

2.4.2 Fully optimized SAM

The full geometry optimization of the SAM on metal substrate was done with the GADGET[53] optimizer for VASP[50]. The first three Gold layers were fixed while the other two layers as well as the organic part were relaxed. Due to the large unit cell necessary because of the side-chains, the optimization leads to a very high tilt angle of the organic parts compared to the surface normal. It was calculated by using the vector from the first carbon atom of the substrate-side backbone unit to the last carbon atom of the vacuum-side backbone unit. The value of the tilt angle was determined to be 68.8°. The twist angles had the following values (in brackets are the values for the only gas phase optimized monolayer):

- between the substrate-side backbone unit and the first pyrimidine-ring: 57.5° (gas phase optimized: 50.6°)
- between the two pyrimidine-rings: 56.5° (gas phase optimized: 47.2°)
- between the second pyrimidine-ring and the vacuum-side backbone unit: 59.1° (gas phase optimized: 83.7°)

One can see that the twist angles of the optimized SAM are similar to the ones of the gas phase optimized monolayer with the exception of the one between the second pyrimidine-ring and the vacuum-side backbone unit. The reason for this change is that, due to the high tilt angle, the effective package density is increased in the optimized SAM.

Figure 2.4.4 shows the Unit-DOS's of the fully optimized SAM (a) and the non-optimized SAM (b). Basically the molecular HOMO is still localized on the substrate-side unit (#1) and the LUMO remains mostly localized on the vacuum-side unit (#3). In addition both, HOMO and LUMO, have now a low density of states on the bi-pyrimidine unit (#2). There also seems to be a very low density of states between the HOMO and the LUMO on the bi-pyrimidine for which no explanation can be given at the moment. The shifts of the orbitals is much lower in the optimized SAM than in the non-optimized one due to the high tilt angle. The explanation for the decrease of orbital shifts for increasing tilt angles is that the z-component of the dipole moment gets smaller. For the optimized SAM, the energetic shift of the highest occupied state on the vacuum-side unit compared to the corresponding state on the substrate-side unit is about $-0.43\,\mathrm{eV}$. This is a little bit less than a third of the value in the non-optimized SAM for which it is circa $-1.50\,\mathrm{eV}$. For comparison, the corresponding shift for the isolated molecule in $\mathrm{N_{down}}$ configuration is about $-0.47\,\mathrm{eV}$. A direct consequence of the lower orbital shift is that no Fermi-level pinning occurs in the optimized system in contrast to the non-optimized one. From the

UnitDOS's it is also evident that the electronic structure changes very much due to the different geometry. The global gap in the optimized SAM is much larger than in the non-optimized system. For the optimized system the energy gap has a value of about 2.25 eV which is about double as high than for the non-optimized SAM that has a gap of circa 1.11 eV. Of course, the larger global gap is also a direct consequence of the lower orbital shift. The high tilt angle also causes a dramatic reduction of the work-function modification $\Delta\Phi$. While the non-optimized SAM exhibits a work-function modification of about -2.71 eV it is reduced to less than half of this value, namely to -1.32 eV, in the optimized system.

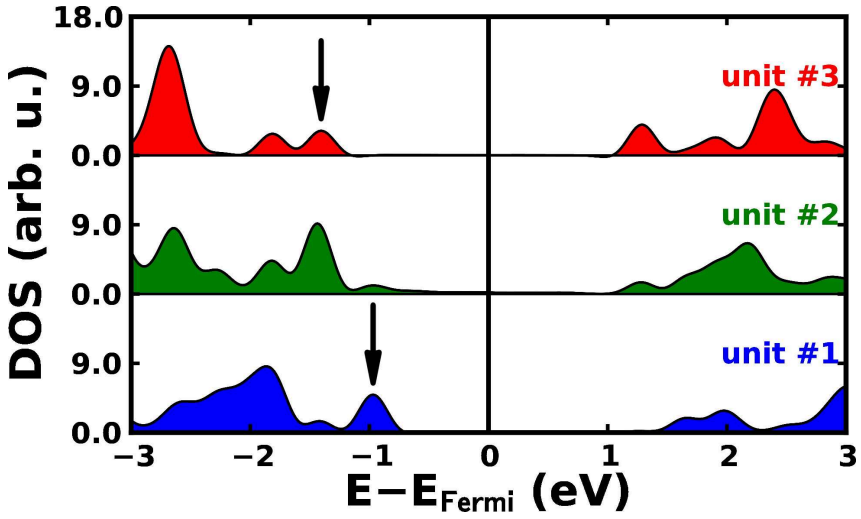

(a) Optimized SAM

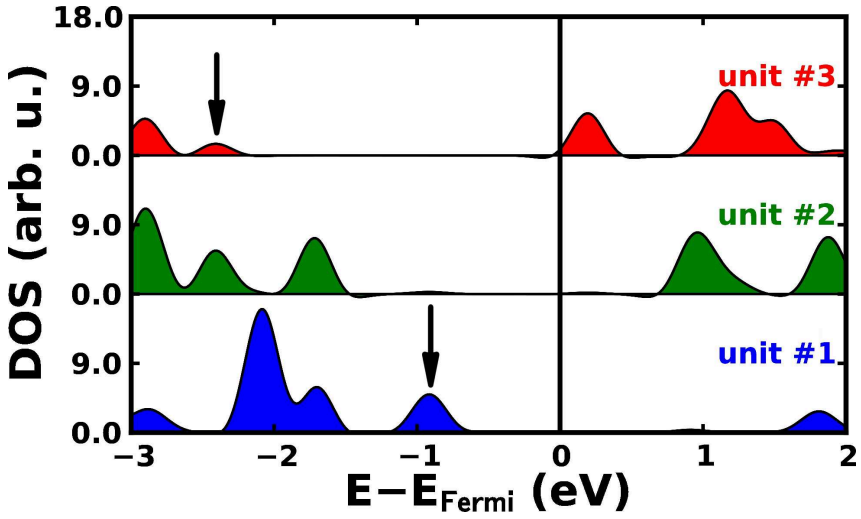

(b) Non-optimized SAM

Figure 2.4.4: Unit-DOS plots for the optimized SAM (a) an the non-optimized SAM (b). The black arrows indicate the peaks used to calculate the orbital shifts. The numbering and coloring of the units follows the color code in the sketch of the chemical structure in Figure 2.0.1.

From this it is obvious that the geometry has a big influence on the electronic properties of the monolayer but one has to take into consideration, that in the present case the packing density is quite low due to the large unit cell. Finding a smaller unit cell to increase the packing density will lead to results more similar to the non-optimized SAM. The principal effects that are investigated in this work, namely the localization and the orbital shifts, get weakened but not obliterated due to the geometry optimization. Therefore, investigations of non-optimized monolayers will still lead to quite reasonable results, at least in the limit of ideal conditions, and so the computationally expensive task of optimizing the geometries of SAMs was limited to a few selected systems.

2.5 Larger Structures

So far, it has been demonstrated that a bi-pyrimidine layer build into a Tour-wire based backbone can be used to shift the frontier orbitals of the backbone segments due to its dipole moment. As a next step, the effects of building two bi-pyrimidine layers separated by a backbone segments into a monolayer will be discussed. Obviously, there are four possibilities to arrange two separate dipole layers into a monolayer. There exist two possibilities for arrangements in which the dipole moments point in the same direction, resulting in cascade-like structures, and also two possibilities to arrange the dipole moments pointing in opposite directions. these arrangements result in quantum-well-like structures. Calculations for all four arrangements have been carried out and the obtained results are presented in this section. Since in the previous sections it became clear, that interface effects do not qualitatively change the situation and to exclude influences from e.g. Fermi-level pinning, in this section only results for free-standing monolayers will be shown.

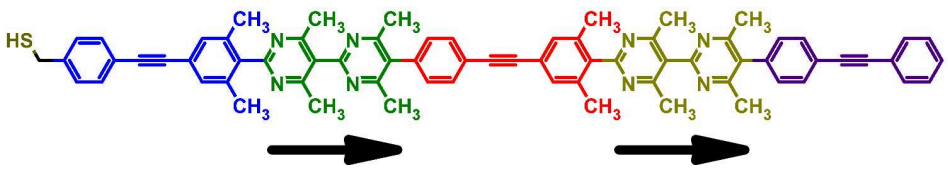

(a) N_{down}

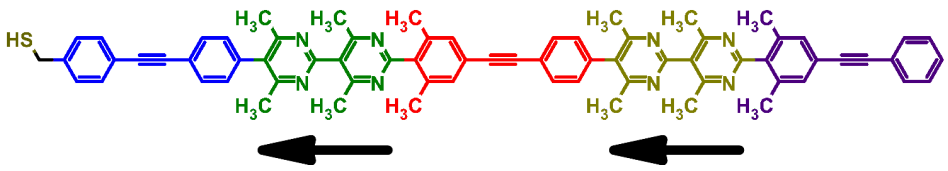

(b) N_{up}

Figure 2.5.1: Schematics of cascade structures. The colors indicate the segmentation into different units. The small arrows indicate the directions of the dipole moments.

2.5.1 Cascade

The cascade-like structures in this work consist of two dipolar layers with dipole moments pointing in the same direction. This dipole layers are separated by a backbone segment. Basically, these structures just represent larger versions of the molecules discussed above. Figure 2.5.1 shows the schematics of the two cascades, one where the dipole moment points from the substrate-side to the vacuum-side and one where the dipole moments point from the vacuum-side to the substrate-side, in analogy to the nomenclature for the basic molecules they are called N_{down} and N_{up}.

The two cascade structures have a few things in common and show a behavior similar to the reference monolayer. For one, due to the dipole moments pointing in the same direction, the orbital shifts and jumps in the vacuum energies are stronger than in the reference molecule. The electronic structures of the both cascades exhibit a stair like characteristics, which is of course not surprising since this is the main feature of a cascade. Another common feature of the two cascade structures is that the global molecular gap gets very narrow. This is due to the fact that the sum of the two dipole moments in each structure cause a shift of the orbitals that is of the same magnitude as the gap of the backbone segments. Since the use of the PBE[43] functional for the calculations leads to an underestimated gap while the dipole moments are described accurate, this closure of the gap should not occur already for two dipole layers in the actual systems.

2.5.1.1 N_{down}

For the N_{down} cascade structure, the dipole moments point away from the surface. Figure 2.5.2 shows the electron potential energy (a), the Unit-DOS (b) and a contour map of the local density of states (LDOS). The vertical lines in the Unit-DOS plot indicate the energy intervals containing two states. From the electron potential energy one can see that the change in vacuum energy is about $-2.20\,\mathrm{eV}$. Therefore, the magnitude of ΔE_{vac} is circa $0.70\,\mathrm{eV}$ higher than for the basic N_{down} monolayer with only one dipole layer (see subsection 2.3.2). A higher change in the vacuum energy is prevented by the closure of the global gap and by Fermi-level pinning. From the Unit-DOS plot, one can see that the HOMO and the LUMO exhibit Fermi-level pinning behavior in this case. The energy difference between the highest occupied orbitals of the central unit (#3) and the substrate-side unit (#1) is approximately $-0.99\,\mathrm{eV}$ while the difference between the highest occupied orbitals of the vacuum-side unit (#5) and the central unit (#3) is circa $-1.13\,\mathrm{eV}$. In total this results in an energy difference between the highest occupied orbitals of the vacuum-side unit (#5) and the substrate-side unit (#1) of about $-2.12\,\mathrm{eV}$. Thus, the total energy difference between the highest occupied orbitals on the vacuum-side and the substrate-side closely follows the jump in the vacuum energy, in analogy to the monolayer in subsection 2.3.2. In contrast, the energetic shifts between the substrate-side unit and the central unit as well as between the central unit and the vacuum-side unit are lower than for the basic monolayer discussed in subsection 2.3.2.

From the plots for the Unit-DOS and the LDOS map it gets clear that the global HOMO is localized on the substrate-side unit (#1) and the global LUMO is confined on the vacuum-side unit (#5). They also reveal the stair-like electronic structure, which is a defining feature of cascade structures. One can also see the closure of the gap. Since

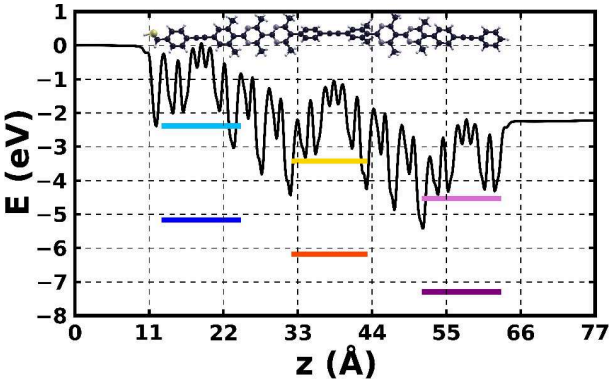

(a) Electron potential energy

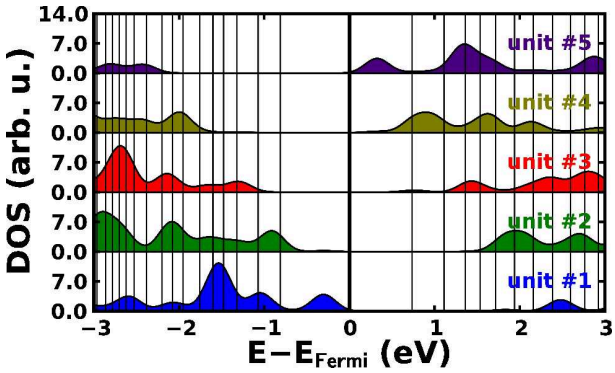

(b) Unit-DOS

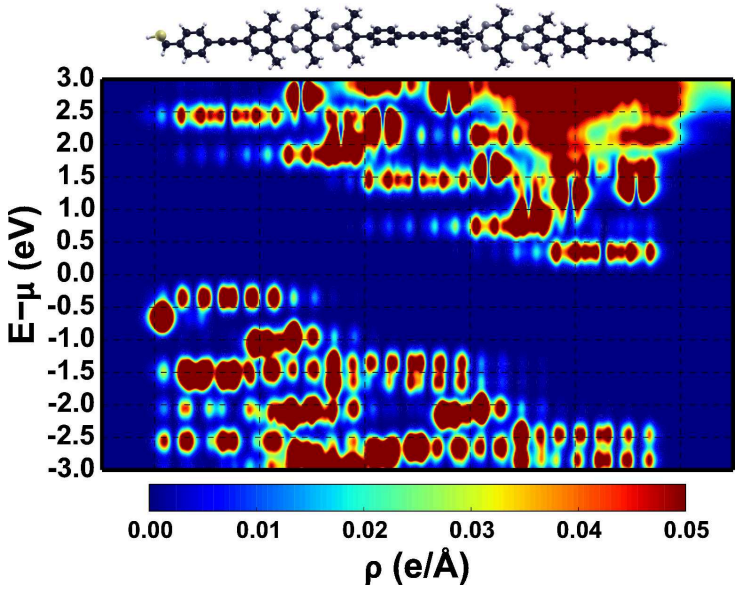

(c) LDOS contour map

Figure 2.5.2: Electron potential energy (a), Unit-DOS (b) and LDOS contour map (c) of the cascade in N_{down} configuration as shown in Figure 2.5.1a. The vertical lines in the Unit-DOS (b) indicate the energy intervals containing two states. The numbering and coloring of the units follows the color code in the sketch of the chemical structure in Figure 2.5.1. The structure above the LDOS map (c) indicates the position of the molecules in the monolayer.

the energy axis of the LDOS map is aligned to the chemical potential, the energy values given for certain states are relative to this chemical potential. The LDOS map shows that a thiol-state occurs at an energy of about −0.7 eV. At about −1.0 eV two states show up that seem to be the same as two states at about −2.0 eV, only that the first two states are localized at the first pyrimidine-ring of unit #2 and on the phenyl-ring with the side-chains of unit #1, while the latter two states are localized on the corresponding pyrimidine- and phenyl-ring of the units #3 and #4. In Figure 2.5.3 the iso-density plots of the thiol-state and the states at about −1.0 eV are shown. From sub-figure (b) it gets clear that the pyrimidine-state is a σ-state while the state on the phenyl-ring is a π-state.

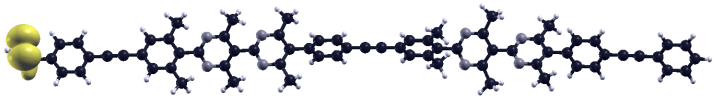

(a) Thiol state

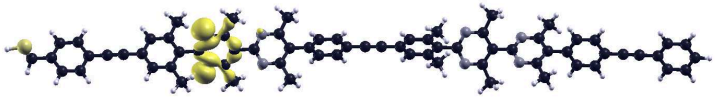

(b) Pyrimidine σ-state

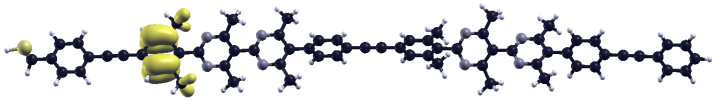

(c) Phenyl state

Figure 2.5.3: iso-density plots of some selected states below the chemical potential of the cascade monolayer in N_{down} configuration. The state in (a) has the highest energy and the state in (c) the lowest.

The states at about −2.0 eV have the same shape as the states at about −1.0 eV and are just localized on different units. Therefore they are not shown here.

2.5.1.2 N_{up}

For the cascade structure in N_{up} configuration the dipole moments point towards the substrate-side. The electron potential energy (a), the Unit-DOS (b) and the LDOS (c) for this structure are displayed in Figure 2.5.4. The vertical lines in the Unit-DOS plot indicate the energy intervals containing two states. The change in vacuum energy ΔE_{vac} is about 2.88 eV as can be seen from the electron potential energy and therefore almost double as high as for the basic N_{up} monolayer. A comparison of the magnitude of this change with the one for the cascade in N_{down} configuration reveals that it is significantly larger. Slight differences in the geometries in matters of twist angles between the two cascade structures could be a reason for a higher dipole moment in the N_{up} system. A direct consequence of this stronger dipole moment is a almost complete closure of the gap, as can be determined from the Unit-DOS and the LDOS. These two plots also reveal the fact that the molecular HOMO is localized on the vacuum-side unit (#5) and the molecular LUMO is localized on the substrate-side unit (#1). Like for the N_{down} cascade, the two plots show the stair-like electronic structure and the Fermi-level pinning behavior of HOMO and LUMO. Besides the lower gap, the two cascades have a very similar electronic structure. Therefore, similar states as displayed in Figure 2.5.3 for the N_{down} cascade can also be found in this structure. The σ-states of the pyrimidines lie at energies of circa −0.7 eV and −2.0 eV relative to the chemical potential and just below them are the π-states of the phenyl rings with the side-chains.

The energetic shift between the highest occupied states of the central unit (#3) and the substrate-side unit (#1) is approximately +1.41 eV, the shift between the highest occupied

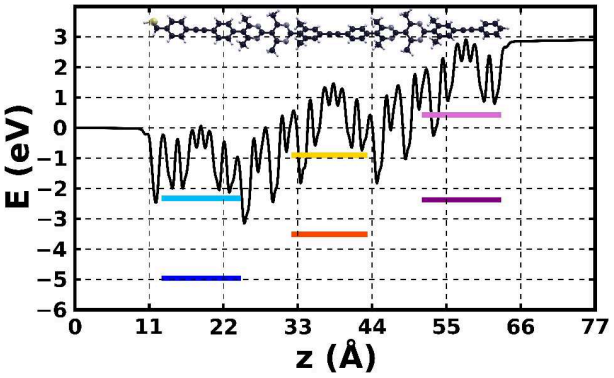

(a) Electron potential energy

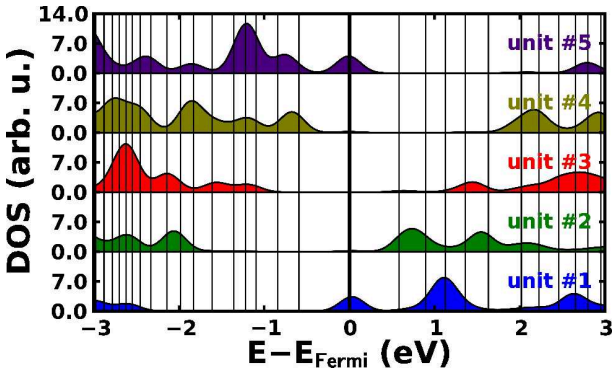

(b) Unit-DOS

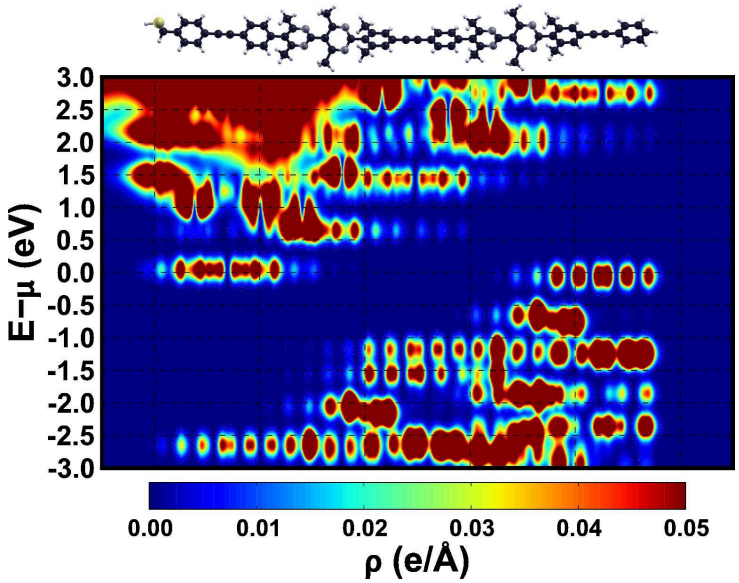

(c) LDOS

Figure 2.5.4: Electron potential energy (a), Unit-DOS (b) and LDOS contour map (c) of the cascade in N_{up} configuration. The vertical lines in the Unit-DOS (b) indicate the energy intervals containing two states. The numbering and coloring of the units follows the color code in the sketch of the chemical structure in Figure 2.5.1. The structure above the LDOS map (c) indicates the position of the molecules in the monolayer.

orbitals of the vacuum-side unit (#5) and the central unit (#3) is about +1.21 eV. This two shifts add up to a total shift between the vacuum-side unit and the substrate-side unit of about +2.62 eV, a value close to ΔE_{vac}.

2.5.2 Quantum-wells

The combination of two dipole layers with dipole moments pointing in different directions leads to quantum-well like structures. In this work, as for the cascade structures, the two dipole layers are separated by a backbone unit. The chemical structures of the quantum-wells are depicted in Figure 2.5.5. The colors indicate the segmentation into different

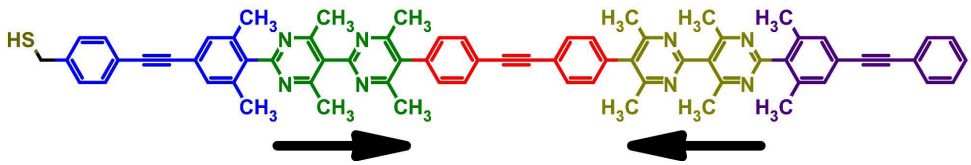

(a) *Electron quantum-well*

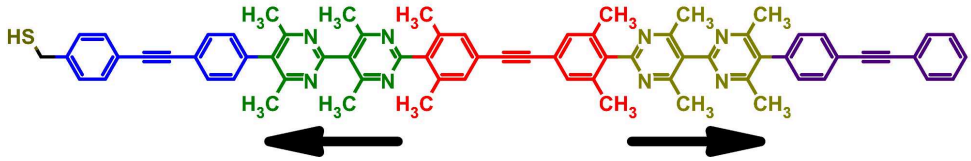

(b) *Hole quantum-well*

Figure 2.5.5: Chemical structures of the quantum-wells, the colors indicate the segmentation into different units and the arrows indicate the directions of the dipole moments.

units and the small arrows show the directions of the dipole moments. When the dipole moments point towards each other, one gets a structure which is acting as a quantum-well for electrons (Figure 2.5.5a). Two dipole moments pointing away from each other lead to a quantum-well structures for holes. Therefore, the structures will be referred to as *electron quantum-well* and as *hole quantum-well*.

The two quantum-well structures have some common properties. For one, since the dipole moments almost cancel because they point into different directions, both structures show virtually no change in the vacuum energy. The second common feature is that the orbitals on the substrate-side and on the vacuum-side are energetically very similar while the orbitals in the middle get shifted either up or down in energy. The global gap gets reduced in both cases, but in contrast to the cascade structures it is far from closed.

2.5.2.1 Electron QW

The dipole moments in the electron quantum-well structure point towards each other, therefore shifting the orbitals in the middle downwards in energy. This situation gets very clear when looking at the Unit-DOS (b) or the LDOS (c) Figure 2.5.6. From this two plot its also evident that the molecular HOMO is localized on the substrate-side and the vacuum-side units (#1 & #5). The molecular LUMO is localized on the central unit (#3) and has a little intensity on the neighboring pyrimidine rings. The LDOS reveals that the electronic structure of the electron quantum-well is very symmetric with the exception of the thiol-peak at about $-1.1\,\mathrm{eV}$. The existence of this symmetry is actually not that surprising if one takes into account that the geometries of the quantum-well structures are quite symmetric themselves except for the methyl-thiol-group and some minor differences in the twist angles. Therefore, one can expect the electronic structure of the hole quantum-well to be symmetric as well. The symmetry of the electron quantum-well manifests itself also in the energies of the orbitals of the substrate-side and the vacuum-side units. For the highest occupied state on the substrate-side unit the energy is about $-4.24\,\mathrm{eV}$ and for the corresponding state on the vacuum-side unit it is circa $-4.27\,\mathrm{eV}$. So the difference

between those two energies is practically zero. The energy of the highest occupied state on the central unit is approximately −5.48 eV. The energy difference between the highest occupied orbitals of the middle and outer units is, therefore, in the range of 1.21 eV to 1.24 eV.

The σ-peaks of the pyrimidine rings occur at about −1.3 eV relative to the chemical potential and the π-states of phenyl-rings with the side chains lie just below them. This states have the same shape as in the cascade system contained in Figure 2.5.3.

A look at the electron potential energy in Figure 2.5.6a reveals that the change in vacuum energy is indeed virtually zero, as expected. The potential energy is lower in the middle than in the outer segments.

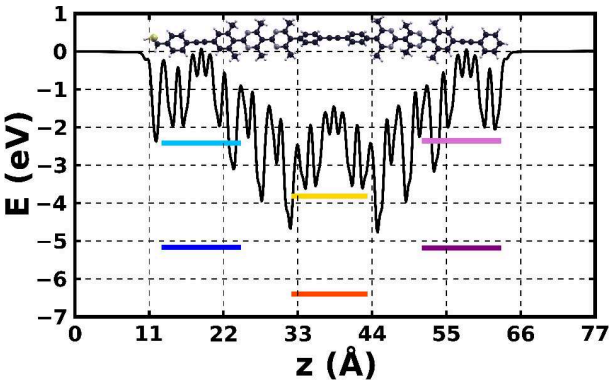

(a) Electron potential energy

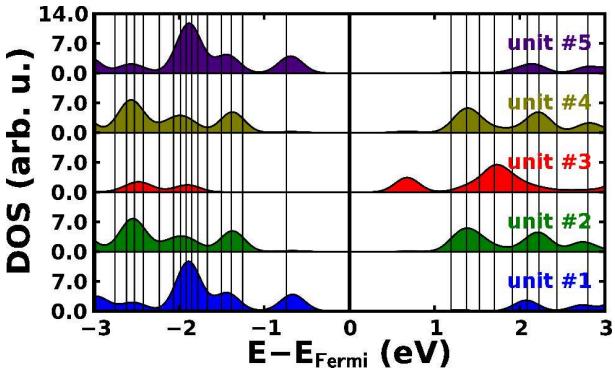

(b) Unit-DOS

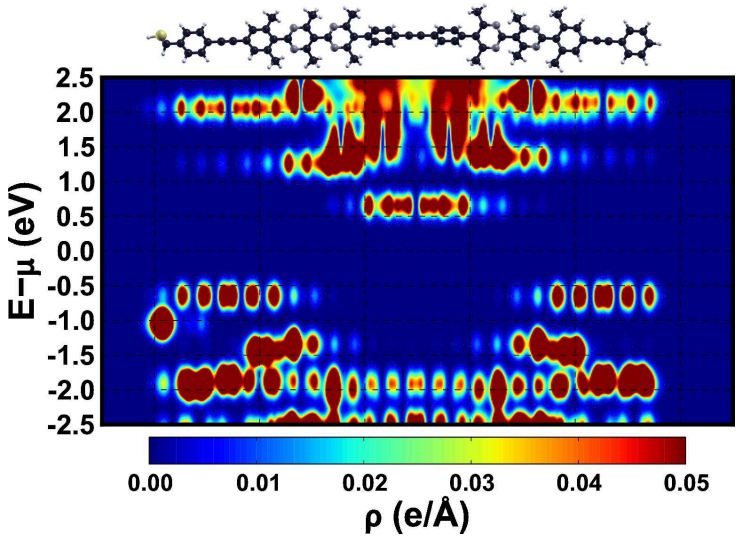

(c) LDOS

Figure 2.5.6: Electron potential energy (a), Unit-DOS (b) and LDOS contour map (c) of the electron quantum-well. The vertical lines in the Unit-DOS (b) indicate the energy intervals containing two states. The numbering and coloring of the units follows the color code in the sketch of the chemical structure in Figure 2.5.5. The structure above the LDOS map (c) indicates the position of the molecules in the monolayer.

2.5.2.2 Hole QW

From the electron potential energy displayed in Figure 2.5.7a it is evident that the hole quantum-well structure also does not produce any significant shift in the vacuum energy. The potential energy is higher in the middle than in the outer regions. A look at the Unit-DOS (b) and the LDOS (c) confirms the quantum-well like structure. Due to the dipole moments pointing away from each other, the orbitals of the central unit (#3) gets shifted up in energy compared to the orbitals of the substrate-side and vacuum-side units (#1 & #5). Thus, the molecular HOMO is localized on the central unit while the molecular LUMO is localized on the substrate-side and the vacuum-side units. In the hole quantum-well structure, the energies of the highest occupied states on the substrate-side and the

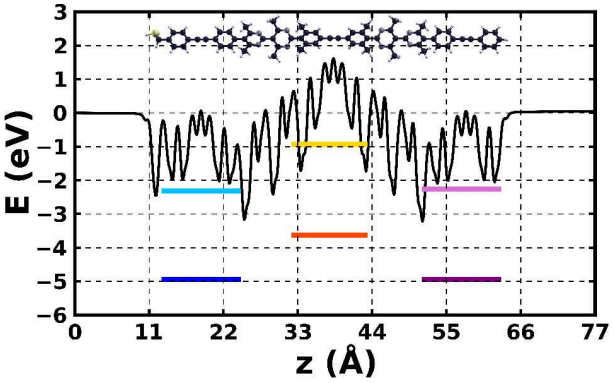

(a) Electron potential energy

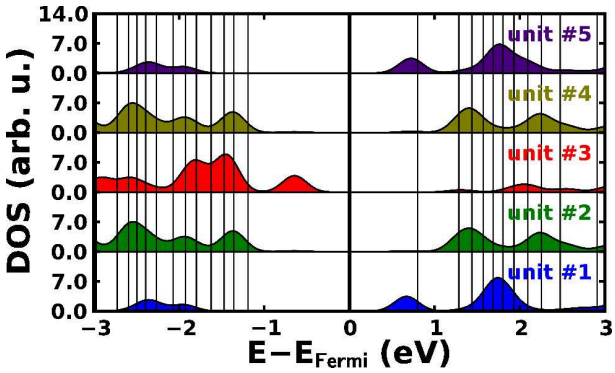

(b) Unit-DOS

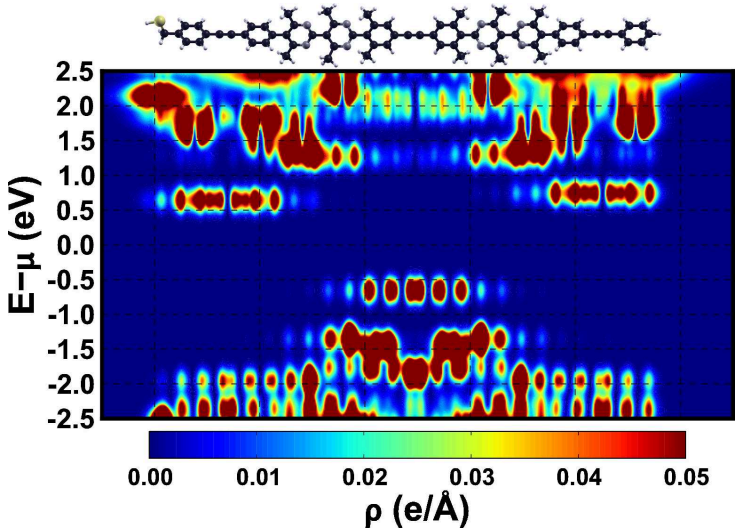

(c) LDOS

Figure 2.5.7: Electron potential energy (a), Unit-DOS (b) and LDOS contour map (c) of the hole quantum-well. The vertical lines in the Unit-DOS (b) indicate the energy intervals containing two states. The numbering and coloring of the units follows the color code in the sketch of the chemical structure in Figure 2.5.5. The structure above the LDOS map (c) indicates the position of the molecules in the monolayer.

vacuum-side units posses the same energy, namely approximately −4.59 eV. The highest occupied state on the central unit is shifted by 1.33 eV compared to the substrate-side and vacuum-side units and, hence, possesses an energy of circa −3.26 eV.

The LDOS map shows that the electronic structure of the hole quantum-well possess also a symmetry similar to the one of the electron quantum-well. According to the LDOS there are two asymmetric states this time. Here, the energies of the states are given relative to the chemical potential. For one there is the well-known thiol-state at an energy of circa −2.5 eV. The other state is an unoccupied methyl-thiol state at an energy of about +2.2 eV. The familiar σ-states of the pyrimidine rings have an energy of approximately −1.3 eV. Just below this states lie the well-known π-states of the phenyl-rings with the side chains.

Chapter 3

Influence of Backbone and Shifting Units

In this chapter, properties of molecules with different backbones (section 3.1) and shifting units (section 3.2) will be investigated and compared to each other. The shifting unit for the backbone comparison will be bipyrimidine since it can be used in a planar as well as in a twisted configuration. The Tour-wire based molecule with 6 methyl substituents, which has been used in chapter 2 to guide the path from a molecule to a quantum-well, will serve as reference system for this task.This choice will be justified through a comparison with the Tour-wire based molecules with 8 and without methyl substituents in section 3.1. In subsection 3.1.2, the biphenyl-, bithiophene- and butadiyne-based backbones will be discussed. To conclude this part of the chapter, a summary of the comparisons of the backbones will be given in subsection 3.1.3. The second part of this chapter will examine the effects of two different shifting units (section 3.2). For this purpose a biphenyl-based backbone will be used.

3.1 Different Backbones

The backbone units that are used for this comparison are shown in Figure 3.1.1 (and also in Figure 1.4.3 in section 1.4). The reference system will be the monolayer with Tour-wire based backbone unit. 6 methyl substituents will be attached to this monolayer, two at each pyrimidine ring and two to the Tour-wire based backbone unit on the side of the nitrogen atoms of the pyrimidine. The other backbones are Tour-wire based molecules

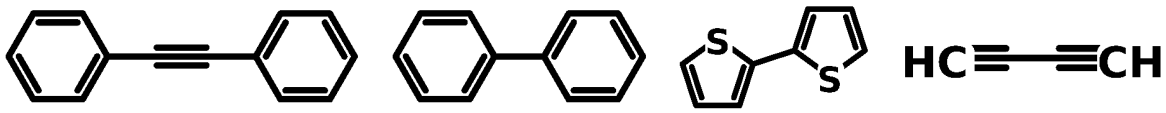

(a) Tour-wire based backbone *(b) Biphenyl* *(c) Bithiophen* *(d) Butadiyne*

Figure 3.1.1: Chemical structures of backbone units

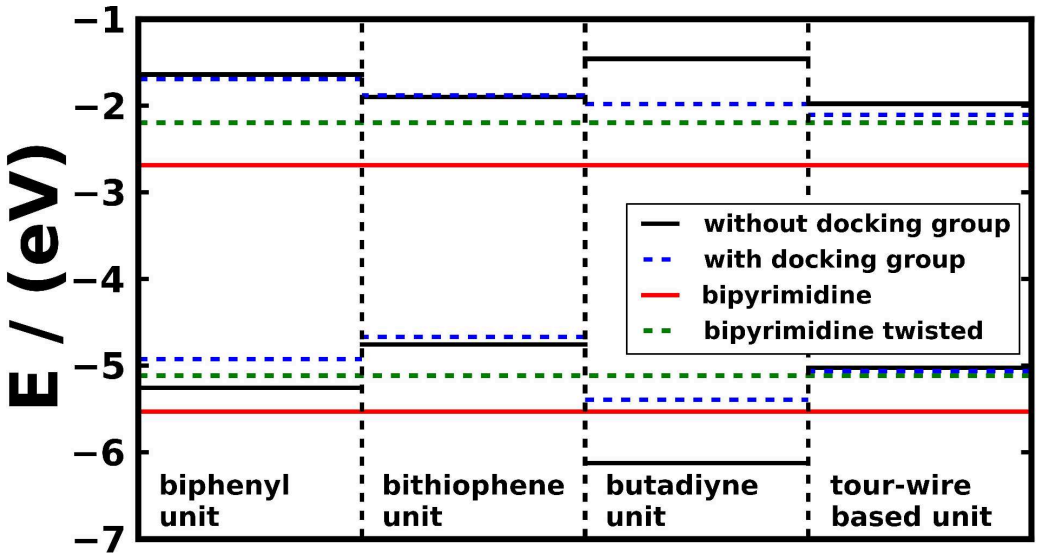

Figure 3.1.2: HOMOs (all lines below −4 eV) and LUMOs (all lines above −3 eV) of the backbone units with (dashed blue lines) and without (black solid lines) docking groups attached. The red lines indicate the HOMO and LUMO energies of the planar bipyrimidine shifting unit and the green dashed lines indicate the HOMO and LUMO energies of the twisted bipyrimidine shifting unit with methyl substituents attached. All energies were calculated with Gaussian03[42] using the PBE[43] functional and the 6-31G basis set.*

with 8 and without methyl substituents as well as biphenyl, bithiophene and butadiyne. Except for the butadiyne backbone, a methyl spacer was put in between the backbone and the thiol docking group. The Tour-wire based monolayers were always put in a $2 * \sqrt{3} \times 3$ unit cell due to geometrical reasons. The other systems were also simulated using this unit cell for the sake of comparison. Also free-standing monolayers and SAMs on metal substrate were investigated.

The different backbone units have very different properties in gas phase. This can be seen in Figure 3.1.2, where the HOMO and LUMO energies of the backbone units with and without docking groups are shown. They are compared to the respective energies of the bipyrimidine unit. One can see from this plot that the energetic change of the frontier orbitals induced due to the attachment of the docking group is rather small for most backbone units. Only for the butadiyne the orbitals are shifted more strongly. This might be due to the fact that in the butadiyne backbone unit no methyl spacer was used. Therefore, the eigenvalues of this backbone unit are shifted up due to the influence of the thiol group.. One can also see the effect of attaching methyl substituents to the bipyrimidine. While the unsubstituted bipyrimidine is planar and has a low lying LUMO, the substitution leads to a twist of the pyrimidine rings relative to each other and to higher HOMO and LUMO energies compared to the unsubstituted bipyrimidine.

The properties, especially the localization of states in the monolayers composed of these molecules cannot necessarily be deduced from the properties of the components in gas phase. Still, knowing them will help in the interpretation of the results.

3.1.1 Tour-wire based Backbones

The chemical structures for the Tour-wire based molecules with 6 and without methyl substituents have already been shown in Figure 2.0.1 and Figure 2.2.1. The one for the molecule with 8 methyl substituents is shown in Figure 3.1.3.

Table 3.1 lists results of the calculations of the systems with Tour-wire based backbone units. The second and third column show results belonging to the free-standing monolayers of the systems, namely the changes in the vacuum energies ΔE_{vac} and the energy shifts of the highest occupied orbitals E_{shift}^{ML}. The last two columns list the work-function modifications $\Delta\phi$ and the energy shifts of the highest occupied orbitals E_{shift}^{SAM} for the different SAMs on metal. The energy shifts of the highest occupied orbitals were calculated according to equation 1.6.4. From this table, one can see that the magnitude of the change of the vacuum energy for the monolayer with 6 methyl substituents is higher than for the monolayers with 8 and without methyl substituents. For the monolayer with 6 methyl substituents, the magnitude of ΔE_{vac} is the same for both configurations, N_{down} and N_{up}. The same is true for the monolayer with 8 methyl substituents but not for the one without methyl substituents. For the latter, the N_{up} configuration has a higher magnitude of ΔE_{vac} than the N_{down} configuration. Like the change in the vacuum energy, the energy shifts between the highest occupied orbitals of the vacuum-side unit and the substrate-side unit (E_{shift}^{ML}) have the highest magnitudes in the free-standing monolayers with 6 methyl substituents. The magnitudes of these shifts are only about half as high

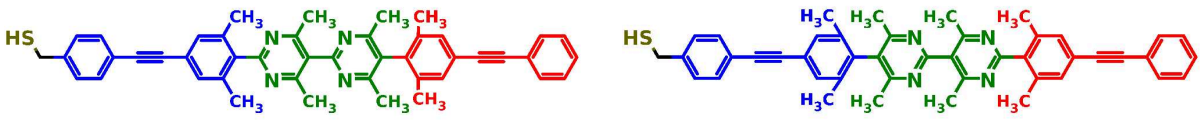

(a) N_{down} *(b) N_{up}*

Figure 3.1.3: Chemical structure of the Tour-wire based molecule with 8 side-chains

Table 3.1: Changes in the vacuum energies ΔE_{vac}, energy shifts of the highest occupied orbitals for the free-standing monolayers E_{shift}^{ML} , work-function modifications $\Delta\phi$ and energy shifts of the highest occupied orbitals for the SAMs on metal E_{shift}^{SAM} for the different Tour-wire-based backbones. For the calculation of the energy shifts of the highest occupied orbitals see equation 1.6.4. The chemical structures of the systems are shown in Figure 2.0.1, Figure 2.2.1 and Figure 3.1.3.

System	ΔE_{vac} / eV	E_{shift}^{ML} / eV	$\Delta\phi$ / eV	E_{shift}^{SAM} / eV
6 methyl substituents, N_{down}	-1.50	-1.32	-2.71	-1.58
6 methyl substituents, N_{up}	+1.51	+1.30	-0.17	+0.78
8 methyl substituents, N_{down}	-1.30	-1.17	-2.52	-1.40
8 methyl substituents, N_{up}	+1.33	+1.13	-0.13	+0.74
no methyl substituents, N_{down}	-0.76	-0.75	-1.31	-0.74
no methyl substituents, N_{up}	+0.91	+0.69	-0.17	+0.44

in the planar free-standing monolayers without methyl substituents. In the monolayers with 8 methyl substituents, the magnitudes of the shifts are only a few tenths of an eV lower compared to the reference monolayers. For the systems in N_{down} configuration, the work-function modification $\Delta\varphi$ of the SAM with 6 methyl substituents has the highest magnitude. Compared to this reference SAM, the magnitude of the work-function modification of the system with 8 methyl substituents is only 0.19 eV lower. The magnitude of $\Delta\varphi$ for these two systems is about twice as high as for the planar system without methyl substituents. For the SAMs in N_{up} configuration, the work-function modifications have virtually the same value for all three systems. The reason for this is Fermi-level pinning, as discussed in subsubsection 2.4.1.1 for the reference SAM. In Figure 3.1.4 the Unit-DOS plots of the SAMs with Tour-wire based backbones on metal are shown for both configurations. From these plots, one can see that in N_{down} configuration only the SAM with 6 methyl substituents exhibits Fermi-level pinning of the LUMO. In contrast, all three systems exhibit Fermi-level pinning of the HOMO when calculated in N_{up} configuration. The magnitudes of the shifts of the highest occupied orbitals between the vacuum-side and the substrate-side units are much lower in the SAMs in N_{up} configuration than in the systems in N_{down} configuration. This is also a direct consequence of the Fermi-level pinning. Due to the Fermi-level pinning of the HOMOs of the SAMs in N_{up} configuration, local charge rearrangements on the vacuum-side unit induce a dipole moment counteracting the dipole moment of the bipyrimidine and, thus, preventing the HOMO from getting shifted up further. The localization for the HOMOs and LUMOs of the SAMs on metal can be determined from these Unit-DOS plots. For the SAMs with methyl substituents, the localization is almost equally well for both configurations. The LUMOs of the planar SAMs extend onto the shifting units for both configurations, thus, leading to a worse localization compared to the twisted SAMs. In N_{up} configuration, in the planar SAM the HOMO also extends onto the bipyrimidine unit.

On the following pages (66-68), the LDOS contour maps of the free-standing monolayers with 6 (N_{down}: Figure 3.1.5, N_{up}: Figure 3.1.8), 8 (N_{down}: Figure 3.1.6, N_{up}: Figure 3.1.9) and without methyl substituents (N_{down}: Figure 3.1.7, N_{up}: Figure 3.1.10) are shown. From these plots, one can see that, for the N_{down} configuration, the HOMO is localized on the substrate-side and the LUMO is localized on the vacuum-side for the two twisted systems. For the N_{up} configuration, the LUMO is localized on the substrate-side and the HOMO on the vacuum-side. Again, this is valid for the two twisted systems. Therefore, the localization is equally good for the free-standing monolayers with 6 and 8 methyl substituents for both configurations. In the planar monolayers without methyl substituents the localization is clearly worse compared to the other two systems. The HOMO and the LUMO of the planar monolayers extend onto the shifting units. In addition to the structural effects discussed in section 2.2, this might be explained by taking a look at the energy levels of the backbone and shifting units in gas phase, as depicted in Figure 3.1.2. From this plot, one can see that the HOMO and LUMO levels of planar bipyrimidine without methyl substituents lie a few tenths of an eV below the HOMO and LUMO levels of the Tour-wire-based units. In contrast, the HOMO and LUMO energies of the twisted bipyrimidine with methyl substituents are very close to the ones of the Tour-wire-based units. The frontier orbitals of the backbone unit on the side of the nitrogen atoms of the bipyrimidine gets always shifted up in energy, while the backbone unit

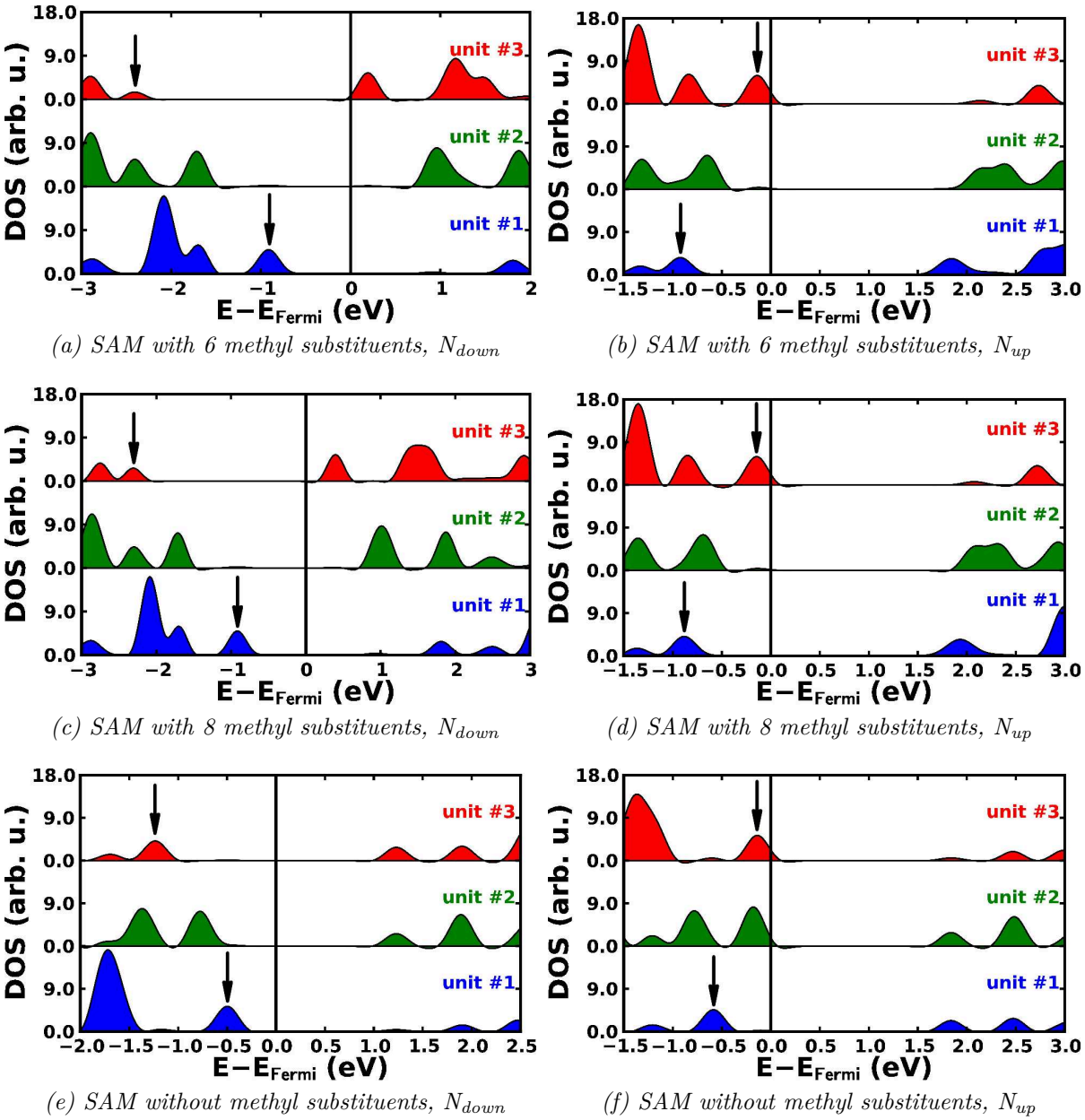

(a) SAM with 6 methyl substituents, N_{down}

(b) SAM with 6 methyl substituents, N_{up}

(c) SAM with 8 methyl substituents, N_{down}

(d) SAM with 8 methyl substituents, N_{up}

(e) SAM without methyl substituents, N_{down}

(f) SAM without methyl substituents, N_{up}

Figure 3.1.4: Unit-DOS plots of the SAMs with Tour-wire based backbone on metal in N_{down} and N_{up} configuration. The arrows indicate the peaks used to calculate the energy shifts of the highest occupied orbitals. The chemical structures of the molecules are shown in Figure 2.0.1, Figure 2.2.1 and Figure 3.1.3.

on the other side of the bipyrimidine unit always gets shifted down. Thus, in the planar monolayers the energies of the frontier orbitals of one backbone unit are always shifted towards the HOMO and LUMO energies of the planar bipyrimidine unit. In contrast, in the twisted monolayers the frontier orbitals of both units get shifted away from the frontier orbitals of the twisted bipyrimidine unit. Therefore, the localization in the twisted monolayers is improved over the localization in the planar systems.

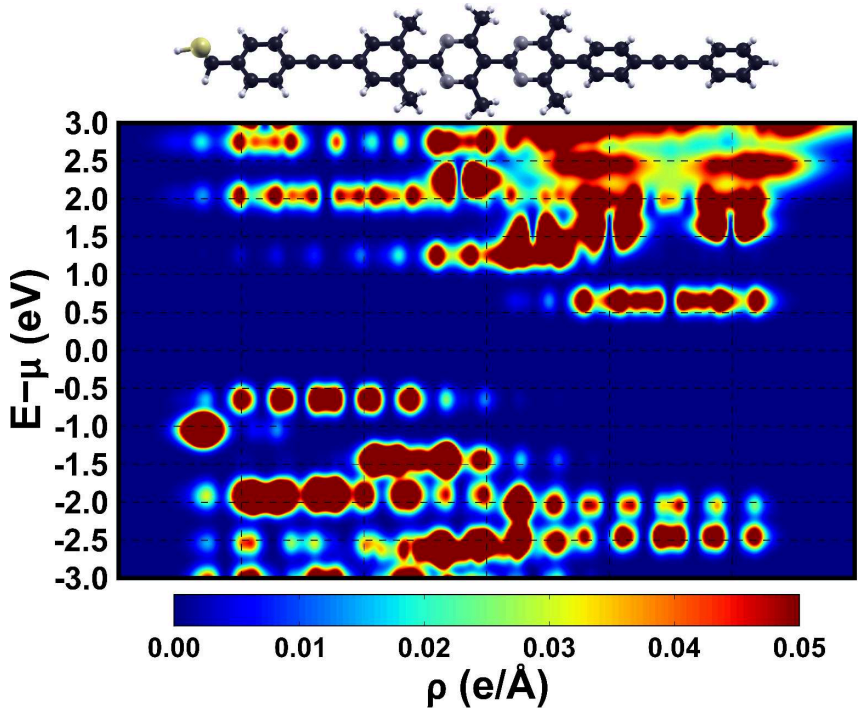

Figure 3.1.5: LDOS contour map of the free-standing monolayer with Tour-wire backbone and 6 methyl substituents in N_{down} configuration. The structure above the LDOS map indicates the position of the molecule in the monolayer.

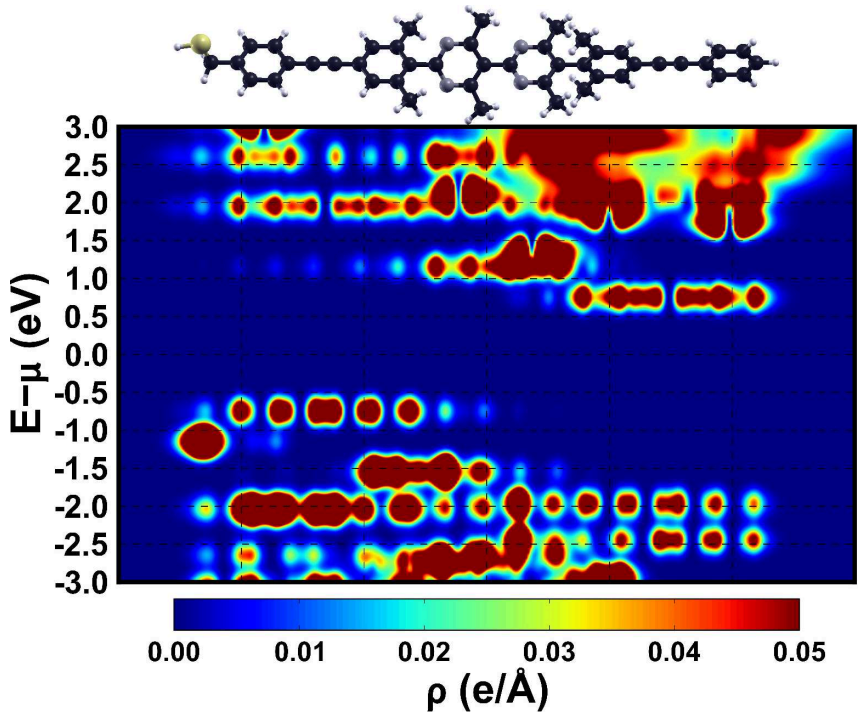

Figure 3.1.6: LDOS contour map of the free-standing monolayer with Tour-wire backbone and 8 methyl substituents in N_{down} configuration. The structure above the LDOS map indicates the position of the molecule in the monolayer.

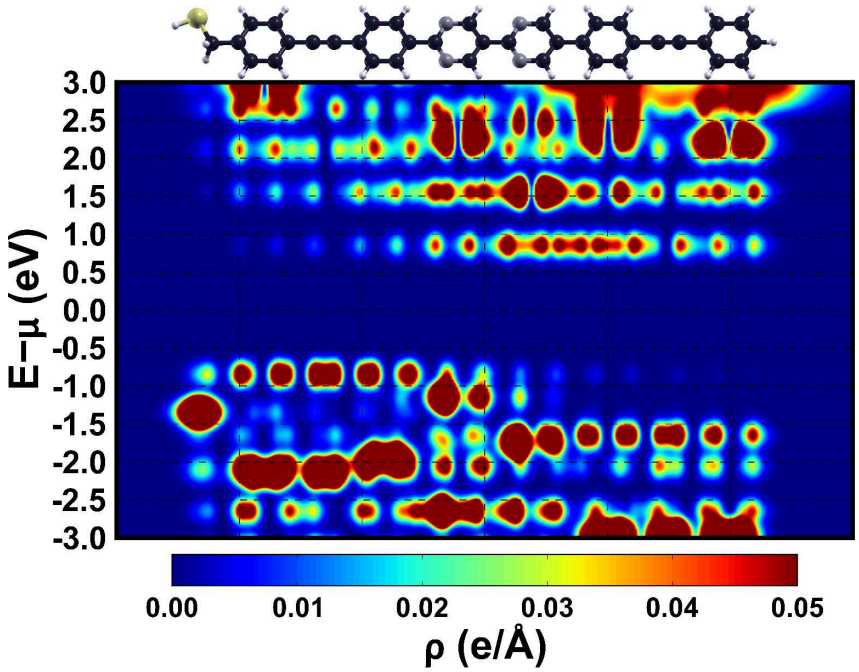

Figure 3.1.7: LDOS contour map of the free-standing monolayer with Tour-wire backbone and no methyl substituents in N_{down} configuration. The structure above the LDOS map indicates the position of the molecule in the monolayer.

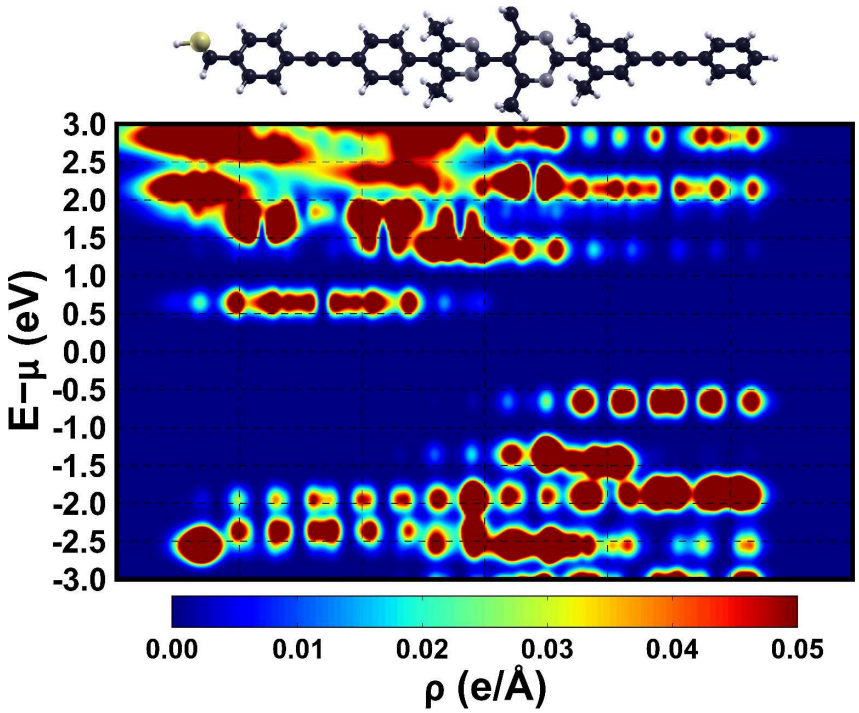

Figure 3.1.8: LDOS contour map of the free-standing monolayer with Tour-wire backbone and 6 methyl substituents in N_{up} configuration. The structure above the LDOS map indicates the position of the molecule in the monolayer.

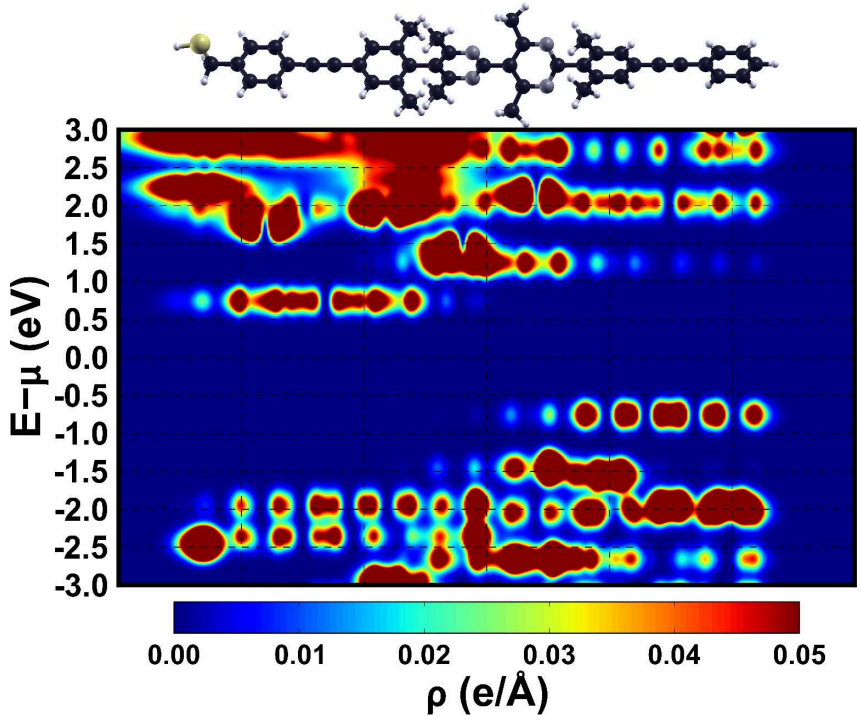

Figure 3.1.9: LDOS contour map of the free-standing monolayer with Tour-wire backbone and 8 methyl substituents in N_{up} configuration. The structure above the LDOS map indicates the position of the molecule in the monolayer.

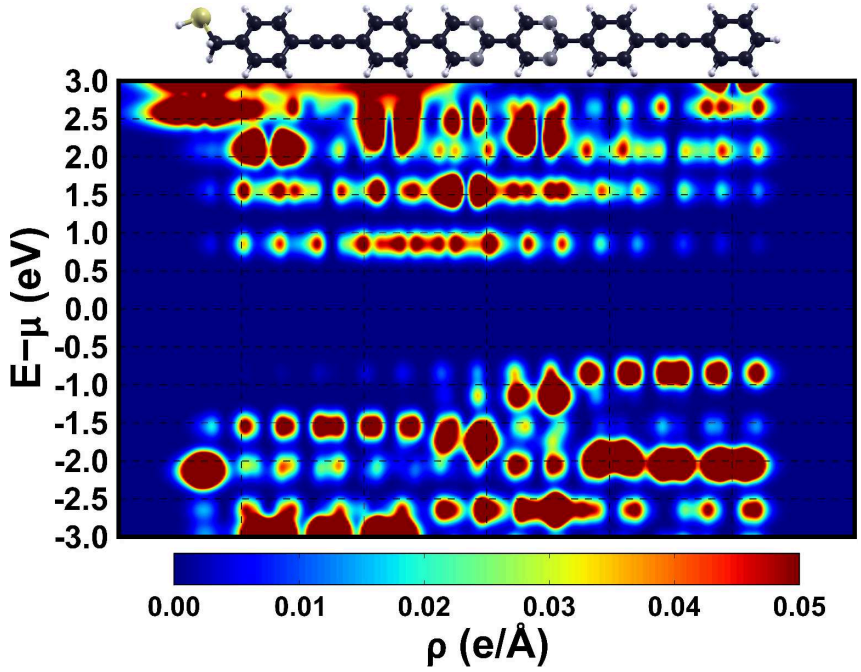

Figure 3.1.10: LDOS contour map of the free-standing monolayer with Tour-wire backbone and no methyl substituents in N_{up} configuration. The structure above the LDOS map indicates the position of the molecule in the monolayer.

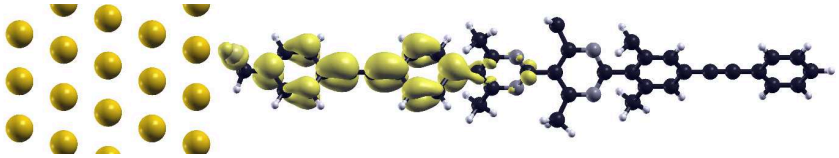

(a) LUMO, 6 side-chains

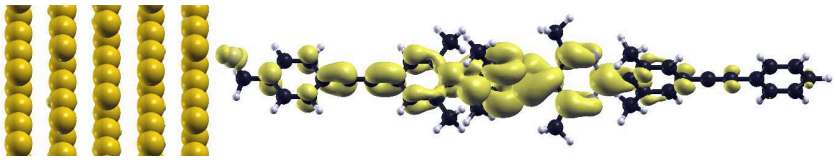

(b) LUMO, 8 side-chains

Figure 3.1.11: Iso-density plots of the LUMOs of the SAMs with 6 (a) and 8 methyl substituents (b) in N_{up} configuration.

The reason for picking the system with 6 methyl substituents as reference system rather than the one with 8 methyl substituents is shown in Figure 3.1.11. This figure shows iso-density plots for the LUMOs of the SAMs on metal substrate with 6 and 8 methyl substituents in N_{up} configuration. From these plots it is evident, that the localization of the LUMO is better in the SAM with 6 methyl substituents than in the one with 8 methyl substituents.

3.1.2 Biphenyl-, Bithiophene- and Butadiyne-based Backbones

Figure 3.1.12 shows the chemical structures of the molecules with biphenyl-, bithiophene- and butadiyne-based backbones in N_{down} configuration. All three of these molecules are completely planar and fully conjugated. In the case of the molecule with biphenyl backbone, the planarity is an artifact of the geometry optimization of the molecule in gas phase. Because of the fully conjugated character of these molecules, the localization is expected to be worse compared to the reference system with Tour-wire-based backbone and 6 methyl substituents. The bonding angle of a thiophene ring is lower than 180°, therefore, the molecule with the bithiophene backbone is slightly curved along the long molecular axis. As a result of this slight curvature, the dipole layer build up by the bipyrimidine units does not stand perfectly perpendicular to the surface but is slightly tilted. The molecule with the butadiyne-based backbone is the only one calculated without a methyl spacer between the docking group and the backbone.

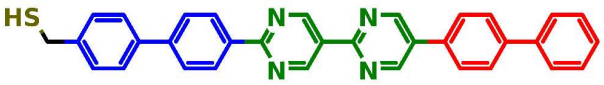

(a) Biphenyl-based backbone

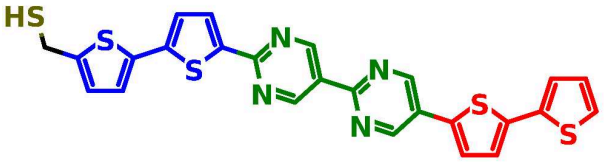

(b) Bithiophene-based backbone

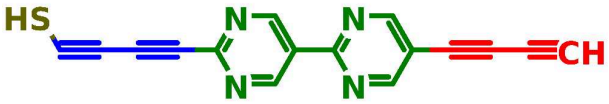

(c) Butadiyne-based backbone.

Figure 3.1.12: Chemical structures of the molecules with biphenyl-, bithiophene- and butadiyne-based backbones and bipyrimidine shifting unit in N_{down} configuration. The different colors indicate the segmentation into different units.

Table 3.2: Changes in the vacuum energies ΔE_{vac}, energy shifts of the highest occupied orbitals for the free-standing monolayers E_{shift}^{ML} , work-function modifications $\Delta\phi$ and energy shifts of the highest occupied orbitals for the SAMs on metal E_{shift}^{SAM} for the biphenyl-, bithiophene- and butadiyne-based backbones in N_{down} configuration. For the calculation of the energy shifts of the highest occupied orbitals see equation 1.6.4. The chemical structures of the systems are shown in Figure 3.1.12.

System	ΔE_{vac} / eV	E_{shift}^{ML} / eV	$\Delta\phi$ / eV	E_{shift}^{SAM} / eV
biphenyl	-0.78	-0.73	-2.41	-1.05
bithiophene	-0.35	-0.59	-1.15	-0.60
butadiyne	-0.26	-0.74	-0.78	-0.80

Table 3.2 lists results of the calculations of the systems with biphenyl, bithiophene and butadiyne backbone units in N_{down} configuration. The second and third column show results belonging to the free-standing monolayers of the systems, namely the changes in the vacuum energies ΔE_{vac} and the energy shifts of the highest occupied orbitals E_{shift}^{ML}. The last two columns list the work-function modifications $\Delta\phi$ and the energy shifts of the highest occupied orbitals E_{shift}^{SAM} for the different SAMs on metal. The energy shifts of the highest occupied orbitals were calculated according to equation 1.6.4. From this table, it is evident that the magnitude of the change in the vacuum energy ΔE_{vac} for the monolayer with biphenyl backbone is more than twice as high as for the other two monolayers. As explained above, in the monolayer with bithiophene backbone the direction of the dipole moment of the bipyrimidine is not perpendicular to the surface but

slightly tilted. Therefore, the z-component of the dipole moment is smaller. Additionally, due to its orientation, the dipole moment of the thiol group counteracts the dipole moment of the bipyrimidine, thus, resulting in a lower ΔE_{vac}. For the free-standing monolayer with butadiyne backbone, the low change in the vacuum energy is most likely caused by the thiol group. Since no methyl spacer was used in this system, attaching the thiol group causes significant differences in the electronic structures of the substrate-side and the vaccum-side backbone units. For the backbone units in gas phase, this is shown in Figure 3.1.2. In addition, Gaussian03 calculations, using the PBE functional and the 6-31G* basis set, of the molecule with butadiyne backbone with and without thiol group were carried out. The molecule without thiol group was saturated with a H atom. These calculations show that attaching the thiol group strongly reduces the magnitude of the dipole moment of the molecule. While the molecule without thiol group has a dipole moment of -3.41 Debye, it is only -1.67 Debye for the molecule with thiol group attached. Therefore, these calculations support the statement that the low change in the vaccum energy in this monolayer is caused by the influence of the thiol group due to the missing methyl spacer. An interesting behavior can be observed for the energy shifts of the highest occupied orbitals E_{shift}^{ML} in the free-standing monolayers. While the magnitude of E_{shift}^{ML} is slightly lower than ΔE_{vac} for the monolayer with biphenyl backbone, they are higher than the changes in the vacuum energies for the other two backbones. For the monolayer with the butadiyne backbone, this might be explained by taking a look at the energies of the frontier orbitals of the backbone and the shifting units in gas phase as shown in Figure 3.1.2. As explained above, due to the lack of a spacer the influence of the thiol group on the electronic structure of the backbone unit is significant. For example, in gas phase the HOMO of the butadiyne unit with the thiol group attached has an energy that is about 0.7 eV higher than the HOMO energy of the butadiyne unit without the thiol group. Thus, it is like if two different backbone units were attached to the bipyrimidine unit. Of course, the situation changes significantly when going from a single molecule to a free-standing monolayer, but as in gas phase the difference in the HOMO energies of the butadiyne with and without docking group is so significant, it probably will not vanish entirely in the case of the monolayer. Additionally, in the free-standing monolayer with butadiyne backbone and bipyrimidine as shifting unit, the highest occupied orbital on the vacuum-side unit, i.e., the backbone unit without docking group, gets shifted down in energy relative to the substrate-side unit, i.e., the backbone unit with the docking group attached. For the monolayer with bithiophene backbone, it seems that the orientation of the dipole moment of the thiol group has less influence on the orbital shift than on the change in the vacuum energy. Interestingly, the orbital shifts in the SAMs on metal assume values close to the ones in the free-standing monolayers for the systems with bithiophene and butadiyne backbone. While the SAM with biphenyl backbone is close to, but not in, the Fermi-level pinning regime, as can be seen in Figure 3.1.13, the SAM with bithiophene backbone exhibits Fermi-level pinning of the HOMO (see Figure 3.1.14). The system with butadiyne backbone does not exhibit Fermi-level pinning, but due to the lack of a spacer unit a hybridization of metal and monolayer states occurs (see Figure 3.1.15). The magnitude of the work-function modification assumes the highest value for the SAM with biphenyl backbone. In this SAM, the magnitude of$\Delta\phi$ is more than twice as high as in the two SAMs with bithiophene and butadiyne backbones.

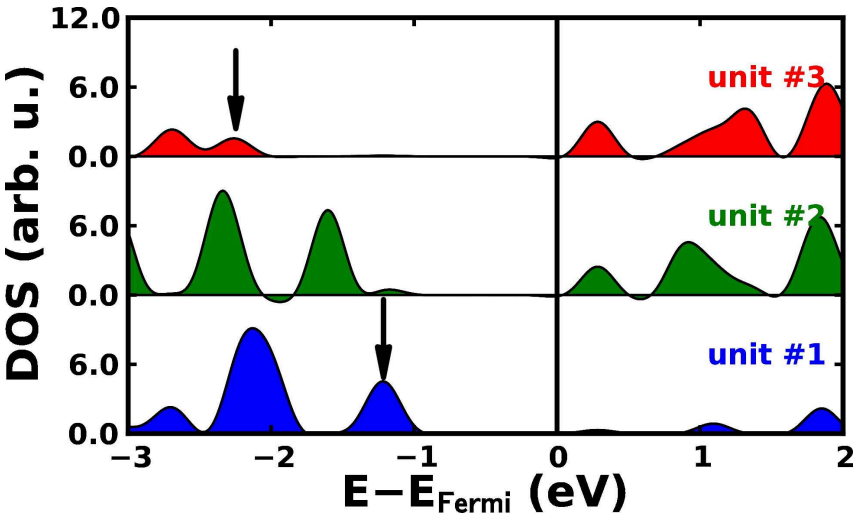

Figure 3.1.13: Unit-DOS of the SAM with biphenyl backbone. The black arrows indicate the peaks used to calculate the orbital shift of the HOMO according to equation 1.6.4.

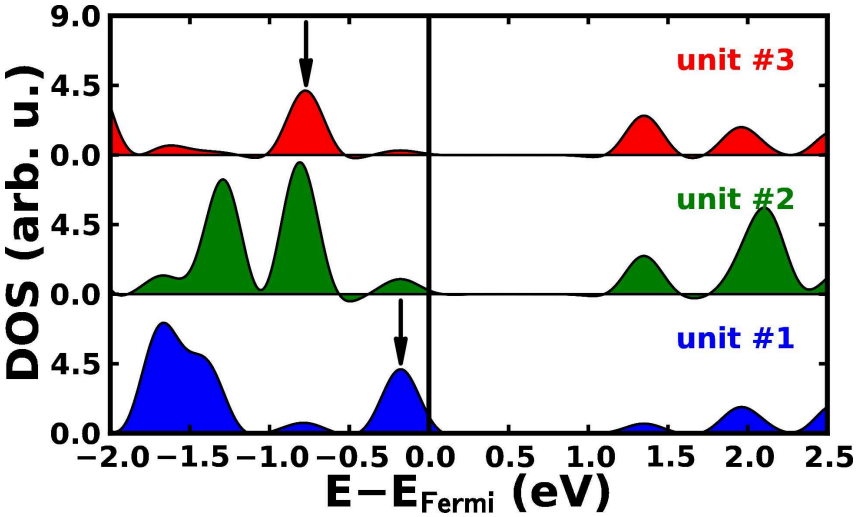

Figure 3.1.14: Unit-DOS of the SAM with bithiophene backbone. The black arrows indicate the peaks used to calculate the orbital shift of the HOMO according to equation 1.6.4.

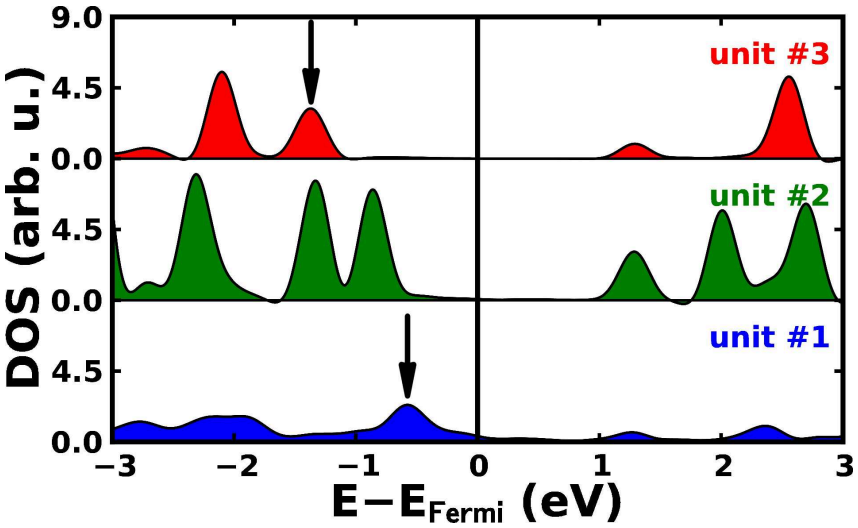

Figure 3.1.15: Unit-DOS of the SAM with butadiyne backbone. The black arrows indicate the peaks used to calculate the orbital shift of the HOMO according to equation 1.6.4.

LDOS contour maps of the free-standing monolayers in N_{down} configuration for the systems in this section are shown in Figure 3.1.16 for the monolayer with biphenyl backbone, in Figure 3.1.17 for the one with bithiophene backbone and in Figure 3.1.18 for the system with butadiyne backbone. From these plots, one can see that the localization of the LUMO is quite bad in all three monolayers. For all three backbones, the LUMO extends onto all three units. In the monolayer with the butadiyne backbone the LUMO has more density on the bipyrimidine unit than on the backbone. This could be a consequence of the low lying LUMO of the bipyrimidine (see Figure 3.1.2). The low lying LUMO of the bipyrimidine is probably also one reason for the bad localization of the LUMO in the other two monolayers. The localization of the HOMO is quite good for the monolayers with biphenyl and bithiophene backbone. In these monolayers, the HOMO is localized on the substrate-side unit and on the bipyrimidine with a very low density of states on the vacuum-side unit. In the monolayer with butadiyne backbone, the HOMO extends on all three units with the major part of DOS on the substrate-side and bipyrimidine units. For the backbones discussed in this subsection, the localization is best in the monolayer with biphenyl backbone. Using butadiyne as backbone does not deliver acceptable results in terms of localization.

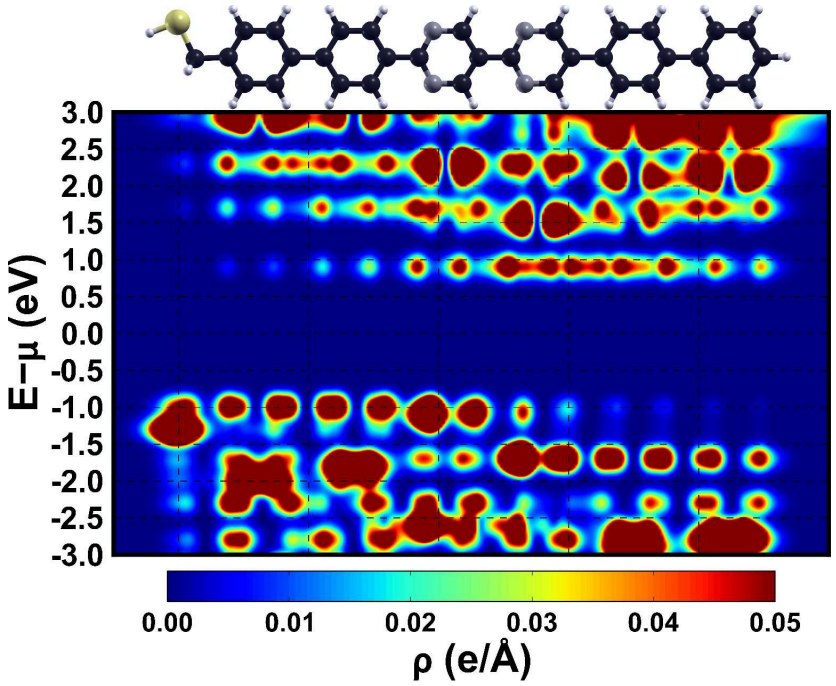

Figure 3.1.16: LDOS contour map of the free-standing monolayer with biphenyl backbone in N_{down} configuration. The structure above the LDOS map indicates the position of the molecule in the monolayer.

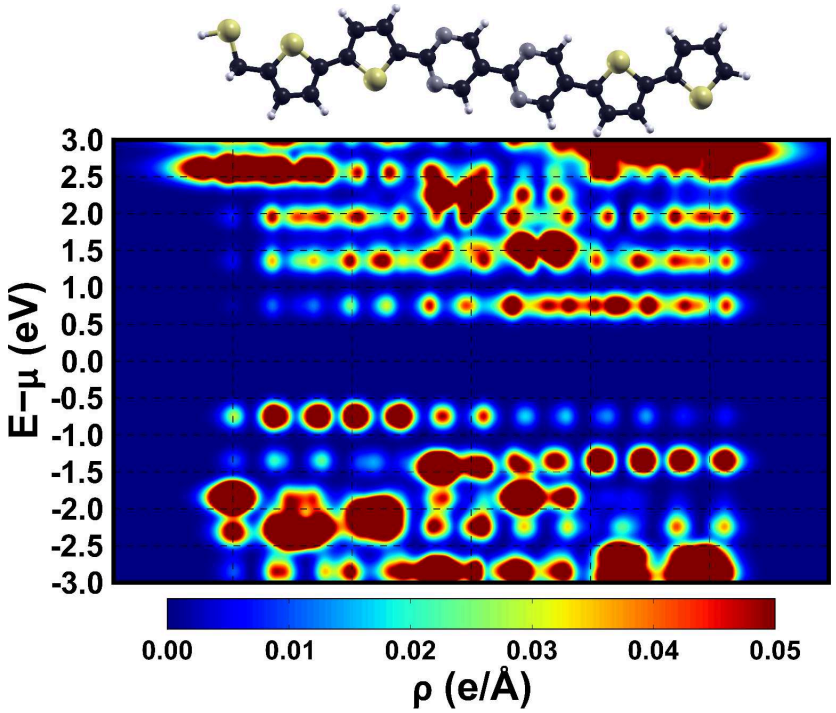

Figure 3.1.17: LDOS contour map of the free-standing monolayer with bithiophene backbone in N_{down} configuration. The structure above the LDOS map indicates the position of the molecule in the monolayer.

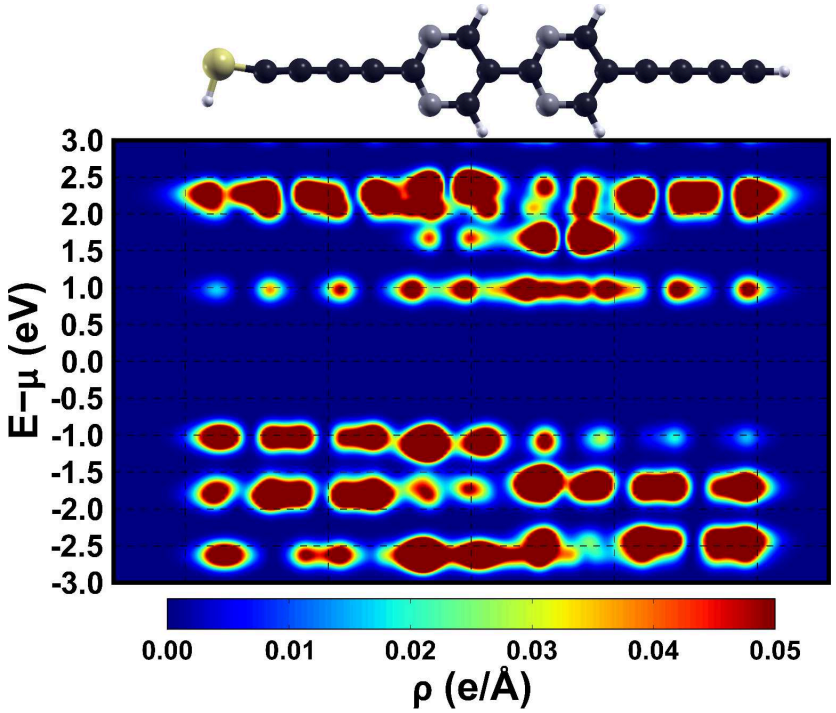

Figure 3.1.18: LDOS contour map of the free-standing monolayer with butadiyne backbone in N_{down} configuration. The structure above the LDOS map indicates the position of the molecule in the monolayer.

3.1.3 Comparison

The above sections made it pretty clear that the choice of the Tour-wire based molecule with 6 side-chains as the reference system was very good. The only other system with almost similar localization properties than the reference system was the Tour-wire based molecule with 8 side-chains. But, the molecule with 8 side-chains made some problems in the N_{up} configuration, namely the LUMO of the SAM on metal was not very well localized anymore, as can be seen in Figure 3.1.11. In general, getting a good localization of the LUMO seems difficult. Especially, for the planar systems it is almost impossible to localize the LUMO on one specific unit, in these SAMs the LUMO always extends onto at least two units. Compared to the localization of the LUMO, the confinement of the HOMO works for the most systems very well. In particular, in the systems with the biphenyl and the planar Tour-wire backbone exhibit a good localization of the HOMO. These two also appear to be the only two serious alternatives to the reference system, at least of the ones that were tested during this work, when it comes to the design of quantum-well structures. Since they are both planar they could also fit into smaller unit cells thus increasing the packing density and therefore amplifying collective effects. In the system with the bithiophene backbone the localization of the orbitals is not as good as for the Tour-wire based systems, but it would be possible to utilize this backbone for the engineering of quantum-well structures. These, as a consequence of the worse localization, would be not as distinct as for the Tour-wire based system. The butadiyne backbone on the other hand is totally useless for the purpose of the molecular engineering of quantum-well structures. The localization of the orbitals is pretty bad in this system, especially for the LUMO.

Another trend that appeared during the comparison of the systems with different backbones is that the magnitude of the change of the vacuum energy is lower for the planar monolayers compared to the twisted ones. A calculation of planar bipyrimidine in a $2\sqrt{3} \times 3$ unit cell showed that the dipole moment of the so built dipolar layer can cause a jump in the vacuum energy of 1.53 eV. The only two monolayers able of producing a jump in the vacuum energy of a similar magnitude are the twisted Tour-wire based monolayers with 6 or 8 methyl substituents respectively. All of the planar monolayers produce much smaller changes in the vacuum energy. This can explained by the fact that in the planar, fully conjugated, monolayers the electrons can spread out over the whole backbone more easily than in the twisted monolayers, in which the conjugation is broken. Therefore charge rearrangements that counteract the dipole moment of the bipyrimidine can occur with a higher intensity in the planar monolayers.

3.2 Different Shifting Units

In this work, two shifting units were compared, namely bipyrimidine and bidioxane. The first one is composed of two conjugated carbon rings with two C-H groups of every ring substituted by nitrogen atoms. The latter one is assembled from two non-conjugated carbon rings. Two C-H groups of each ring are substituted by oxygen atoms. The chemical structures and geometries of these shifting units have already been shown in

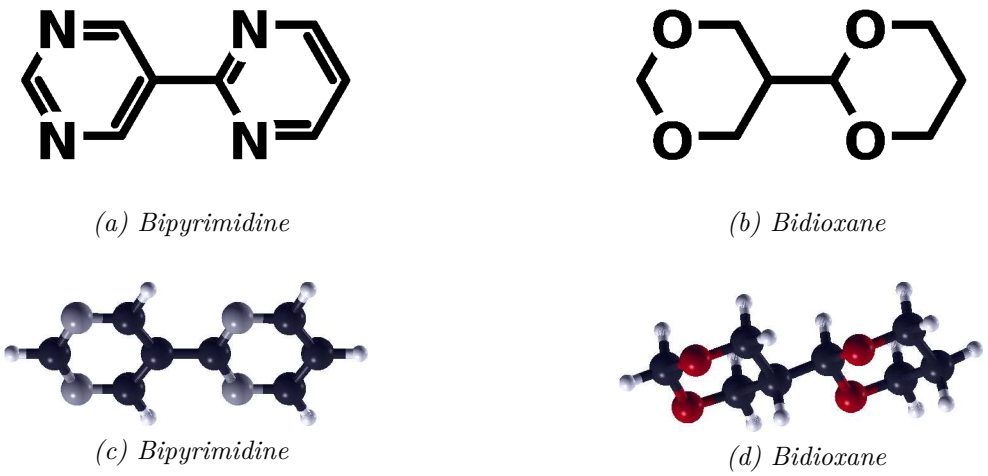

(a) Bipyrimidine *(b) Bidioxane*

(c) Bipyrimidine *(d) Bidioxane*

Figure 3.2.1: Chemical structures (a,b) and geometries (c,d) of the dipolar units.

Figure 3.2.1 (as well as in Figure 1.4.2 in section 1.4). The dipole moments of the two shifting units along the long molecular axis, bipyrimidine and bidioxane, were determined by Gaussian03[42] calculations using the PBE[43] functional and the 6-31G* basis set to be 4.41 Debye and 3.02 Debye, respectively. The HOMO and LUMO energies of the bipyrimidine and the bidioxane units obtained from these Gaussian03[42] calculations are shown in Figure 3.2.2. Additionally, the HOMO and LUMO energies of the biphenyl backbone unit are indicated in this plot. One can clearly see that the HOMO energies for

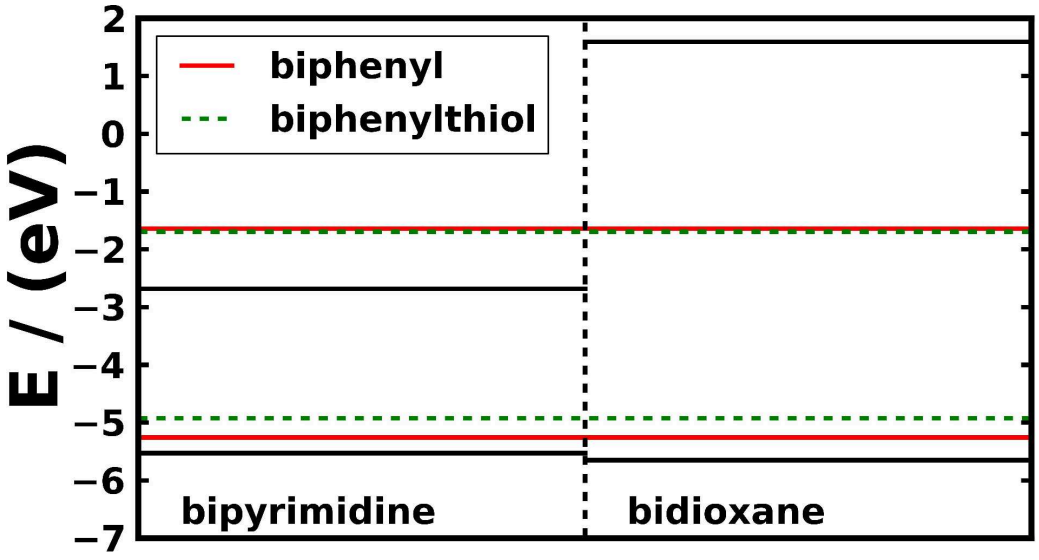

Figure 3.2.2: HOMO (solid lines) and LUMO (dashed lines) energies of the dipolar units bipyrimidine (blue) and bidioxane (green) as well as of the biphenyl backbone unit (red). These energies were obtained through Gaussian03[42] calculations using the PBE[43] functional and the 6-31G basis set.*

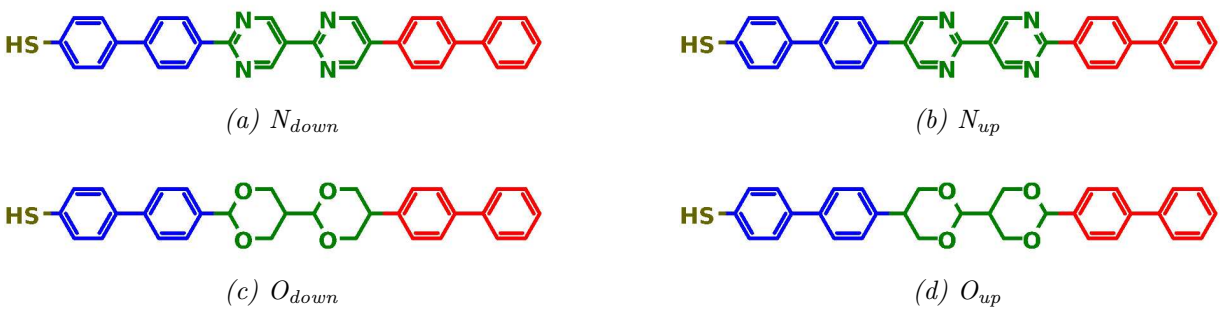

(a) N_{down} *(b)* N_{up}

(c) O_{down} *(d)* O_{up}

Figure 3.2.3: Chemical structures of the molecules with different shifting units and a biphenyl backbone

the two dipolar units in gas phase are very similar and lie slightly below the HOMO energy of the biphenyl backbone. On the other hand, the LUMO energies of the two shifting units are very different. In contrast to the bidioxane, which has a very high energy gap and, therefore, a very high LUMO energy, the bipyrimidine has a quite low lying LUMO. Somewhere in between those two LUMOs, but closer to the one of the bipyrimidine, lies the LUMO of the biphenyl backbone unit.

The potential changes in the vacuum energies produced by those two shifting units in a $2\sqrt{3} \times 3$ unit cell were determined to be about 1.53 eV for the bipyrimidine and approximately 1.20 eV for the bidioxane.

For the comparison of the different shifting units they have been built into molecules with a biphenyl backbone. The chemical structures of these molecules are shown in Figure 3.2.3. The geometries of the molecules were optimized using Gaussan03 with the PBE[43] functional and the 6-31G* basis set. The molecules with bipyrimidine as shifting unit stayed planar during the optimization procedure. This is clearly an artifact of the calculation. On the other hand, in close packed monolayer oligophenylen is almost planar.

Table 3.3 lists the changes in the vacuum energies, ΔE_{vac}, the energy shifts of the highest occupied orbitals for the free-standing monolayers, E^{ML}_{shift}, the work-function mod-

Table 3.3: Changes in the vacuum energies ΔE_{vac}, energy shifts of the highest occupied orbitals for the free-standing monolayers E^{ML}_{shift}, work-function modifications $\Delta\phi$ and energy shifts of the highest occupied orbitals for the SAMs on metal E^{SAM}_{shift} for the systems with bipyrimidine and bidioxane shifting units. For the calculation of the energy shifts of the highest occupied orbitals see equation 1.6.4. The chemical structures of the systems are shown in Figure 3.2.3.

System	ΔE_{vac} / eV	E^{ML}_{shift} / eV	$\Delta\phi$ / eV	E^{SAM}_{shift} / eV
bipyrimdine, N_{down}	-0.93	-0.83	-1.64	-1.12
bipyrimdine, N_{up}	+0.71	+0.48	+0.09	-0.03
bidioxane, O_{down}	-1.33	-1.42	-2.22	-1.69
bidioxane, O_{up}	+1.00	+0.61	-0.13	+0.03

ifications, $\Delta\phi$, and energy shifts of the highest occupied orbitals for the SAMs on metal, E_{shift}^{SAM}, for the systems with the two shifting units. The magnitudes of the changes in the vacuum energies are higher for the free-standing monolayers with the bidioxane shifting unit than for the ones with the bipyrimidine unit. This is a consequence of the broken conjugation and structural effects in the monolayers with bidioxane that reduce charge rearangements counteracting its dipole moment. For the down configuration, N_{down} or O_{down} respectively, the magnitudes of the energy shifts of the highest occupied orbitals are several tenths of an eV higher in the free-standing monolayer (E_{shift}^{ML}) and the SAM on metal (E_{shift}^{SAM}) with bidioxane as shifting unit than in those with bipyrimidine. In contrast, for the up configuration, N_{up} and O_{up}, the orbital shift in the free-standing monolayer with bidioxane is about one tenth of an eV higer than in the monolayer with bipyrimidine. The orbital shifts in the two SAMs in up configuration are virtually zero. The reason for this is the asymmetry of the backbone of this monolayers due to the lack of a spacer unit between backbone and docking group. The SAM with bipyrimidine in N_{up} configuration exhibits Fermi-level pinning, as can be seen in Figure 3.2.4a. This Fermi-level pinning is the reason for the low magnitude of the work-function modification in this SAM. The cause for the low magnitude of the work-function modification in the SAM with bidioxane is caused by the bond dipole, no Fermi-level pinning occurs in this system, as shown in Figure 3.2.4b. In the SAMs in down configuration, N_{down} and O_{down}, no Fermi-level pinning occurs, as is apparent from the Unit-DOS plots in Figure 3.2.5 on page 81.

The LDOS contour maps of the free-standing monolayers with bipyrimidine (N_{down}: Figure 3.2.6 on page 82, N_{up}: Figure 3.2.8 on page 83) and with bidioxane shifting unit (O_{down}: Figure 3.2.7 on page 82, O_{up}: Figure 3.2.9 on page 83) are displayed below. These plots clearly show that the localization of the HOMO and the LUMO are much better in the free-standing monolayers with bidioxane than with bipyrimidine as shifting unit for both configurations (down and up). One can also see, that the global and local band gaps are higher in the monolayers with bidioxane as shifting unit compared to the monolayers with bipyrimidine.

Altogether, if one would only take the localization and the orbital shifts into account, the bidioxane unit would be a way better choice as a shifting unit. When takning a closer look at the results, one can conclude that the main reasons for the better localization in the systems with bidioxane, compared to the ones with byprimidine, are the large band gap of the bidioxane and the twists between the phenylrings of the backbone units it induces. As demonstrated by means of the Tour-wire-based backbones in chapter 2, it is possible to induce structural changes in the backbone in systems that use the bipyrimdine as shifting unit, too, e.g. by attaching methyl substituents. Additionally, the planarity of the biphenyl backbone in the monolayer with the bipyrimdine unit is an artifact of the geometry optimization. By using a different functional or starting geometry the backbone could get twisted in the molecule with bipyrimdine, too. The drawback of bidioxane as shifting unit is that the molecules based on it are not linear any more.

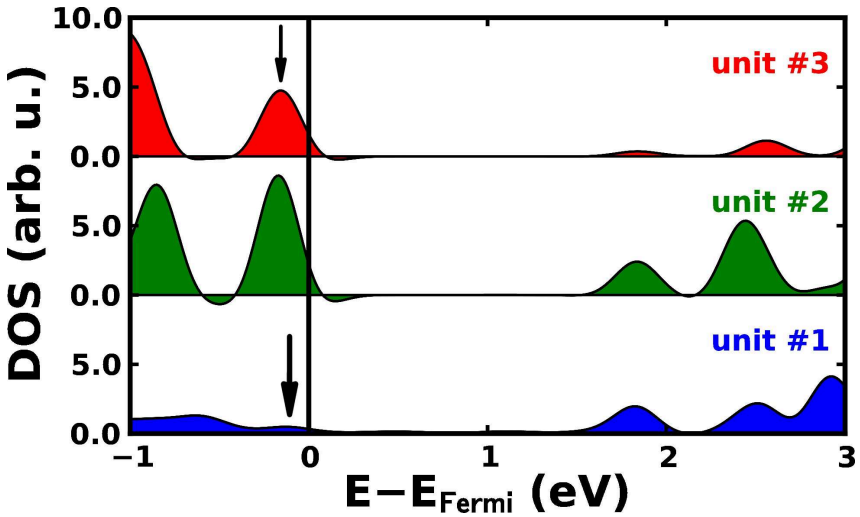

(a) SAM, bipyrimidine, N_{up}

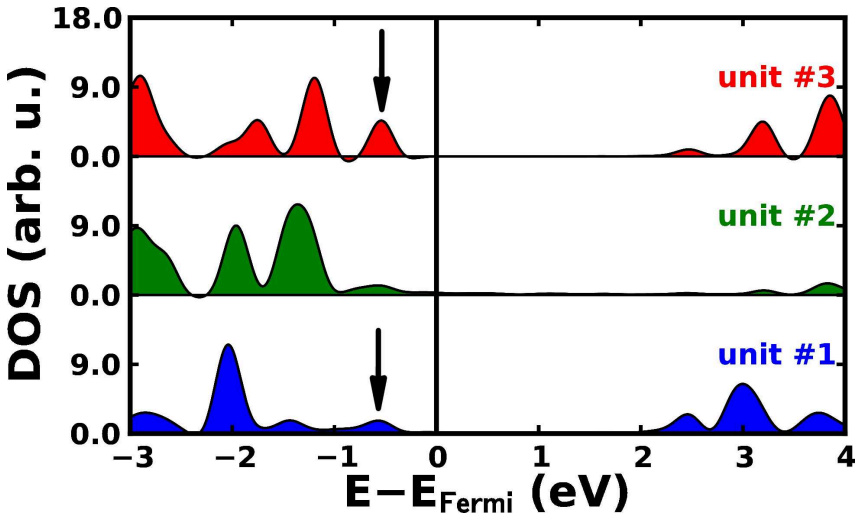

(b) SAM, bidioxane, O_{up}

Figure 3.2.4: Unit-DOS plots for the SAMs on gold of the molecules with bipyrimidine (a) and bidioxane (b) shifting units in N_{up} and O_{up} configuration. The black arrows indicate the peaks used for the calculation of the orbital shifts. For the chemical structures see Figure 3.2.3. The numbering and coloring of the units follows the color code in these sketches of the chemical structures.

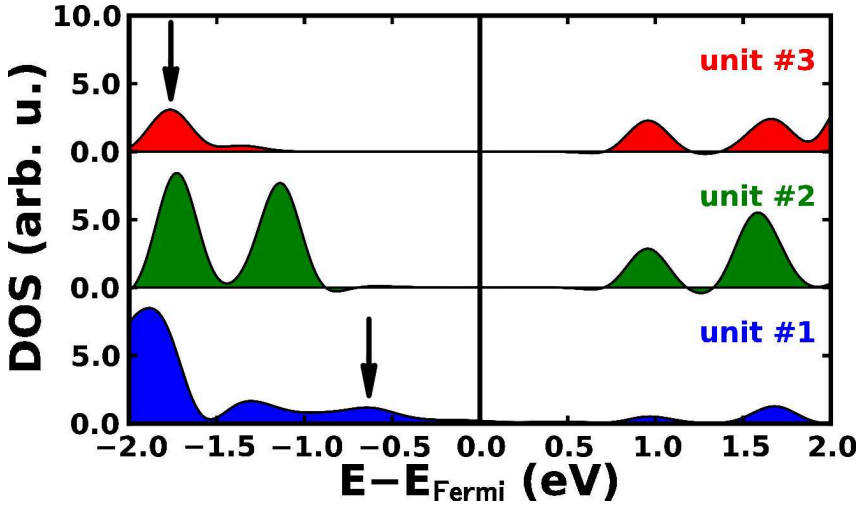

(a) SAM, bipyrimidine, N_{up}

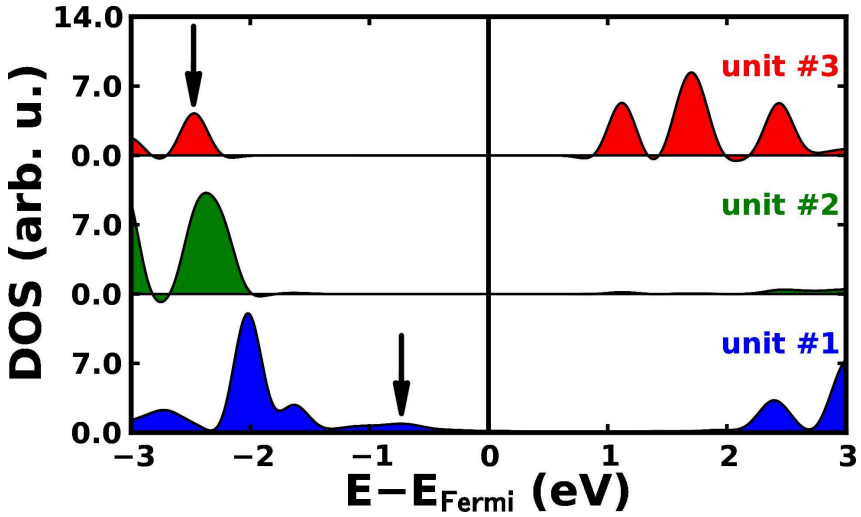

(b) SAM, bidioxane, O_{up}

Figure 3.2.5: Unit-DOS plots for the SAMs on gold of the molecules with bipyrimidine (a) and bidioxane (b) shifting units in N_{down} and O_{down} configuration. The black arrows indicate the peaks used for the calculation of the orbital shifts. For the chemical structures see Figure 3.2.3. The numbering and coloring of the units follows the color code in these sketches of the chemical structures.

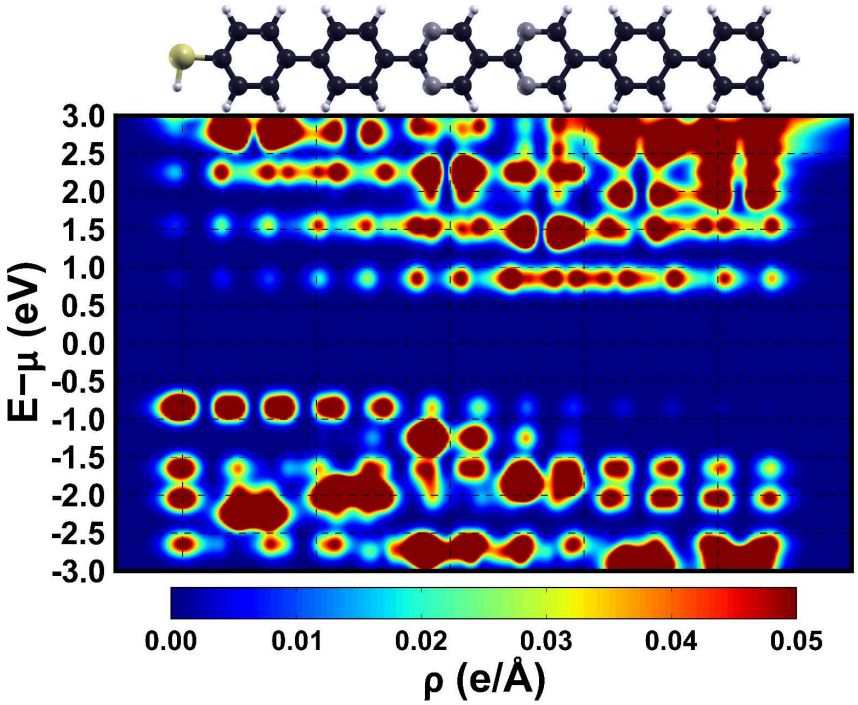

Figure 3.2.6: LDOS contour map of the free-standing monolayer with bipyrimidine shifting unit in N_{down} configuration. The structure above the LDOS map indicates the position of the molecule in the monolayer.

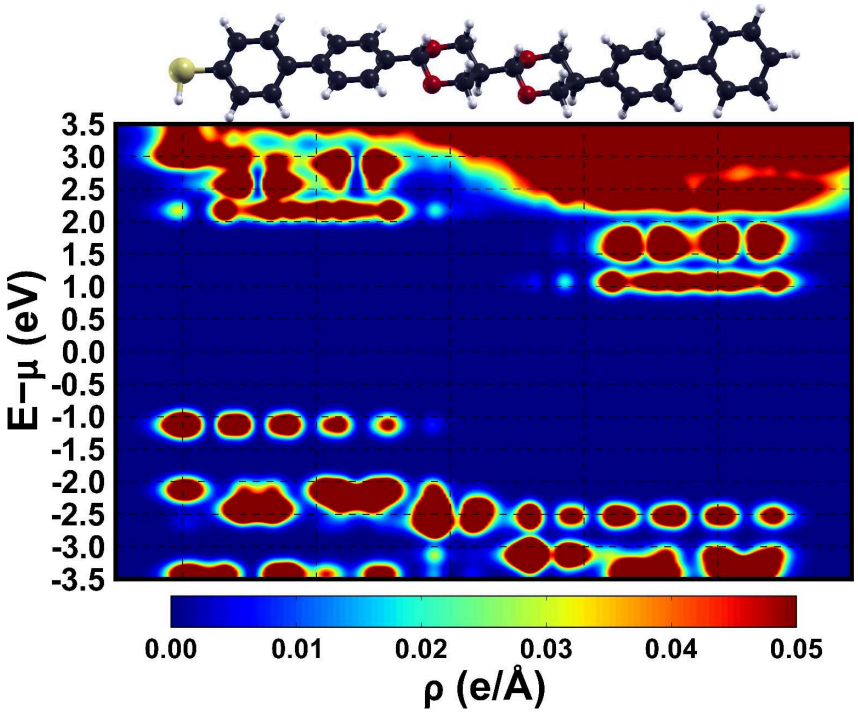

Figure 3.2.7: LDOS contour map of the free-standing monolayer with bidioxane shifting unit in O_{down} configuration. The structure above the LDOS map indicates the position of the molecule in the monolayer.

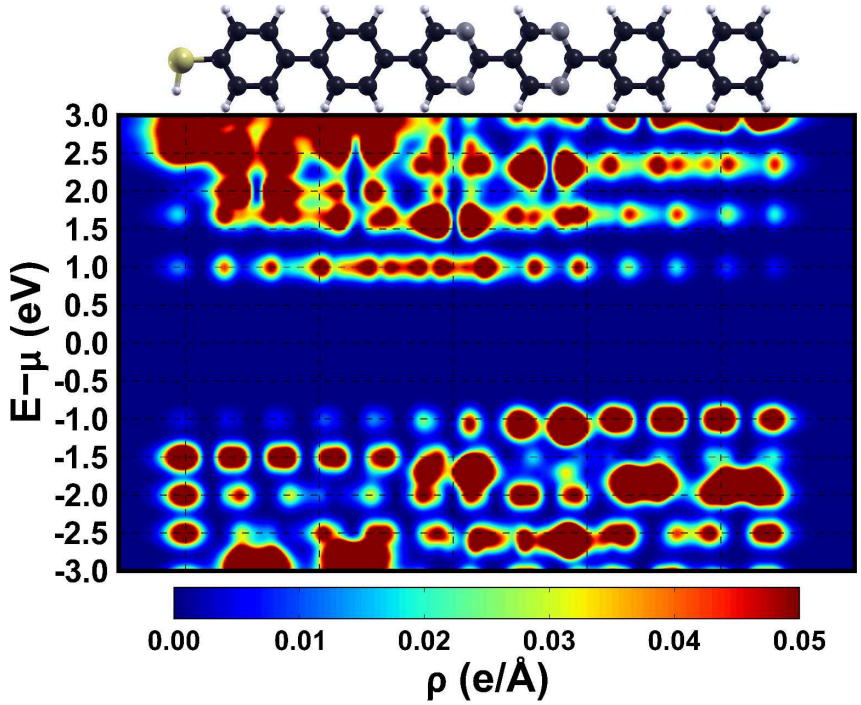

Figure 3.2.8: LDOS contour map of the free-standing monolayer with bipyrimidine shifting unit in N_{up} configuration. The structure above the LDOS map indicates the position of the molecule in the monolayer.

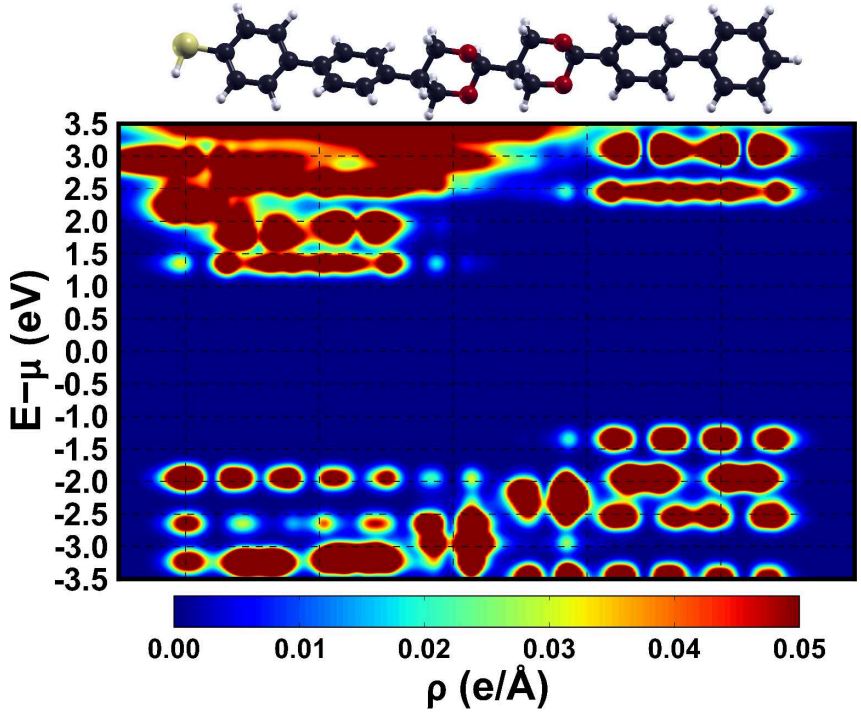

Figure 3.2.9: LDOS contour map of the free-standing monolayer with bidioxane shifting unit in O_{up} configuration. The structure above the LDOS map indicates the position of the molecule in the monolayer.

Chapter 4

Impact of Spacer Units and "more exotic" Backbones

The purpose of this chapter is on the one hand to show the influence of spacer units. These spacer units are either included between the substrate-side backbone unit and the thiol docking group (section 4.1) or between the backbone units and the bi-pyrimidine shifting units (section 4.2). For the first purpose a methyl spacer group was used and for the latter cyclohexane and Mg were distributed within the monolayer. Additionally, in this chapter a SAM composed of doped pyrene will be discussed (section 4.3), where the pyrene doping was done by substituting of the carbon atoms by nitrogen or boron. An important aspect of the discussion of doped pyrene SAMs will be how to treat open shell molecules.

4.1 Methyl-Spacer between Thiol and Backbone

When an organic molecule is bonded to a metal surface, surface states of the metal hybridize with states of the organic molecule. This leads to a DOS on parts of the organic molecule in the energy region of its band gap. This can drastically affect the quality of the localization drastically. From the literature one can learn that putting a methyl-spacer unit between the thiol and the delocalized π-system of the organic molecule can provide a handle to reduce the influence of the metal substrate.[7] Therefore, a methyl spacer was included between the thiol-group and the backbone for most of the systems investigated during this work. In this section it will be shown how this spacer unit affects the DOS in the vicinity of the Fermi-energy.

For the investigation of the effects of the spacer unit on the DOS, SAMs on metal substrate with biphenyl backbones and bipyrimidine as dipolar unit in N_{down} configuration were used, where in one SAM a methyl spacer was added between the thiol-group and the backbone.

Figure 4.1.1 shows the DOS projected onto the thiol-group (indicated in the plot by S) and the first two rings of the SAMs (indicated by R1 and R2) without (a) and with methyl spacer (indicated by CH2) (b). Additionally, for the latter also the DOS projected

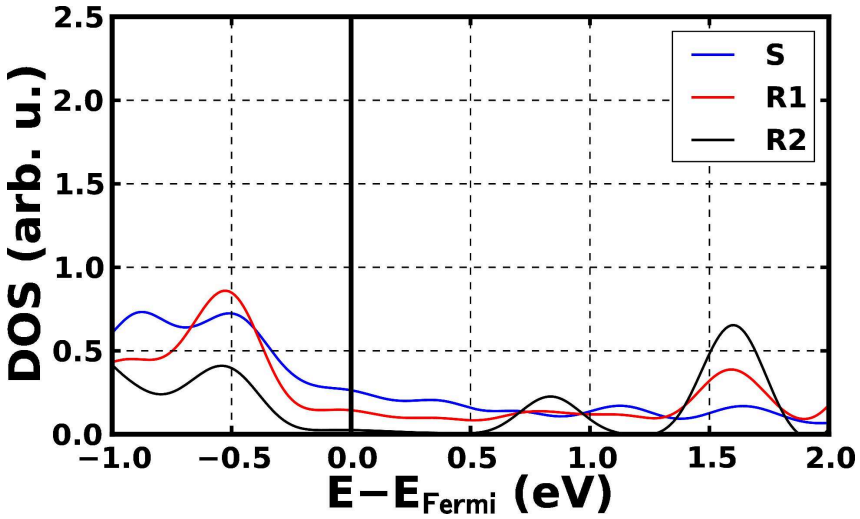

(a)

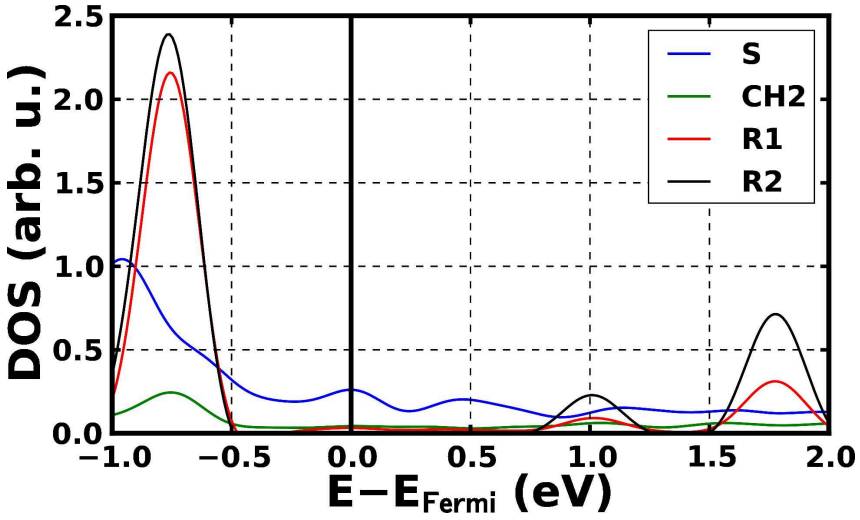

(b)

Figure 4.1.1: DOS projected onto the sulfur (S) and the first two carbon rings (R1 and R2) for the SAM without spacer unit (a) and additionally projected onto the methyl-group (CH2) for the SAM with spacer unit.

onto the methyl spacer is displayed. To point out the effects more clearly for both DOS plots the same scales for the energy and the DOS was used, even though the peaks for the SAM without spacer unit are quite low compared. From these plots one can see that the sulfur has a significant DOS in the region around the Fermi-energy in both cases. This DOS on the sulfur atoms displays no well resolved peaks which is a clear indicator that strong hybridization with metal states occurs. For the case of the SAM without spacer unit, as depicted in Figure 4.1.1a, one can see that the metal states also hybridize with the states of the first phenyl ring of the backbone, where the DOS at the Fermi-energy has approximately half ofthat on the sulfur atom. In the system with the spacer unit the states of the metal only hybridize with the sulfur states, while the DOS in the region

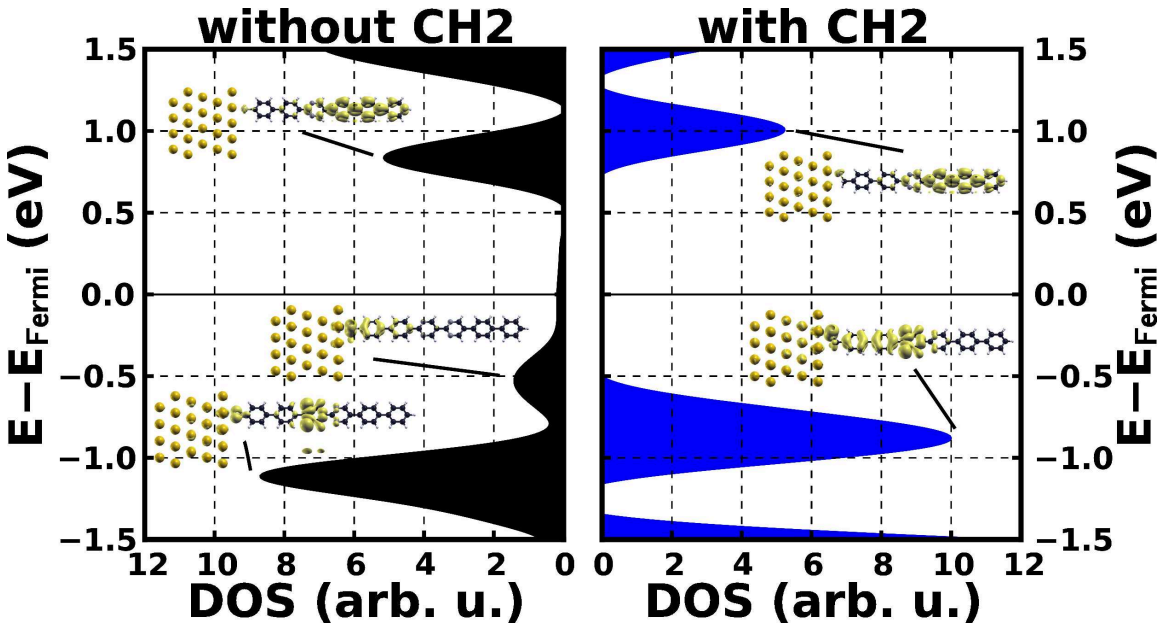

Figure 4.1.2: DOS and iso-density plots of the SAMs without and with methyl spacer group.

around the Fermi-energy is virtually zero for the spacer unit and the first two carbon rings.

In Figure 4.1.2 the DOS's projected onto the organic parts of the SAMs as well as iso-density plots for the HOMOs and LUMOs are shown. For the system without spacer unit also the iso-density plot for the HOMO-1 is displayed. One can clearly see that the spacer unit has no influence on the localization and the peak height of the LUMO, since it is localized on the vacuum-side and therefore far away from the region where the surface sates of the metal can exert influence on the adsorbed molecule. An interesting effect appears for the high-lying occupied peaks of this systems. In the SAM without spacer unit, there are two well resolved peaks at about $-0.5\,\text{eV}$ and $-1.1\,\text{eV}$ respectively. The first one is a sulfur state spreading out onto the first two carbon rings, as can be seen from the associated iso-density plot. The latter one corresponds to a superposition of a σ-state on the pyrimidine ring closer to the surface, a sulfur state and states with very low DOS on the carbon ring next to the pyrimidine ring on the substrate-side and on the second pyrimidine ring. The addition of the methyl spacer unit causes these two peaks to overlap, as can be seen when comparing the heights of the peaks and the corresponding iso-density plots.

One can conclude that the introduction of the methyl spacer unit results in a decoupling of the organic part of the adsorbed molecule from the metal surface. This is an effect that is desirable. But the introduction also has a down side, at least for the system investigated in this section, namely it causes states to overlap. This is especially for the biphenyl backbone systems undesirable since a pyrimidine σ-state is involved. Pyrimidines posses close-lying π- and σ-states in the region of the HOMO-LUMO gap.[26] The localization of these states varies significantly.[26] It has been shown that the error in the description of states in DFT depends on their localization but not on their character (π

or σ), the better the state is localized the higher is the error.[26] Since the σ-states in the vicinity of the HOMO-LUMO gap in the molecules calculated in this work are localized stronger than the π-states, the description of σ-states is less accurate. Therefore, an overlap of π- and σ-states is undesirable, especially, in the frontier states. In the twisted Tour-wire based SAMs no overlap of π- and σ-states occurs in the HOMO and LUMO. However, for the purpose of localization it is still preferably to reduce the influence of the substrate by using a methyl spacer. Therefore most of the systems investigated in the scope of this work were calculated with a methyl spacer unit.

4.2 Including Spacer Units in the Backbone

The purpose of building spacer units into the backbone of a molecule is to break the conjugation and therefore prevent the electron wave-functions from spreading out over the whole molecule. This should lead to an improvement of the localization. Of course, the spacer units itself also have to be of a non-conjugated nature. Therefore, geometrical issues can arise since non-conjugated elements are often very flexible. The usefulness of the molecules used in this part of the work has completely been disregarded since only the theoretical potential of spacer units within molecules should be pointed out.

The spacer units used for the separation of different parts of the monolayers were cyclohexane and magnesium. Cyclohexane was chosen since it is a non-conjugated carbon ring and magnesium for its ability to form only two bonds. Figure 4.2.1 shows the chemical structures of the molecules with cyclohexane (a) and Mg (b) incorporated into their backbones. The different colors show the segmentation of the molecules into different units. For the calculations of the monolayer with the cyclohexane spacer unit a $2\sqrt{3} \times 3$ unit cell was used, while the one with the Mg spacer was placed in a $\sqrt{3} \times 3$ unit cell.

One might ask why methyl, which does a good job in decoupling an organic molecule from a metallic substrate as shown in section 4.1, was not used to separate different units of the monolayer. The reason is that due to the bond angle of the methyl group the resulting molecules would have a stair-like geometry, as a simple geometry optimization of a gas phase molecule with methyl spacers within the backbone showed.

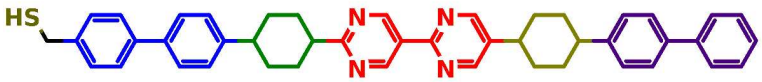

(a)

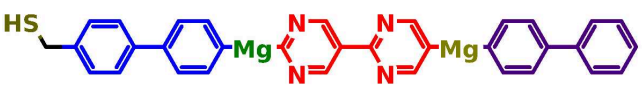

(b)

Figure 4.2.1: Chemical structures of the molecules with cyclohexane (a) and Mg (b) spacer units built into the backbone. Colors indicate the segmentation into different units.

4.2.1 Cyclohexane Spacer

Cyclohexane can exist in various different conformations, e.g. the so-called *chair* and *boat* conformations.[64] The boat conformation has a u-like shape and, therefore, would produce a geometry useless for building SAMs. Only cyclohexane in the chair conformation can be used to build a molecule which is at least almost planar and forms no steps. Luckily, the chair conformation has the lowest energy of all cyclohexane conformations

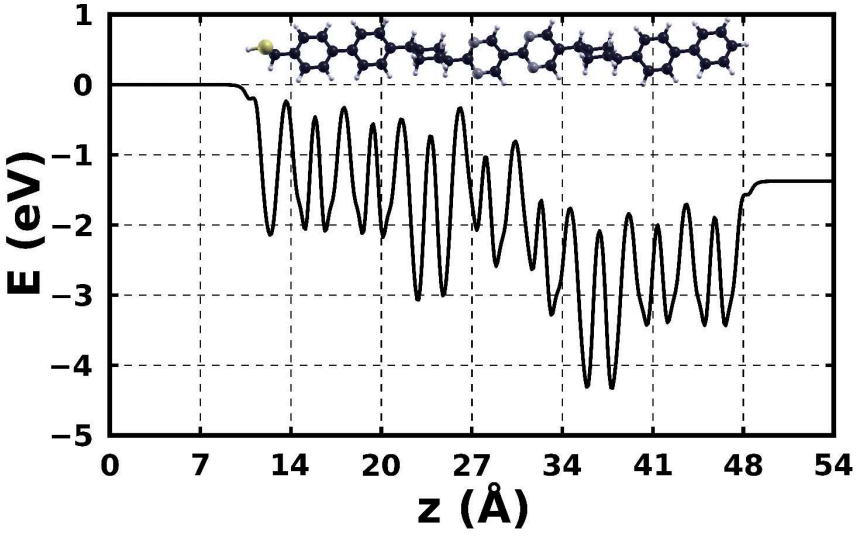

(a)

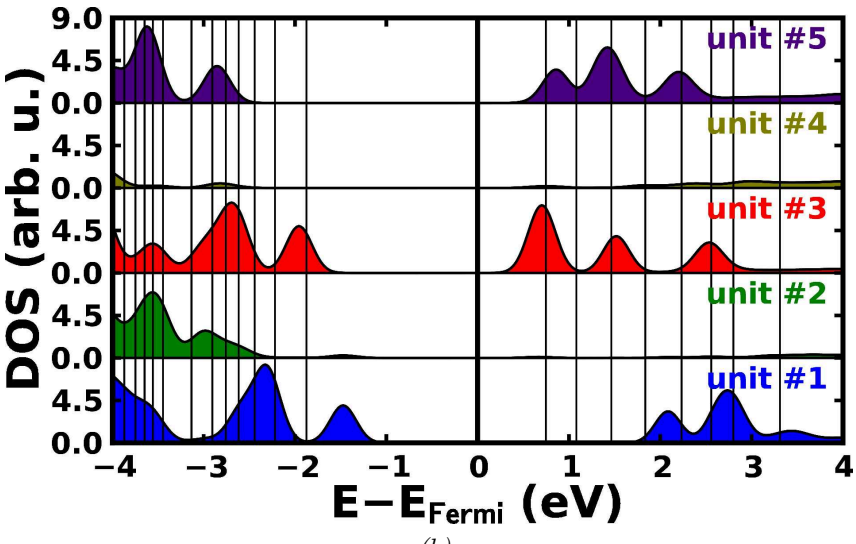

(b)

Figure 4.2.2: Electron potential energy (a) and Unit-DOS (b) for the free-standing monolayer with the cyclohexane spacer unit within the backbone. The vertical lines in the Unit-DOS indicate the energy levels containing two states. The numbering and coloring of the units follows the color code in the sketch of the chemical structure in Figure 4.2.1. Units #1 and #5 are the substrate-side and the vacuum-side backbone units, units #2 and #4 are the spacer units and unit #3 is the bipyrimidine unit.

and, hence, it should be possible to synthesize cyclohexane in this conformation.[64]

Figure 4.2.2a shows the electron potential energy of the free-standing monolayer with the cyclohexane spacer unit incorporated between the phenyl backbone units and the bipyrimidine. One can see that the jump in the vacuum energy is about $-1.37\,\mathrm{eV}$. Compared to a monolayer with the same backbone but without cyclohexane spacer units the change of the vacuum energy is increased significantly. The potential drop occurs within the bipyrimidine unit, which is in agreement with theoretical expectations and the experience from the monolayers without spacer units within the backbone.

The Unit-DOS of the monolayer with the cyclohexane spacer unit is depicted in Figure 4.2.2b. The vertical lines in the Unit-DOS plot indicate the energy intervals containing two states and should help identifying the localization behavior of the monolayer. From this plot, one can see that the cyclohexane spacer units (#2 and #4) have no DOS in the vicinity of the frontier states of the free-standing monolayer. In the energy range considered in this plot, the cyclohexane rings have no significant amounts of states above the Fermi-energy. The localization of the frontier states in the monolayer with cyclohexane spacers is similar to their localization in the monolayer without scpacer units. The HOMO is localized on the substrate-side unit (#1) and on the bipyrimidine unit (#3). The LUMO is localized on the bipyrimidine (#3) and the vacuum-side unit (#5). It seems that the LUMO+1 and LUMO+2 are localized in a similar way as the LUMO. The LUMO+4 has DOS on the substrate-side and the vacuum-side units but not on the other units.

Summarizing one can say that the incorporation of cyclohexane into the backbone leads to a higher magnitude in the change of the vacuum energy and to a very different electronic structure, especially concerning the unoccupied states. It seems that even states significantly above the LUMO can be localized quite well.

4.2.2 Mg Spacer

The important question for the determination of the applicability of Mg as a spacer unit is whether its bonding angle is close to 180°. The fact that Mg can make exactly two bonds might lead to a sp-hybridization and therefore to a bond angle of 180° like it happens in magnesium hydride.[65] Indeed, the geometry optimization of the molecule with Mg as spacer unit performed with Gaussain03 using the PBE[43] functional and the 6-31G* basis set resulted in bond angles between 177° and 179° for the two Mg atoms respectively.

The electron potential energy of the free-standing monolayer with Mg as spacer unit in N_{down} configuration is displayed in Figure 4.2.3a. The jump in the vacuum energy is about $-1.80\,\mathrm{eV}$ for this monolayer. Therefore its magnitude is about 1 eV higher than for a similar monolayer without spacer units and about 0.4 eV higher than for the monolayer with cyclohexane spacer units.

From the Unit-DOS in Figure 4.2.3b one can see that the localization is not as good as with a Tour-wire based backbone. Both frontier orbitals, the HOMO and the LUMO, have a significant amount of DOS on the bipyrimidine unit. Besides that,the HOMO is mostly localized on the substrate-side unit (#1). In contrast, the LUMO is localized

almost to equal degrees on the bipyrimidine and the vacuum-side unit (#5). The spacer units essentially do not contribute to the DOS in the cosidered energy window.

Besides the fact that the bond angle of magnesium built into a molecule consisting of biphenyl and bipyrimidine units might not be exactly 180°, it is obviously not the best choice in terms of improvement of the localization. The results clearly indicate that the

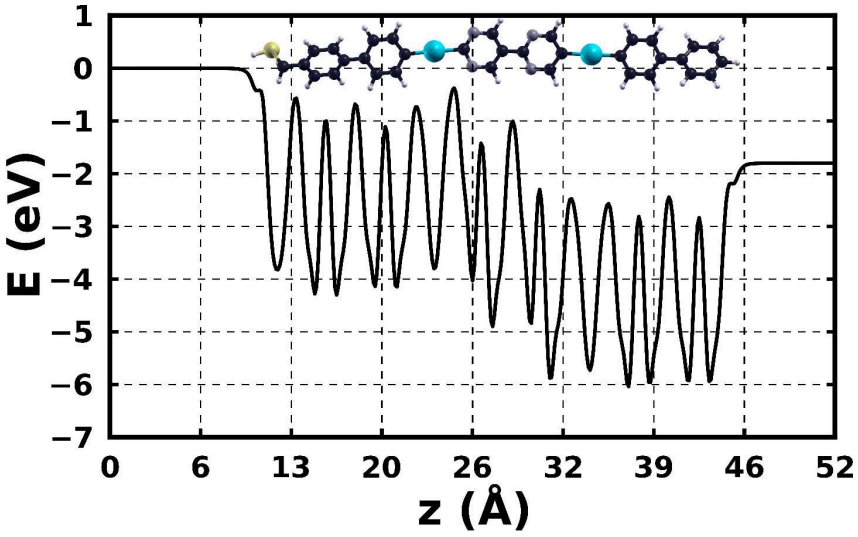

(a)

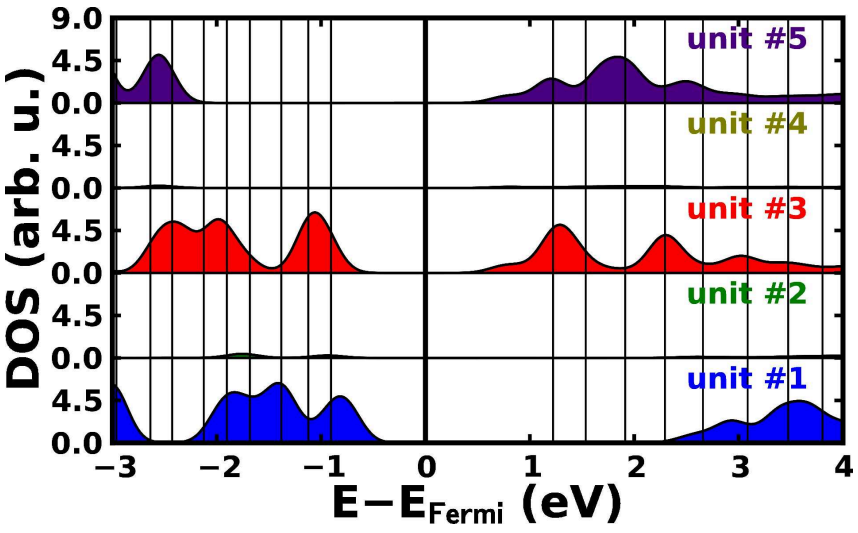

(b)

Figure 4.2.3: Electron potential energy (a) and Unit-DOS (b) for the free-standing monolayer with the Mg spacer unit within the backbone. The vertical lines in the Unit-DOS indicate the energy levels containing two states. The numbering and coloring of the units follows the color code in the sketch of the chemical structure in Figure 4.2.1. Units #1 and #5 are the substrate-side and the vacuum-side backbone units, units #2 and #4 are the spacer units and unit #3 is the bipyrimidine unit.

localization is not as good as for example in the Tour-wire based monolayers with methyl substituents. The localization of the frontier orbitals in the monolayer with Mg spacer units is very similar to the localization in the monolayer with cyclohexane spacers.

4.3 Pyrene

It has been shown that doping of a pyrene based molecular wire can improve its transport properties significantly.[44] This doping was done by a substitution of one of the pyrenes carbon atoms with nitrogen or boron.[44] The impact of doping a molecular wire is similar to that of doping an inorganic semiconductor. In both cases, the doping induces a rise in the conductivity. In inorganic semiconductors, the rise of the conductivity is caused by an increase of free charge carriers due to the doping. In contrast, in the pyrene based molecular wire the doping causes a partially occupied state to be pinned to the Fermi-energy of the metal electrodes.[44] To provide a continous transport channel in the doped molecular wire, the partially occupied state has to be delocalized over the entire molecular backbone.[44] In the light of these findings, doped pyrene was embedded in a SAM with biphenyl-based backbone to enable zero-bias conduction.

The chemical structure of the pyrene-based molecule with biphenyl backbone is shown in Figure 1.4.5. The carbon atom which is substituted by boron or nitrogen is marked by the X.

A look at the energy levels of the pyrene-based molecules in gas phase in Figure 4.3.2 reveals that the nitrogen and boron doped analogues exhibit similarities to the classical n- and p-doped semiconductors. The nitrogen doped pyrene-based molecule has an occupied state with an energy close to the energies of the unoccupied states, a situation similar to the band structure of an n-doped semiconductor. In contrast, doping the pyrene-based molecule with boron leads to an unoccupied state with an energy near the energies of the occupied states, this corresponds to a p-doped semiconductor. In both cases, the states resulting from doping are restricted to one particular spin and, therefore, are the source of the magnetization in the pyrene-based doped molecules. This magnetization might exist in the free-standing monolayer only. Due to coupling of the states of the organic part to states of the metal this magnetization could be lost in the case of the SAM on gold.

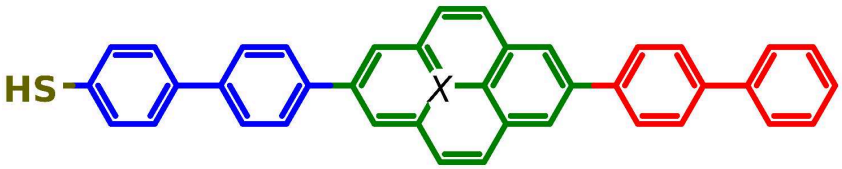

Figure 4.3.1: Chemical structure of the pyrene-based molecule with biphenyl backbone. The colors indicate the segmentation into different units. The X marks the carbon atom which is substituted by boron or nitride.

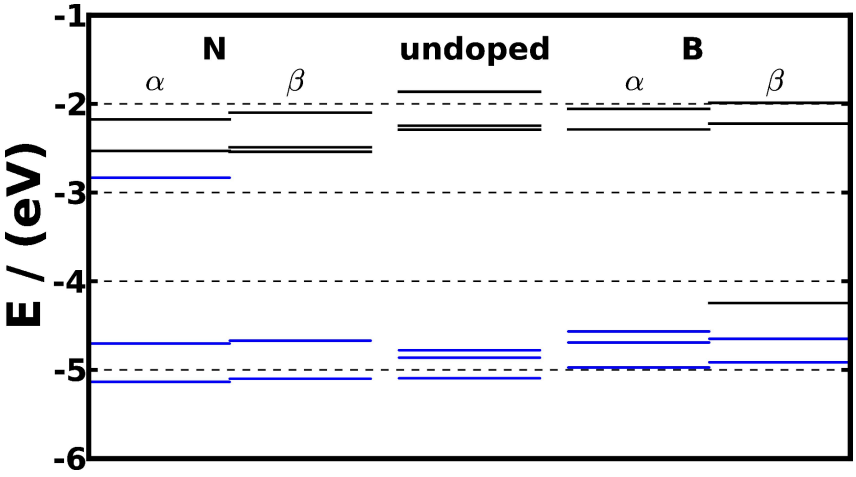

Figure 4.3.2: Energy levels of occupied (blue) and unoccupied (black) frontier states of the N- and B- doped and the undoped pyrene-based molecule. α and β stand for the two different spins a state can have.

4.3.1 Challenges in Calculations of Systems with Open Shell Atoms

The treatment of molecules possessing a magnetic moment in DFT simulations needs to be done by spin unrestricted calculations. In spin unrestricted calculations, the DOS can be different for the two different spin channels. To do a spin unrestricted calculation in VASP[50] one has to set `ISPIN=2` in the `INCAR` file.[52] The problem for this kind of calculations in VASP[50] is that they can cause problems with the convergence and can lead to strange values for the magnetization. VASP[50] provides a few input parameters to improve the results of these calculations.[52] Detailed descriptions of the parameters changed in this section can be found in the VASP user guide.[52] While the calculations for the boron doped monolayer and SAM on metal substrate actually worked quite well, the results for the nitrogen doped monolayer and SAM were pretty bad in the beginning. Therefore, different tests were performed for the nitrogen doped molecule and the VASP[50] input parameters that helped improving the results are presented in this subsection. Summaries of the results for the different calculation setups can be found in Table 4.1 and Figure 4.3.3 for the free-standing monolayer and in Table 4.2 and Figure 4.3.4 for the SAM bonded to the substrate.

Nitrogen doped monolayer:

Standard: First a "standard" simulation of the monolayer was performed. This standard simulation consisted of a calculation without dipole correction followed by a calculation with dipole correction using the converged `CHGCAR` and `WAVECAR` of the calculation without the dipole correction. The problem with this simulation was that it resulted in a final magnetization of the monolayer of $-0.66\,\mu_{\text{Bohr}}$. Since for a free-standing monolayer an electron, or a part of it, can not simply disappear it should have a magnetization of $\pm 1\,\mu_{\text{Bohr}}$. This might be due to the artificial smearing of the partial occupancies. For

systems with unoccupied states close to the Fermi-energy the spin information can be erased by the artificial smearing.[66]

MAGMOM-tag: As the standard calculation procedure did not lead to the expected magnetization, it was tried to set the initial magnetization by hand. This calculation was only performed with dipole correction. For the purpose of manually setting the initial magnetization VASP[50] provides the MAGMOM-tag.[52] With this tag the initial magnetization of the monolayer was set to $1\,\mu_{\mathrm{Bohr}}$ on the nitrogen atom and to $0.1\,\mu_{\mathrm{Bohr}}$ on the three carbon atoms neighboring the nitrogen, resulting in an net initial magnetization of $1.3\,\mu_{\mathrm{Bohr}}$. The reason for choosing an initial magnetization larger than $1\,\mu_{\mathrm{Bohr}}$ is a suggestion from the VASP user guide.[52] According to this document, a higher initial magnetization can help the VASP[50] caculation to converge to the correct final magnetization.[52] The final magnetization of this simulation was $0.6584\,\mu_{\mathrm{Bohr}}$. So only setting the initial magnetization did not lead to the correct result.

NUPDOWN-tag: The NUPDOWN-tag can be used to freeze the difference between the numbers of spin up and spin down electrons in spin unrestricted calculations. In the next test, it was set to one. In this case, of course, the final magnetization has the correct value. From the DOS of this test shown in Figure 4.3.3 one can see that no spin polarized partially occupied state close to the LUMO exists, as it should be according to Figure 4.3.2.

N+M-tags: In this setup the MAGMOM-tag and the NUPDOWN-tag were both set the same way as described above. The result is virtually the same as for the setup where only the NUPDOWN-tag was set.

SIGMA = 0.02: It has been shown that the reduction of the broadening of the partial occupancies can help the calculation to converge to the correct mangetization.[66] The parameter SIGMA in the VASP[50] input file defines how strong the partial occupancies and therefore the DOS are broadened in the calculation to improve convergence.[52] The standard value for SIGMA that was used in this work was 0.2. For this test, SIGMA was set to 0.02, a tenth of the standard value. Additionally the MAGMOM-tag was used to set the initial magnetization to the nitrogen atom and its neighboring carbon atoms. As described above, the initial magnetization for the nitrogen atom was set to $1\,\mu_{\mathrm{Bohr}}$ and for the three carbon atoms to $0.1\,\mu_{\mathrm{Bohr}}$. So the net initial magnetization was $1.3\,\mu_{\mathrm{Bohr}}$. The simulation led to a net final magnetization of $1.00\,\mu_{\mathrm{Bohr}}$ and the DOS showed occupied states just below the Fermi-energy for one spin and, therefore, displayed the expected behavior. From all the tested setups for the free-standing monolayer this one led to the most realistic results.

SIGMA = 0.002: This setup is the same as the one described in the last subparagraph but the broadening was further reduced, SIGMA was set to 0.002. This resulted in a final magnetization of $0.50\,\mu_{\mathrm{Bohr}}$ and occupied states for both spins occurred slightly below the Fermi-energy. The low magnetization in this test might be due to the k-point

sampling. When using too few k-points in combination with a small broadening, the energetic splitting between peaks associated with individual k-points will become large. This can lead to significant changes in the magnetization when the DOS's of the different spin configurations are shifted.

The most important results from these tests for the free-standing monolayer are summarized in Table 4.1. Figure 4.3.3 shows the spin resolved DOS's projected onto the organic parts for the different tests. The setup with the broadening reduced to 0.02 and a set `MAGMOM`-tag delivered the best results.

Table 4.1: Total energies, Fermi-energies, initial and final magnetizations of the nitrogen doped free-standing monolayer for different setups.

Setup	E_{tot} (eV)	$Mag_{initial}$ (μ_{Bohr})	Mag_{final} (μ_{Bohr})
Standard	-455.42	-	-0.66
`MAGMOM`-tag	-455.42	1.3	0.66
`NUPDOWN`-tag	-455.41	1.0	1.00
`M+N`-tags	-455.41	1.3	1.00
`SIGMA` = 0.02	-455.40	1.3	1.00
`SIGMA` = 0.002	-455.40	1.3	0.50

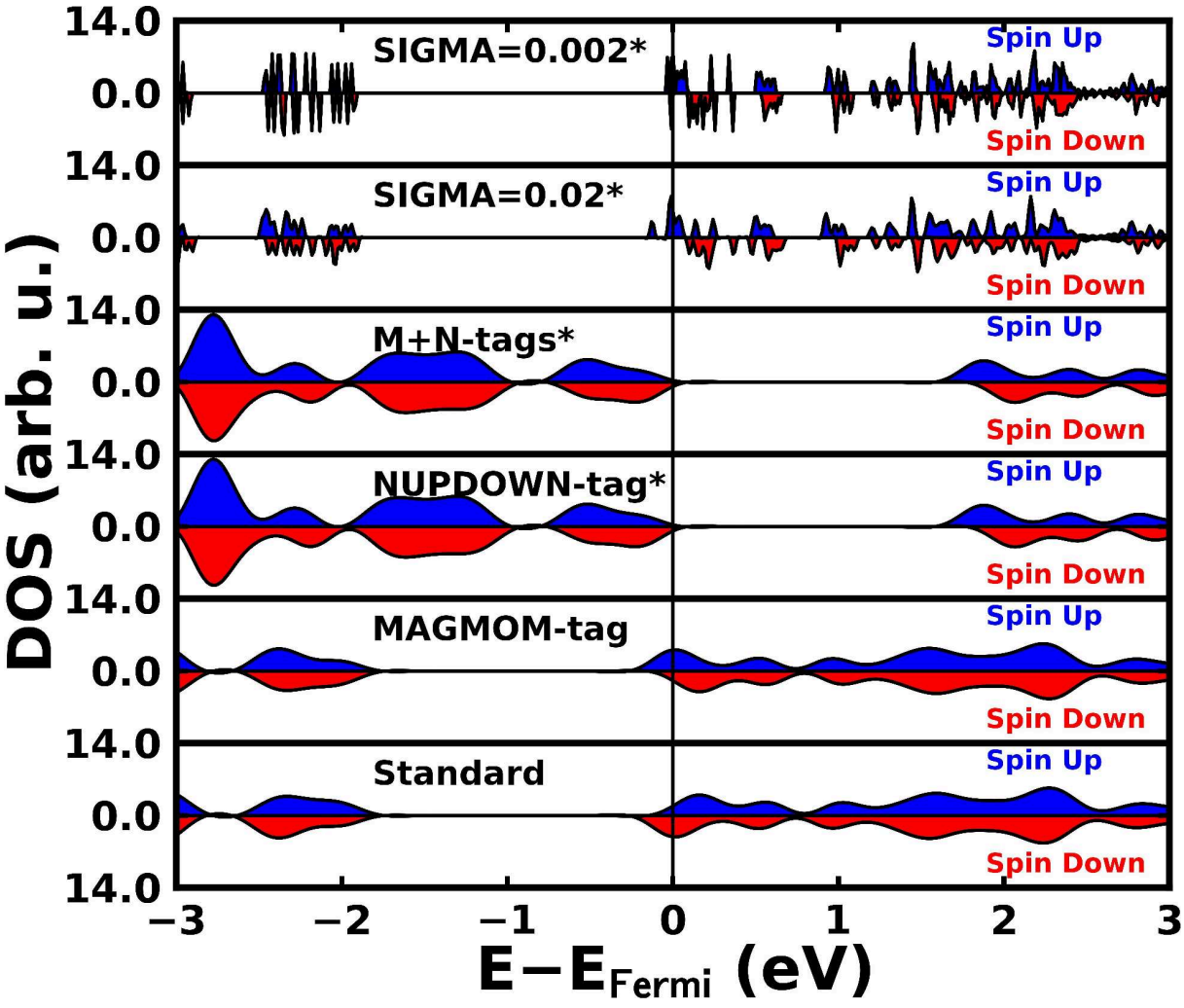

*Figure 4.3.3: DOS's projected onto the organic parts for the spin up and spin down channel of the different tests for the free-standing monolayer. For the tests marked with an * the DOS was multiplied by a factor of 0.5.*

Nitrogen doped SAM on metal: For the SAM on substrate it is not quite so easy to determine whether the obtained results are sensible. This is because the magnetization has only a limited informative value, as charge transfer from the monolayer to the substrate during the bonding process or a coupling of states of the organic parts and with states from the substrate can reduce the magnetization. The following tests were, nevertheless, performed:

Standard: As described above for the monolayer, the standard calculation procedure consists of calculations without and with dipole correction, where for the latter the converged `CHGCAR` and `WAVECAR` from the first one were used as input. The resulting final magnetization had a value of $-0.07\,\mu_{\text{Bohr}}$. This is very low and would mean a strong coupling of states of the organic parts with states from the substrate.

`MAGMOM`-tag: In this setup the initial magnetization was set using the `MAGMOM`-tag. Like for the free-standing monolayer, the initial magnetization of the nitrogen atom was set to $1\,\mu_{\text{Bohr}}$ and the initial magnetizations of the three carbon atoms bonded to the nitrogen were set to $0.1\,\mu_{\text{Bohr}}$. The resulting final magnetization assumed a value of $0.11\,\mu_{\text{Bohr}}$. This value is still very low since it would require the unpaired electron of the nitrogen to transfer almost entirely to the substrate.

Higher starting magnetization: Here the initial magnetization for the nitrogen and its neighboring carbon atoms was doubled compared to the previous setup. This led to an initial magnetization of $2.6\,\mu_{\text{Bohr}}$. The final magnetization had a value of $0.64\,\mu_{\text{Bohr}}$, which compared to the final magnetizations produced by the previous test is a quite reasonable value.

`NBANDS`=370: Starting from a converged spin restricted calculation, a spin unrestricted calculation with a higher number of bands included (set by `NBANDS`-tag) and the initial magnetization set to $2.6\,\mu_{\text{Bohr}}$, like in the previous setup, was performed. The resulting final magnetization has a value of $0.21\,\mu_{\text{Bohr}}$.

Starting magnetization from free-standing monolayer: In this setup the initial magnetization for the organic parts of the SAM was taken from the final magnetization of the calculation of the free-standing monolayer with `SIGMA`=0.02. The initial magnetization for the SAM was distributed like in the monolayer but the values were slightly increased, following a suggestion in the VASP user guide[52], resulting in an initial magnetization of $1.178\,\mu_{\text{Bohr}}$. The final magnetization assumed a value of $0.13\,\mu_{\text{Bohr}}$.

Starting from spin restricted calculation: For this calculation the `CHGCAR` and `WAVECAR` files from a converged spin restricted calculation were used as starting point. Additionally the `MAGMOM`-tag was used to set the initial magnetization of the nitrogen atom to $1\,\mu_{\text{Bohr}}$ and of the neighboring three carbon atoms to $0.1\,\mu_{\text{Bohr}}$. At the end of the calculation the magnetization assumed a value of $-0.06\,\mu_{\text{Bohr}}$.

SIGMA = 0.02, CHGCAR not read: Calculations without and with dipole correction were performed with reduced broadening (SIGMA=0.02) and the initial magnetization set according to the final magnetization of the free-standing monolayer using the MAGMOM-tag. For the calculation with dipole correction only the WAVECAR but not the CHGCAR file of the converged calculation without dipole correction was used as input. This setup led to a final magnetization of $1.10\,\mu_{\mathrm{Bohr}}$.

SIGMA = 0.02: The same procedure as described for the previous setup but for the calculation with the dipole correction the WAVECAR and the CHGCAR were used as input. This led to a final magnetization of about half the magnitude than for the previous setup, namely of $0.50\,\mu_{\mathrm{Bohr}}$.

An overview of the most important quantities for the different setups for the SAM are given in Table 4.2. Figure 4.3.4 shows the spin resolved DOS's projected onto the organic parts for the different tests. One can see that the DOS's and total energies of all tests are very similar. Since it is not quite clear which value the magnetization should assume for the SAM, it is difficult to determine which setup leads to the best results. The most reasonable results are delivered by the calculations with reduced broadening since for them the change from the initial magnetizations to the final magnetizations are the lowest.

Table 4.2: Total energies, Fermi-energies, initial and final magnetizations of the nitrogen doped SAM for different setups

Setup	E_{tot} (eV)	$Mag_{initial}$ (μ_{Bohr})	Mag_{final} (μ_{Bohr})
Standard	-545.93	-	-0.07
MAGMOM-tag	-545.93	1.300	0.11
Higher Startmagnetization	-545.91	2.600	0.64
NBANDS=370	-545.93	2.600	0.21
Startmagnet. fr. ML	-545.93	1.178	0.13
Start fr. non-magn. calc.	-545.93	1.300	-0.06
SIGMA = 0.02, CHGCAR not read	-545.92	1.178	1.10
SIGMA = 0.02	-545.89	1.178	0.50

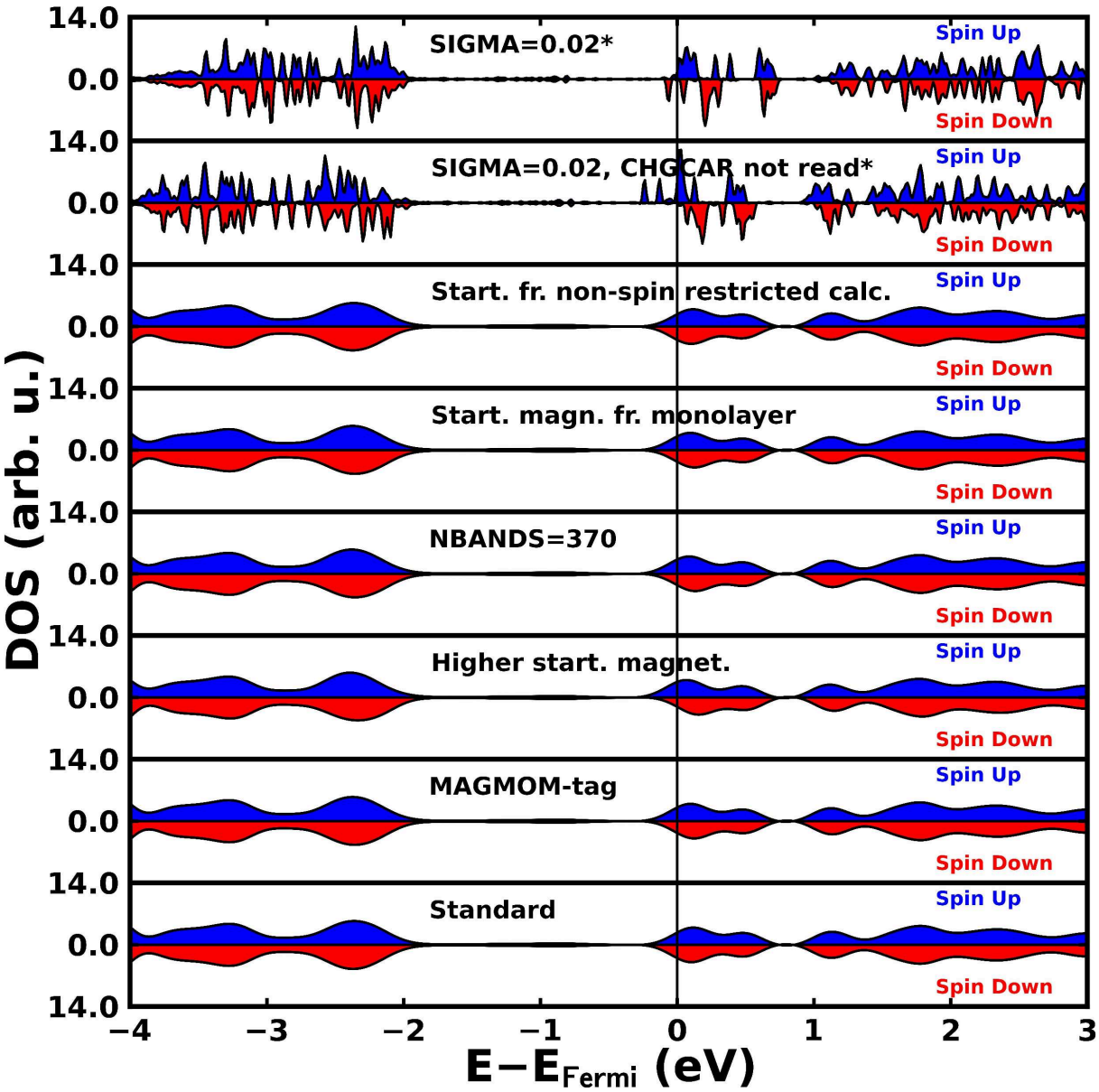

*Figure 4.3.4: DOS's projected onto the organic parts for the spin up and spin down channel of the different tests for the SAM on metal. For the tests marked with an * the DOS was multiplied by a factor of 0.8.*

4.3.2 N-doped

Based on the converged `WAVECAR` and `CHGCAR` files of the calculation with reduced smearing (`SIGMA`=0.02) and a higher start magnetization a non-self-consistent calculation with Gaussian smearing and `SIGMA`=0.2 was performed. The use of Gaussian smearing was necessary to obtain the DOS in a form which can be integrated. The final magnetization was 1.00 μ_{Bohr}.

Figure 4.3.5 shows the electron potential energy (a) and the spin resolved Unit-DOS (b) for the nitrogen doped free-standing monolayer. From the electron potential energy one

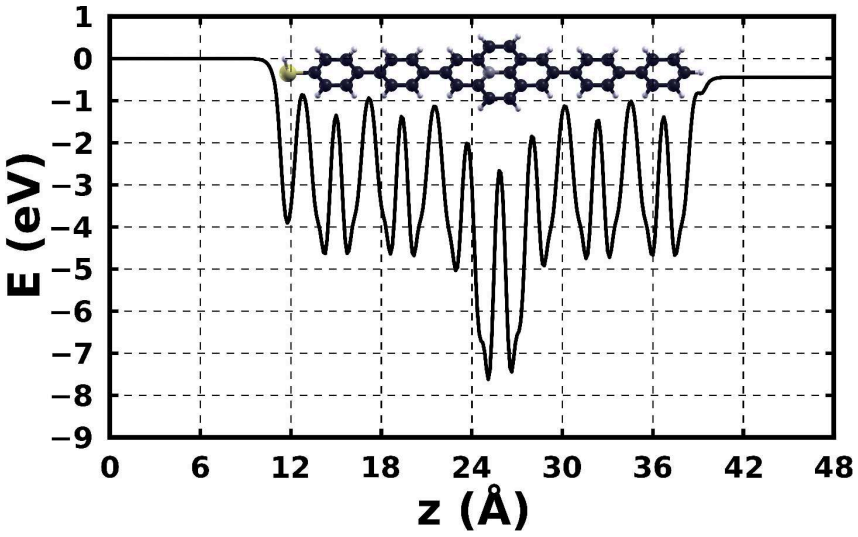

(a)

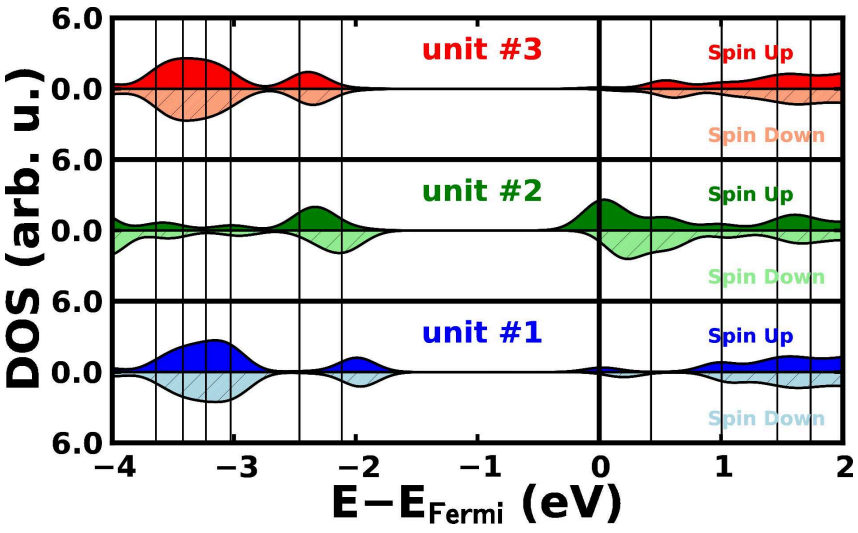

(b)

Figure 4.3.5: Electron potential energy (a) and spin resolved Unit-DOS (b) for the nitrogen doped free-standing monolayer. The vertical lines indicate energy intervals containing two states. The numbering and coloring of the units follows the color code in the sketch of the chemical structure in Figure 4.3.1.

can see that the monolayer produces a jump in the vacuum energy of about $-0.44\,\mathrm{eV}$. For the undoped pyrene-based monolayer with biphenyl backbone the change in the vacuum energy is about $-0.25\,\mathrm{eV}$. This means that due to the nitrogen doping an additional net dipole moment occurs. This additional dipole moment is caused by the asymmetric substitution of one of the carbon atoms by nitrogen.

The spin resolved Unit-DOS displays that there are occupied states for spin up on the pyrene unit (#2) and on the substrate-side unit (#1) near the Fermi-energy. On the latter one the intensity of the DOS near the Fermi-energy is very low. A little bit unexpected is that the HOMO is localized on the already mentioned pyrene and substrate-side units while the DOS of the vacuum-side unit (#3) does not contribute to the HOMO. For the LUMO most of the states are localized on the pyrene unit. Apparently, there are overlapping states in the LUMO.

The most important result is the occurrence of a partially filled band around the Fermi-energy. This is in agreement with the calculation for the molecule in gas phase, as shown in Figure 4.3.2.

4.3.3 B-doped

The calculation of the boron doped free-standing monolayer caused much fewer problems than the one for the nitrogen doped monolayer. For the case of the boron doped monolayer the standard calculation procedure of performing a single point calculation without dipole correction followed by a calculation with dipole correction using the converged `WAVECAR` and `CHGCAR` files from the first calculation as input worked already quite well. The resulting final magnetization of the monolayer was $1.01\,\mu_{\mathrm{Bohr}}$.

The electron potential energy (a) and the spin resolved Unit-DOS (b) are depicted in Figure 4.3.6. Doping the monolayer with boron leads to a change in the vacuum energy of circa $+0.31\,\mathrm{eV}$. This indicates that the partial charge of the boron atom is less negative than those for the neighboring carbon atoms.

The spin resolved Unit-DOS shows the existence of unoccupied spin down states at the Fermi-energy on the pyrene unit (#2), thus confirming the p-type behavior. The HOMO is mostly localized on the pyrene but the other orbitals are all more or less delocalized. From the Unit-DOS one can also see the existence of a partially occupied band in the spin down channel close to the Fermi-energy.

Besides the problems in performing spin unrestricted calculations in VASP[50], doping a conjugated monolayer with open shell atoms might be an interesting option for the molecular engineering of magnetic monolayers. Such monolayers with spin polarized states near the Fermi-energy could be an intriguing alternative for the use in the field of organic spintronics, i.e. spin dependent charge transport in organic molecules.

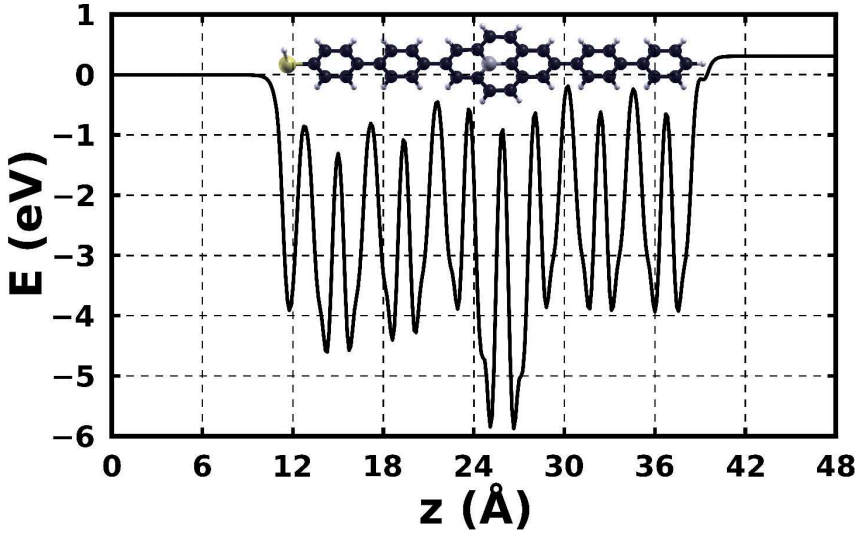

(a)

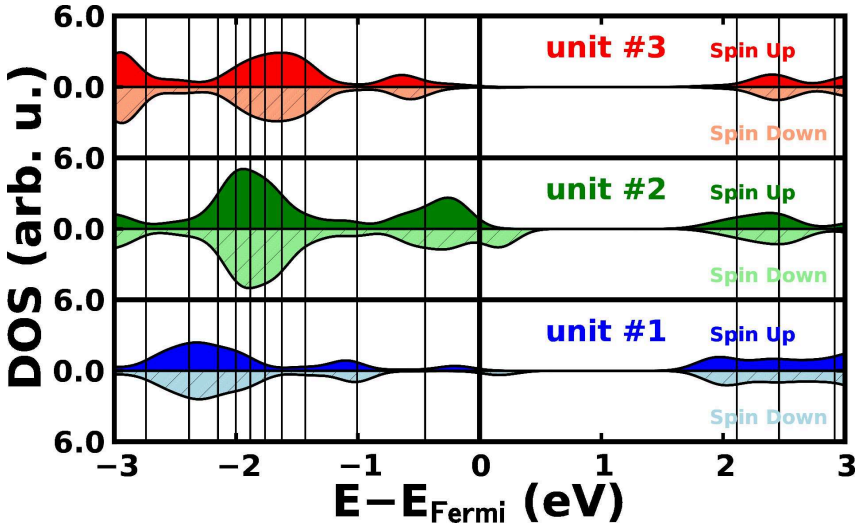

(b)

Figure 4.3.6: Electron potential energy (a) and spin resolved Unit-DOS (b) for the boron doped free-standing monolayer. The vertical lines indicate energy intervals containing two states. The numbering and coloring of the units follows the color code in the sketch of the chemical structure in Figure 4.3.1.

Chapter 5

Summary/Conclusions

In chapter 2 the way from a simple molecule to molecular quantum-well and cascade structures in self-assembled monolayers was portrayed. It was demonstrated that the shift of the highest occupied orbital of a free-standing monolayer is linearly dependent of the number of dipolar rings incorporated into the backbone. Due to the occurrence of Fermi-level pinning in SAMs on Au(111) with two or more dipolar rings the shifts did not show this linear behavior.

The investigation of structural effects revealed that they have a significant influence on the change of the vacuum energy and orbital shifts and, consequently, on the localization of the frontier orbitals in free-standing monolayers. The reason for the high influence of the molecular structure is that breaking the conjugation prevents the electron wave-functions from spreading out over the whole backbone. Consequently, local charge rearrangement can no longer counteract the dipole moment of the shifting unit.

The full optimization of the geometry of a SAM led to a worsening of the localization and orbital shifts, caused by the high tilt angle. A higher tilt angle leads to a smaller component of the dipole moment in -z-direction and, therefore, to smaller orbital shifts.

The comparison of the localization and orbital shifts in gas phase molecules and monolayers shows that these quantities get amplified in the monolayers due to collective electrostatic effects. While the orbitals are already localized in the gas phase molecule, the collective electrostatic effects occurring in a monolayer are important to build quantum-well structures since they trigger the necessary energetic separation of the orbitals.

When putting the monolayer on a metal substrate, interface related effects occur that have to be taken into account. An additional dipole at the interface occurs, which is able to influence the change of the work-function through the adsorbed monolayer significantly. Another important interface effect is the above mentioned Fermi-level pinning. These interface effects have also a significant influence on localization and orbital shifts.

Finally, the insights gained from the calculation on relatively simple systems allowed the designe of more complex quantum-well and cascade structures. These structures were realized by combining two dipolar elements within one backbone.

In chapter 3 the influences of different backbones and dipolar units was investigated. It could be shown that non-planar Tour-wire based backbones have the highest potential in terms of orbital shifts and localization of orbitals. For the purpose of building

quantum-well structures the planar Tour-wire based and the biphenyl backbones appeared as reasonable alternatives to the reference backbone discussed before. An interesting observation when computing different backbones was that the localization of the LUMO is very bad for planar backbones. The reason for this is the low-lying LUMO of the planar bipyrimidine. In contrast, the localization of the HOMO is quite good for the most of the tested backbones.

Besides the different backbones, also two different shifting units were tested: A conjugated one (bipyrimidine) and a non-conjugated one (bidioxane). In terms of orbital shifts and localization the bidioxane would be the better choice. The reason that a better localization and stronger orbital shifts can be reached with the bidioxane is the breaking of the conjugation. Additionally, the localization is improved by the relatively large band gap of the bidioxane unit. Molecules with bidioxane as shifting unit are not linear. Therefore, bipyrimidine was used as shifting unit for the most calculations.

The influence of spacer units and pyrene-based magnetic monolayers are discussed in chapter 4. It could be demonstrated that the introduction of a methyl spacer between the backbone and the thiol docking group can significantly reduce the influence of the substrate. Especially the spreading of metal states onto the first ring of the backbone can be prevented efficiently by the methyl spacer. The only disadvantage is that it can lead to an overlap of a pyrimidine σ-state with a thiol state, where the effect, however, very much depends on the backbone.

Two spacer units built in between the biphenyl backbone units and the bipyrimidine shifting unit were tested. These two were cyclohexane and magnesium. Both of which show a similar localization of the frontier orbitals. For comparison, the localization in systems with these two spacer units is not as good as in Tour-wire based monolayers with methyl substituents.

Finally, nitrogen and boron doped pyrene embedded into a molecule with biphenyl backbone was studied. Since the doping results in a molecule possessing an unpaired electron, the calculations have to be performed spin unrestricted. This can lead to severe complications when done in VASP[50], especially for the nitrogen doped monolayer. In subsection 4.3.1 some parameters are described that can help to obtain a consistent result. Property-wise the doping with nitrogen or boron leads to a magnetic monolayer with a partially filled band.

Appendix A

Tests

A.1 Old vs. new Potentials

At the beginning of this work some tests were performed with different versions of potentials for VASP[50]. The potentials termed as old ones here were released in 2003. The new potentials were released in 2012. All calculations in this section were performed with dipole correction. Both versions of the potentials were tested for different SAMs on metal substrate. The chemical structures of these SAMs are shown in Figure A.1.1.

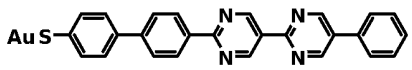

(a) AuSPh2Py2Ph

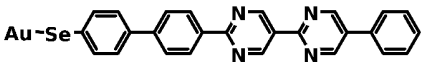

(b) AuSePh2Py2Ph

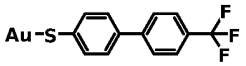

(c) Biphenylthiol+CF_3

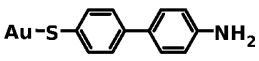

(d) Biphenylthiol+NH_2

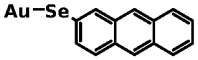

(e) Anthracenese-lenoid

Figure A.1.1: Chemical structures of tested SAMs

Table A.1: Convergence and work-function modifications for the different SAMs simulated with old and new potentials.

system	old potentials convergence (steps)	$\Delta\phi$ (eV)	new potentials convergence (steps)	$\Delta\phi$ (eV)
AuSPh2Py2Ph	45	0.38	60 (not converged)	-
AuSePh2Py2Ph	41	0.61	60 (not converged)	-
Biphenylthiol+CF_3	38	1.30	no convergence expected	-
Biphenylthiol+NH_2	29	-2.44	44	-2.47
Anthraceneselenoid	37	-1.37	35	-1.35

The results of these tests are summarized in Table A.1. This table shows the number of steps necessary to reach convergence and the work-function modifications for the systems where convergence was reached. If no convergence was reached after 60 steps in the SCF-cycle, two cases can be distinguished. In the first case, convergence may be reached by performing more steps, this case is indicated by "60 (not converged)" in Table A.1. In the other case no convergence is expected due to very high energy differences between the last steps. From Table A.1 one can see that this was the case only for *Biphenylthiol+CF_3*. For the first two listed systems convergence can be reached within 45 and 41 steps, respectively, when using the old potentials while the new ones would have needed more than 60 steps. In general, the old potentials seem to perform better in terms of convergence. Only for one system the new potentials converge faster than the old ones. For the cases in which both potentials converge within 60 steps, the work-function modifications and other results are virtually the same.

Since the systems simulated during this work show generally a bad convergence behavior, the old potentials were used since they seem to converge faster and with a higher reliability.

A.2 `ALGO` Tests

For the SAM on metal substrate with biphenyl backbone and bipyrimidine shifting unit in N_{down} configuration in a $\sqrt{3} \times 3$ unit cell tests with different algorithms for the electronic relaxation were performed. The standard calculation procedure consisting of a calculation without dipole correction followed by one with dipole correction was applied. The quantities for the comparison were the number of steps and the average time per step needed with and without dipole correction as well as the total energy and the work-function modifications at the end of the second part of the simulation. Most of the algorithms documented in the VASP-manual either do not work at all or do not lead to any result. The test results for the algorithms that worked and delivered reasonable results are shown in Table A.2. One can see that without dipole correction all algorithms need almost the same number of steps to reach convergence but the average time per step varies quite a lot. A similar observation is made for the calculation with dipole corrections except for `ALGO=All`. For the latter one the dipole moment was not converged and additional steps

would be necessary in this case. Very alarming is the fact that the choice of the algorithm has a significant influence on the work-function modification, even when the algorithm where the dipole moment is not converged is ignored.

Table A.2: Results of tests of different algorithms.

ALGO	without dipole correction		with dipole correction			
	steps	average time (s)	steps	average time (s)	E_{tot} (eV)	$\Delta\phi$ (eV)
Fast	25	324.98	21	267.23	-508.85646	-1.76
Normal	25	466.60	20	427.17	-508.85199	-1.95
All[1]	27	566.29	14	425.64	-508.84971	-2.21

[1]dipole moment is not converged

A.3 GADGET Test

For the SAM with Tour-wire based backbone with 6 side-chains in N_{down} configuration a geometry optimization was performed using GADGET[53]. To find a set of parameters which leads to the correct number of degrees of freedom and a correct substrate detection a lot of tests were made. In these tests the input parameters ascale, bscale, subst and the covalent radius of Gold were varied. The results are shown in Table A.3. The number of degrees of freedom should be 321. A smiley indicates correct results for the degrees of freedom and the substrate detection. For the substrate detection, an X marks wrong results and '—' display the tests done without substrate detection.

Table A.3: GADGET[53] tests

ascale	bscale	subst	covalent radius for Au	degrees of freedom	substrate detection
1.4	2	7	default	319	x
1.4	2	8	default	317	☺
1.5	2	8	default	317	x
1.4	1.6	6	default	319	x
1.4	1.6	7	default	319	x
1.4	1.7	6	default	319	x
1.4	1.8	6	default	319	x
1.4	1.9	6	default	☺ 321	x
1.4	1.9	7	default	319	x
1.4	1.9	8	default	317	☺
1.4	2	6	1.3	☺ 321	x
1.4	2	6	1.2	☺ 321	x
1.4	2	7	1.2	319	x
1.4	1.9	6	1.2	☺ 321	x
1.4	1.9	7	1.2	319	x
1.4	1.9	8	1.2	317	☺
1.4	1.9	8	1	317	x
1.3	1.9	6	1.2	311	x
1.5	1.9	6	1.2	☺ 321	x
1.5	1.9	8	1.2	317	x
1.3	2	6	default	311	☺
1.3	2	8	default	311	☺
1.3	2.1	6	default	311	☺
1.4	2.1	6	default	☺ 321	x
1.4	2	6	default	☺ 321	x
1.4	2.1	8	default	317	☺
1.4	2.1	6	1.2	☺ 321	x
1.3	2	6	1.2	311	☺
1.35	2	6	default	310	x
1.4	2	100	default	317	—
1.6	2	100	default	315	—
1.6	2.1	100	default	315	—
1.4	2.1	8	1.2	317	☺
1.6	2.1	8	1.2	☺ 321	x
1.6	2.1	9	1.2	315	x
1.8	2.1	10	1.2	☺ 321	x
1.8	2.1	100	1.2	☺ 321	—

A.4 Different Positions of the Dipole Jump

For this tests the cascade system in N_{down} configuration was used (see Figure A.4.1). For the first dipole jump test, the size of the unit cell in z-direction was varied in steps of 5 Å from 90 Å to 120 Å. Figure A.4.2 shows the electron potential energies for the different sizes of the unit cell in z-direction. The results have already been discussed in subsection 1.6.1. To summarize them, the work-function modification strongly depends on the size of the unit cell. The numerical values for the work-function modifications can be found in Table A.4. The difference between the highest and lowest work-function modification is about 0.70 eV.

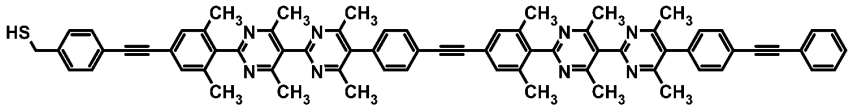

Figure A.4.1: Chemical structure of the cascade in N_{down} configuration.

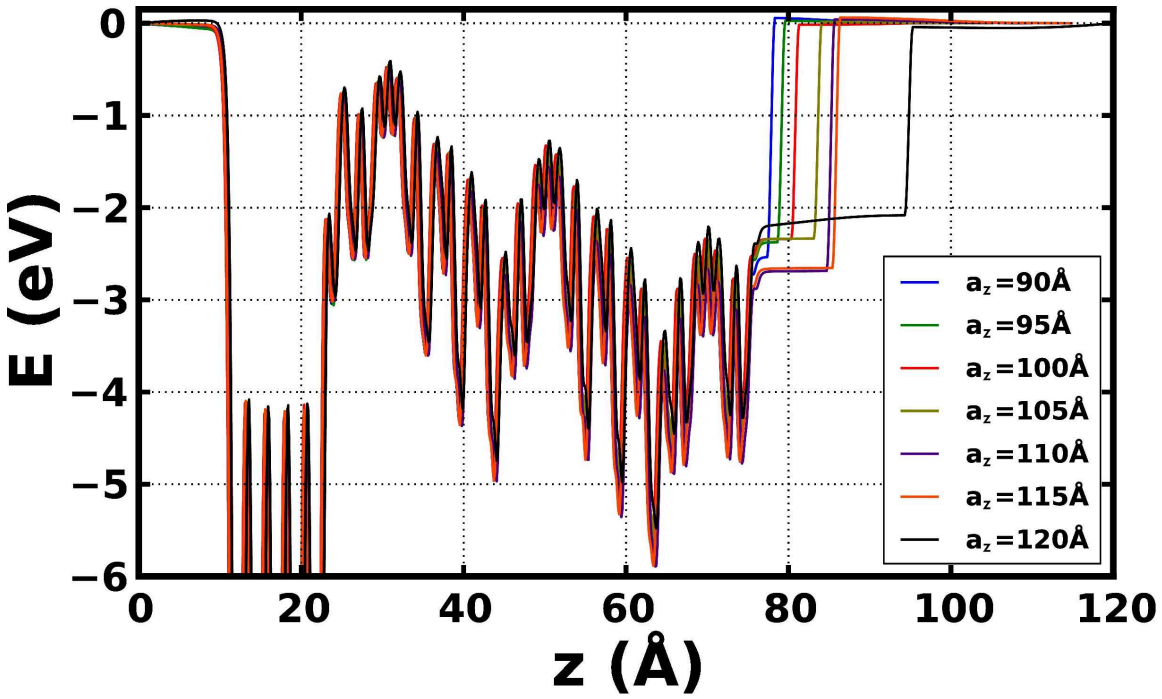

Figure A.4.2: Plane averaged electron potential energy for the cascade system for different sizes of the unit cell in z-direction.

Table A.4: Values of the work-function modifications $\Delta\varphi$ in dependence for different unit cell sizes in z-direction a_z.

a_z (Å)	$\Delta\varphi$ (eV)
90	-2.50
95	-2.42
100	-2.32
105	-2.35
110	-2.73
115	-2.70
120	-2.03

In the second test, the position of the dipole jump was set manually. VASP[50] provides a tag called `DIPOL` for this task.[52] This tag requires three floating point numbers between 0 and 1. They specify the position of the dipole jump in the three spatial directions in direct coordinates. Along the direction where the dipole correction is applied, VASP[50] adds half the corresponding unit cell vector to the given coordinate. The following line demonstrates the usage of the `DIPOL`-tag:

```
DIPOL = 0.27 0.46 0.25
```

In this example the dipole jump is set to 0.75 times the unit cell vector in z-direction. The x- and y-components of the `DIPOL`-tag were set to the approximate center of mass of the organic part. This was necessary to guarantee convergence. The size of the unit cell was chosen to be 110 Å for this test. The positions of the dipole jump were set between 82.5 Å and 104.5 Å. Figure A.4.3 shows the potential energies for the different positions of the dipole jump. When the dipole jump is too close to the molecule, the potential has a slight curvature around the dipole jump. The work-function modification varies quite a lot for the different positions of the dipole jump. Table A.5 lists the values for the work-function modification in dependence of the position of the dipole jump. The difference between the lowest and highest work-function modification is approximately 0.56 eV.

Table A.5: Values of the work-function modifications $\Delta\varphi$ in dependence of the position of the dipole jump z_{DP}.

z_{DP} (Å)	$\Delta\varphi$ (eV)
82.5	-1.64
88.0	-2.01
93.5	-1.84
99.0	-1.80
104.5	-2.20

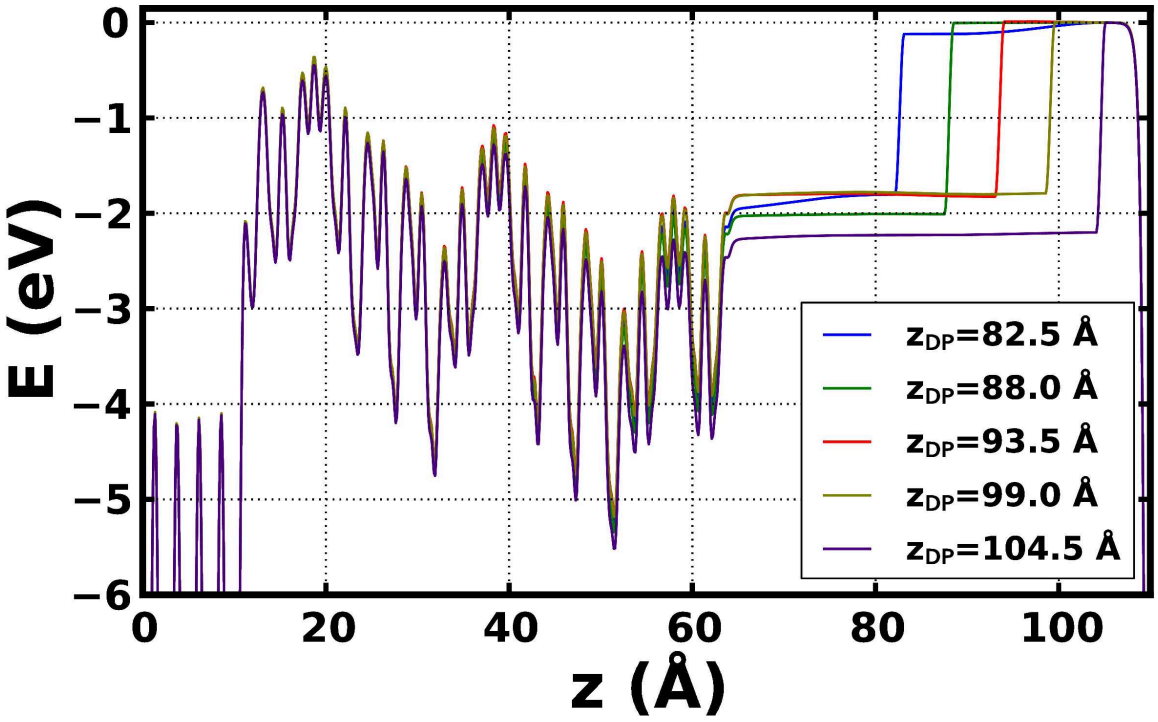

Figure A.4.3: Electron potential energies for the cascade system in a unit cell with $a_z = 110\,\text{Å}$ *for different positions of the dipole jump* z_{DP}.

Appendix B

Summary of used Input Parameters

B.1 VASP[50, 52]

All the information about the VASP[50] input parameters was obtained from the VASP user guide[52].

The following listing shows the standard `INCAR` file as it was used for the most calculations performed during this work:

Listing B.1: Standard `INCAR` file

```
 SYSTEM = x
 ENCUT = 273.894
 ISTART = 1
 ICHARG = 1
 NWRITE = 2
 PREC = Normal
 ISPIN = 1

Number of SCF cycles are left at their default values

 EDIFF = 1.E-04
 EDIFFG = -1E-02
 NELMIN = 8
 NSW = 1
 IBRION = -1
 POTIM = 0.08
 SMASS = 0.35
 ISIF = 0
 ISYM = 0


Flags for Pair-Correlation function output are set to
   default
```

```
LORBIT = 11
EMIN = -40.
EMAX = 20.
NEDOS = 5001
ISMEAR = 1
SIGMA = 0.2
LREAL = A
VOSKOWN = 1
ALGO = Fast
LDIAG = .TRUE.
LPLANE = .TRUE.
NSIM = 4
NPAR = 2

Mixing tags are left at their default values

LWAVE = .TRUE.
LCHARG = .TRUE.
LELF = .FALSE.
LVHAR = .TRUE.

IDIPOL = 0
LDIPOL = .FALSE.
```

Most of the parameters in the `INCAR` file have not been changed during this work. The ones that have been changed will be explained here shortly:

`ISPIN`: For spin restricted calculations this parameter needs to be set to 1 and for spin unrestricted calculations to 2.

`EDIFF`: This parameter represents the convergence criterion for the SCF-cycle. For single point calculations a value of 10^{-4} eV was used, for the geometry optimizations with GADGET[53] it was set to 10^{-6} eV.

`ISMEAR & SIGMA`: `ISMEAR` defines the method used for the broadening of the partial occupancies and `SIGMA` the width. For SAMs `ISMEAR` was set to 1 which selects a Methfessel-Paxton smearing method of first order. Free-standing monolayers and isolated molecules were simulated with a Gaussian smearing method (`ISMEAR` = 0). `SIGMA` was set to 0.2 unless stated otherwise.

`ALGO`: Selects the algorithm for the electronic relaxation. For single point calculations `Fast` was used and for GADGET[53] geometry calculations `Normal`.

`IDIPOL & LDIPOL`: Specify whether the dipole correction is used and for which direction. See subsection 1.6.1.

AMIN: A mixing parameter with a standard value of 0.1. For calculations with very large unit cells in z-direction this parameter was set to 0.01 to improve convergence.
Additionally different parameters for the calculation of the PDOS were used, namely `LPARD`, `IBAND`, `EINT` and `LSEPB`. These are explained in detail in subsection 1.6.2. For spin unrestricted calculations additional parameters were used (`MAGMOM`, `NUPDOWN`, ...). These are explained in subsection 4.3.1.

For GADGET[53] calculations the following lines were added to the `INCAR` file and `LREAL` was commented out:

```
ADDGRID=.TRUE.
LSCALAPACK=.FALSE.
#LREAL = A
```

ADDGRID: With this parameter set to .TRUE. VASP[50] uses an additional support grid to evaluate augmentation charges.

LSCALAPACK: Setting it to .FALSE. tells VASP[50] not to use scaLAPACK.

LREAL: Tells VASP[50] whether the projection operators should be evaluated in real space or in reciprocal space.

B.2 GADGET[53, 67]

The `INPDAT` file is used to specify the input parameters for GADGET[53] geometry optimizations. The standard version of this file is shown in the following listing:

Listing B.2: GADGET[53] standard `INPDAT` file

```
HESSIAN=3       # hessian initialised as a diag. matrix
   in cartesian (0),
                # internal coord.(1) space or as a model
                   hessian (2,3)

HUPDATE=1       # hessian-update formula, 0-no update,
   1-BFGS, 2-BFGS-TS, 3-SR1, 4-PSB,
                # 5-SR1/PSB, 6-SR1/BFGS
CART=0          # optimization in cartesians (1) or in
   delocalized internals (0)
GCRITER=0.000194469 # convergence criterion - maximal
   gradient in a.u.
SCRITER=5.02    # convergence criterion for geometry step
    (A)
ECRITER=1e-5    # convergence criterion - maximal energy
   change in a.u.
```

```
ASCALE=1.1      # scaling factor for automatic coordinate
    identification
BSCALE= 2.0     (additional scaling factor for covalent
   radii - only if more fragments are found i
FRAGCOORD= 2
RELAX=0
OPTENGINE=1     # engine for optimization (0-DIIS, 1-RFO)
NFREE=5
NSW = 1000
SUBST=6
POTIM=100
HSING=1.5e-4
```

The only parameters changed in this file were `ASCALE`, `BSCALE` and `SUBST`, see section A.3.

Appendix C

Uncommented Source Codes

C.1 Calculation of LDOS for consecutive Energy Intervals

This *Python* script starts VASP[50] calculations to compute the LDOS for consecutive energy intervals.

Listing C.1: Script to calculate the LDOS for consecutive energy intervals

```
1  #! /usr/bin/env python
2
3  import os
4  import sys
5  from math import fabs
6  import shutil
7  import subprocess
8  import time
9  from time import localtime, strftime
10
11 def main():
12
13     #get arguments
14     args = sys.argv
15
16     #test if correct number of arguments are given, if
           not: exit program
17     if len(args) != 5:
18         print 'Error␣1:␣4␣Arguments␣needed:␣E-min␣E-max␣
               deltaE␣ncores'
19         sys.exit(1)
20
21     #open logfile
22     log = open('System_PARCHG.log','a+')
23
```

```
24      #converting arguments from string to float
25      Emin = float(args[1])
26      Emax = float(args[2])
27      deltaE = float(args[3])
28      ncores = args[4]
29
30      #write arguments to logfile
31      log.write('E-min␣='+str(Emin)+'\n')
32      log.write('E-max␣='+str(Emax+deltaE)+'\n')
33      log.write('deltaE␣='+str(deltaE)+'\n')
34
35      cwd = os.getcwd()
36      #set starting energy i to Emin
37      i = Emin# + deltaE
38      while i < Emax:
39          #start with next energy intervall
40          act_time = strftime("%d-%m-%Y␣%H:%M:%S",
               localtime())
41          log.write(act_time)
42          log.write('*****************************\n')
43          log.write('Next␣energy␣intervall\n')
44
45          #create string for directory of current energy
               intervall
46          new_dir ='from'+str(i+deltaE)+'to'+str(i)
47          #copy Input directory to directory of current
               energy intervall
48          shutil.copytree('Input',new_dir+'/Input/')
49          log.flush()
50          #link WAVECAR to directory of current energy
               intervall
51          log.write('Linking␣WAVECAR␣to'+new_dir+'\n')
52          os.symlink(cwd+'/WAVECAR', new_dir+'/WAVECAR')
53
54          #adding necessary tags to INCAR file
55          log.write('Modifying␣INCAR\n')
56          os.chdir(new_dir+'/Input/')
57          f_incar = open('./INCAR', 'a')
58          f_incar.write('␣␣LPARD␣=␣.TRUE.\n')
59          f_incar.write('␣␣EINT␣=␣'+str(i)+'␣'+str(i+deltaE
               )+'\n')
60          f_incar.write('␣␣LWAVE=.FALSE.\n')
61          f_incar.write('␣␣LCHARG=.FALSE.\n')
62          f_incar.close()
63          os.chdir('..')
```

```
64
65          #copy files from Input directory to directory of
               current energy intervall
66          shutil.copy('Input/INCAR', '.')
67          shutil.copy('Input/KPOINTS', '.')
68          shutil.copy('Input/POSCAR', '.')
69          shutil.copy('Input/POTCAR', '.')
70
71          #start VASP
72          log.write('Starting␣VASP\n')
73          vasp = subprocess.Popen(["runvasp", new_dir,
               ncores])#, stdout=subprocess.PIPE)
74          log.write('Waiting␣for␣VASP\n')
75          log.flush()
76          sleep_time = 0
77          #test every 60 seconds if VASP still runs
78          vasp_runs = True
79          while vasp_runs:
80              time.sleep(60)                                  #
                   wait for 60 seconds
81              sleep_time += 60
82              try:
83                  f_out = open(new_dir+'.out', 'r')           #
                       open *out-file
84                  lines = f_out.readlines()
85                  if 'VASP␣will␣stop␣now' in lines[-1]:       #
                       if VASP stopped
86                      vasp_runs = False                       #
                           set vasp_runs to False
87                  f_out.close()                               #
                       close out-file
88              except Exception, e:                            #
                   if out-file doesn't exist an exception is
                   thrown
89                  pass                                        #
                       if out-file doesn't exist do nothing
90
91          #VASP has finished
92          log.write('Sleep␣time:␣'+str(sleep_time)+'\n')
93          log.flush()
94          #copy PARCHG from energy intervall directory to
               PARCHG-directory
95          shutil.copy('PARCHG', '../PARCHG.'+new_dir+'.ALLK
               ')
96          os.system('gzip␣*')
```

```
97          os.chdir('..')
98
99          #increas actual Energy i by deltaE
100         i = i +  deltaE
101
102     #done, close logfile
103     act_time = strftime("%d-%m-%Y␣%H:%M:%S", localtime())
104     log.write(act_time+'\n')
105     log.write('Done')
106     log.close()
107
108 if __name__ == "__main__":
109     sys.exit(main())
```

C.2 smear.f

This *Fortran* program is a python module which was compiled with *f2py*[68]. The purpose of this python module is to convolute the input data with a Gaussian function. The following listing shows the source code:

Listing C.2: Source code of smear.f

```
1           subroutine smear (sigma, lx, ly, lz, Z, smearedZ,
              Y)
2
3            double precision :: sigma, E
4            double precision, dimension(:,:) :: Z, smearedZ
5            double precision, dimension(:) :: Y
6
7            double precision :: temp,  g, c1, ex, dE
8            integer :: i, j, k
9            double precision, parameter :: pi = 3.1415927
10
11  Cf2py    intent(in) lx, ly, lz
12  Cf2py    intent(in) sigma, Z, dE
13  Cf2py    intent(inout) smearedZ
14
15           i=1
16           j=1
17           k=1
18
19           dE = abs(Y(1)-Y(ly))/ly
20           print *, dE
21           c1 = dE/(sigma*sqrt(2*pi))
22
```

```
23
24          do i=1, lx
25
26              do j=1, ly
27
28              E = Y(j)
29              temp = 0.0
30
31                  do k=1, lz
32
33                   ex=0.0
34                   ex=exp(-(E-Y(k))**2/(2*sigma**2))
35                   g=c1*ex
36                   temp = temp + Z(k,i)*g
37
38                  end do
39
40              smearedZ(j,i) = temp
41
42              end do
43
44          end do
45
46          end
```

C.3 LDOS Plot Script

The following python script reads in the LODS data, convolves it with a Gaussian function using the *Python* module *smear.f* and plots it:

Listing C.3: Source code of the LDOS plot script

```
1  #!/usr/bin/env python
2  # -*- coding: utf-8 -*-
3
4  import matplotlib
5  matplotlib.use('QT4Agg')
6
7  import sys
8  sys.path.append('/home/berni/Work/Stuff/python_modules')
9
10 import matplotlib.pyplot as plt
11
12 import os
13 import matplotlib.backends.backend_pdf
```

```
14 import numpy as np
15 from matplotlib import ticker, axes
16 import smear
17 from math import sqrt
18
19
20 def main():
21
22     E_fermi = -3.2 #actaully, in this case the chemical
          potentail
23
24     ymin = -3
25     ymax = 3
26
27     E_min = -6.2
28     E_akt = E_min
29     E_max = -0.2
30     delta_E = 0.1
31     N = 99
32     limit = 0.08
33     l_limit = 0.0#1
34     Z = []
35     X = []
36     Y = []
37
38     while E_akt < E_max:
39         fn = 'PARCHG.from'+str(E_akt+delta_E)+'to'+str(
              E_akt)+'.ALLK.dat'
40
41         f = open(fn, 'r')
42         l = f.readlines()
43         temp = []
44         for s in l:
45             t =  s.strip().split()
46             temp.append(float(t[1]))
47
48             if E_akt == E_min:
49                 X.append(float(t[0]))
50         k=0
51         i=E_akt
52         while i < (E_akt+delta_E-0.001):
53             Z.append(temp)
54             Y.append(round(i-E_fermi,4))
55             i += 0.01
56             k+=1
```

```
57          if k!= 10:
58              print 'Error: something bad happened!!! k=',
                    k
59          E_akt += delta_E
60
61
62      sigma = 0.1
63      slimit = 0.05
64      ly = len(Y)
65      lz = len(Z)
66      lx = len(X)
67      Zf = np.asfortranarray(Z)
68      Yf = np.asfortranarray(Y)
69      Zsf = np.asfortranarray(np.zeros((ly,lx)))
70
71
72      smear.smear(sigma, lx, ly, lz,Zf, Zsf, Yf)
73
74      for i in range(len(X)):
75          for j in range(len(Y)):
76
77              if Zsf[j][i] > slimit:
78                  Zsf[j][i] = slimit
79              if Zsf[j][i] < 0:
80                  Zsf[j][i] = 0.0
81
82
83
84      #set default font for mathtext to sans-serif
85      matplotlib.rc('mathtext', default='sf')
86
87      #set fontset for mathtext ti stixsans
88      matplotlib.rc('mathtext', fontset='stixsans')
89
90      #set distance between tick labels and axes to 10
            points
91          matplotlib.rc(('xtick.major','xtick.minor','ytick
                .major','ytick.minor'), pad='10')
92
93      font = {'family' : 'Arial',
94              'weight' : 'bold',
95              'size'   : 36}
96
97      font2 = {'family' : 'Arial',
98              'weight' : 'bold',
```

```
99              'size'   : 24}
100     font28 = {'family' : 'Arial',
101             'weight' : 'bold',
102             'size'   : 28}
103     c = [ 'b', 'g', 'r', 'Indigo', 'm', 'Gray', '
           OrangeRed', 'k']
104
105
106
107     fig1 = plt.figure(facecolor='white', frameon=True,
           figsize=(10.65,9), dpi=100)#figsize=(21.3,12), dpi
           =300)
108
109     ax1 = plt.axes()
110     plt.grid(True, linewidth=0.8, linestyle='--')
111     ax1.get_xaxis().tick_bottom() # Turn off ticks at top
            of plot
112
113     ax1.set_xticklabels([])
114
115     ax1.spines['bottom'].set_linewidth(4)
116     ax1.spines['top'].set_linewidth(4)
117     ax1.spines['left'].set_linewidth(4)
118     ax1.spines['right'].set_linewidth(4)
119
120     #set standard font
121     matplotlib.rc('font', **font2)
122
123     C = plt.contourf(X,Y,Zsf,N)#,cmap='gray_r')#, locator
           =ticker.LogLocator(base=5))#, levels=lev)
124     cbar =      plt.colorbar(C,orientation='horizontal',
           pad=0.03,shrink=0.85)#=0.75)
125     cbar.set_label(r'$\mathbf{\rho}$␣(e/'+ur'\u00c5'+')'
           ,**font)
126
127
128     zticks = np.arange(0,slimit+1,0.01)
129     zlabels = ['{0:0.2f}'.format(zticks[i]) for i in
           range(len(zticks))]
130
131
132     cbar.set_ticks(zticks)
133     cbar.ax.set_xticklabels(zlabels)
134
135     ax1.set_xlim(0.05,0.65)
```

```
136     ax1.set_ylim(ymin,ymax)
137
138     yticks = np.arange(ymin, ymax+0.1, 0.5)
139     ax1.set_yticks(yticks)
140     ax1.set_yticklabels([str(i) for i in yticks], **
          font28)
141     ax1.set_ylabel('E-$\mathbf{\mu}$'+ '␣(eV)', **font)
142
143     plt.subplots_adjust(left=0.143, right=0.983, bottom
          =0.15)
144     plt.show()
145         fig1.savefig('LDOS_Map_twb_CascadeNup_sigma'+str(
              sigma)+'.eps')#,bbox_inches='tight',pad_inches
              =0.2)
146
147     return 0
148
149 if __name__ == '__main__':
150     main()
```

Bibliography

[1] C. Joachim, J. K. Gimzewski, and A. Aviram. "Electronics using hybrid-molecular and mono-molecular devices." In: *Nature* 408.6812 (Nov. 2000), pp. 541–548. ISSN: 0028-0836. DOI: 10.1038/35046000. URL: http://dx.doi.org/10.1038/35046000.

[2] J. R. Heath and M. A. Ratner. "Molecular electronics." In: *Physics Today* May 2003 (2003), pp. 43–49.

[3] A. C. Whalley, M. L. Steigerwald, X. Guo, and C. Nuckolls. "Reversible Switching in Molecular Electronic Devices." In: *Journal of the American Chemical Society* 129.42 (Sept. 2007), pp. 12590–12591. ISSN: 0002-7863. DOI: 10.1021/ja073127y. URL: http://dx.doi.org/10.1021/ja073127y (visited on 02/24/2014).

[4] N. Holonyak, R. Kolbas, R. D. Dupuis, and P. D. Dapkus. "Quantum-well heterostructure lasers." In: *Quantum Electronics, IEEE Journal of* 16.2 (Feb. 1980), pp. 170–186. ISSN: 0018-9197. DOI: 10.1109/JQE.1980.1070447.

[5] J. Faist, F. Capasso, D. L. Sivco, C. Sirtori, A. L. Hutchinson, and A. Y. Cho. "Quantum Cascade Laser." In: *Science* 264.5158 (Apr. 1994), pp. 553–556. DOI: 10.1126/science.264.5158.553. URL: http://www.sciencemag.org/content/264/5158/553.abstract.

[6] Z.-y. Xie, T.-c. Wong, L.-S. Hung, and S.-t. Lee. "Transient electroluminescence of organic quantum-well light-emitting diodes." In: *Applied Physics Letters* 80.8 (2002), pp. 1477–1479. DOI: http://dx.doi.org/10.1063/1.1450248. URL: http://scitation.aip.org/content/aip/journal/apl/80/8/10.1063/1.1450248.

[7] A. Danilov, S. Kubatkin, S. Kafanov, P. Hedegard, N. Stuhr-Hansen, K. Moth-Poulsen, and T. Bjornholm. "Electronic Transport in Single Molecule Junctions: Control of the Molecule-Electrode Coupling through Intramolecular Tunneling Barriers." In: *Nano Letters* 8.1 (Dec. 2007), pp. 1–5. ISSN: 1530-6984. DOI: 10.1021/nl071228o. URL: http://dx.doi.org/10.1021/nl071228o (visited on 12/10/2013).

[8] A. Aviram and M. A. Ratner. "Molecular rectifiers." In: *Chemical Physics Letters* 29.2 (Nov. 1974), pp. 277–283. ISSN: 0009-2614. DOI: 10.1016/0009-2614(74)85031-1. URL: http://www.sciencedirect.com/science/article/pii/0009261474850311.

[9] H. Nakamura, Y. Asai, J. Hihath, C. Bruot, and N. Tao. "Switch of Conducting Orbital by Bias-Induced Electronic Contact Asymmetry in a Bipyrimidinyl-biphenyl Diblock Molecule: Mechanism to Achieve a pn Directional Molecular Diode." In: *The Journal of Physical Chemistry C* 115.40 (Sept. 2011), pp. 19931–19938. ISSN: 1932-7447. DOI: 10.1021/jp205723g. URL: http://dx.doi.org/10.1021/jp205723g (visited on 11/21/2013).

[10] G.-P. Zhang, G.-C. Hu, Y. Song, Z.-L. Li, and C.-K. Wang. "Modulation of Rectification in Diblock Co-oligomer Diodes by Adjusting Anchoring Groups for Both Symmetric and Asymmetric Electrodes." In: *The Journal of Physical Chemistry C* 116.41 (Sept. 2012), pp. 22009–22014. ISSN: 1932-7447. DOI: 10.1021/jp304890p. URL: http://dx.doi.org/10.1021/jp304890p (visited on 11/21/2013).

[11] J. M. Tour, M. Kozaki, and J. M. Seminario. "Molecular Scale Electronics: A Synthetic/Computational Approach to Digital Computing." In: *Journal of the American Chemical Society* 120.33 (Aug. 1998), pp. 8486–8493. ISSN: 0002-7863. DOI: 10.1021/ja9808090. URL: http://dx.doi.org/10.1021/ja9808090 (visited on 11/18/2013).

[12] P. E. Burrows and S. R. Forrest. "Direct observation of ordered crystalline organic quantum-well structures using reflection high-energy electron diffraction." In: *Applied Physics Letters* 62.24 (1993), pp. 3102–3104. DOI: http://dx.doi.org/10.1063/1.109151. URL: http://scitation.aip.org/content/aip/journal/apl/62/24/10.1063/1.109151.

[13] L. Yingkui. "Nondoped phosphorescent organic quantum well light-emitting device based on iridium complex: Synthesis, characterization, photophysical property, and electroluminescence performance." In: *Journal of Luminescence* 131.9 (Sept. 2011), pp. 1821–1826. ISSN: 0022-2313. DOI: 10.1016/j.jlumin.2011.04.048. URL: http://www.sciencedirect.com/science/article/pii/S0022231311002511.

[14] L. Wen, F. Li, and T. Guo. "White organic light-emitting diode based on organic quantum well structure." English. In: *Materials Science Forum* 694 (2011). INSPEC:12989698, pp. 645–649. ISSN: 0255-5476. DOI: 10.4028/www.scientific.net/MSF.694.645.

[15] S.-H. Yang, B.-C. Hong, and S.-F. Huang. "Luminescence enhancement and emission color adjustment of white organic light-emitting diodes with quantum-well-like structures." In: *Journal of Applied Physics* 105.11 (2009), pp. –. DOI: http://dx.doi.org/10.1063/1.3138810. URL: http://scitation.aip.org/content/aip/journal/jap/105/11/10.1063/1.3138810.

[16] E. R. Bittner and C. Silva. "Estimating the conditions for polariton condensation in organic thin-film microcavities." In: *The Journal of Chemical Physics* 136.3 (2012), pp. –. DOI: http://dx.doi.org/10.1063/1.3678015. URL: http://scitation.aip.org/content/aip/journal/jcp/136/3/10.1063/1.3678015.

[17] D. Niedzialek, V. Lemaur, D. Dudenko, J. Shu, M. R. Hansen, J. W. Andreasen, W. Pisula, K. Müllen, J. Cornil, and D. Beljonne. "Probing the Relation Between Charge Transport and Supramolecular Organization Down to Ångström Resolution in a Benzothiadiazole-Cyclopentadithiophene Copolymer." In: *Advanced Materials* 25.13 (2013), pp. 1939–1947. ISSN: 1521-4095. DOI: 10.1002/adma.201201058. URL: http://dx.doi.org/10.1002/adma.201201058.

[18] C. D. Canestraro, P. C. Rodrigues, C. F. Marchiori, C. B. Schneider, L. Akcelrud, M. Koehler, and L. S. Roman. "The role of the double peaked absorption spectrum in the efficiency of solar cells based on donor–acceptor–donor copolymers." In: *Photovoltaics, Solar Energy Materials & Thin Films, IMRC 2009-Cancun* 95.8 (Aug. 2011), pp. 2287–2294. ISSN: 0927-0248. DOI: 10.1016/j.solmat.2011.03.043. URL: http://www.sciencedirect.com/science/article/pii/S0927024811001966.

[19] J. Cornil, I. Gueli, A. Dkhissi, J. C. Sancho-Garcia, E. Hennebicq, J. P. Calbert, V. Lemaur, D. Beljonne, and J. L. Brédas. "Electronic and optical properties of polyfluorene and fluorene-based copolymers: A quantum-chemical characterization." In: *The Journal of Chemical Physics* 118.14 (2003), pp. 6615–6623. DOI: http://dx.doi.org/10.1063/1.1561054. URL: http://scitation.aip.org/content/aip/journal/jcp/118/14/10.1063/1.1561054.

[20] J. W. Colson, A. R. Woll, A. Mukherjee, M. P. Levendorf, E. L. Spitler, V. B. Shields, M. G. Spencer, J. Park, and W. R. Dichtel. "Oriented 2D Covalent Organic Framework Thin Films on Single-Layer Graphene." In: *Science* 332.6026 (Apr. 2011), pp. 228–231. DOI: 10.1126/science.1202747. URL: http://www.sciencemag.org/content/332/6026/228.abstract.

[21] Y. Zhou, Z. Wang, P. Yang, X. Zu, and F. Gao. "Electronic and optical properties of two-dimensional covalent organic frameworks." In: *Journal of Materials Chemistry* 22.33 (2012), pp. 16964–16970. ISSN: 0959-9428. DOI: 10.1039/C2JM32321D. URL: http://dx.doi.org/10.1039/C2JM32321D.

[22] Z. Wu, J. B. Neaton, and J. C. Grossman. "Quantum Confinement and Electronic Properties of Tapered Silicon Nanowires." In: *Physical Review Letters* 100.24 (June 2008), p. 246804. URL: http://link.aps.org/doi/10.1103/PhysRevLett.100.246804.

[23] Z. Wu, J. B. Neaton, and J. C. Grossman. "Charge Separation via Strain in Silicon Nanowires." In: *Nano Letters* 9.6 (2009), pp. 2418–2422. ISSN: 1530-6984. DOI: 10.1021/nl9010854. URL: http://dx.doi.org/10.1021/nl9010854 (visited on 11/18/2013).

[24] Z. Wu and J. C. Grossman. "Prediction of Ultra-High Aspect Ratio Nanowires from Self-Assembly." In: *Nano Letters* 8.9 (Aug. 2008), pp. 2697–2705. ISSN: 1530-6984. DOI: 10.1021/nl801025c. URL: http://dx.doi.org/10.1021/nl801025c (visited on 12/09/2013).

[25] C. Cocchi, D. Prezzi, A. Ruini, M. J. Caldas, and E. Molinari. "Electronics and Optics of Graphene Nanoflakes: Edge Functionalization and Structural Distortions." In: *The Journal of Physical Chemistry C* 116.33 (July 2012), pp. 17328–17335. ISSN: 1932-7447. DOI: 10.1021/jp300657k. URL: http://dx.doi.org/10.1021/jp300657k (visited on 11/20/2013).

[26] F. Rissner, D. A. Egger, A. Natan, T. Körzdörfer, S. Kümmel, L. Kronik, and E. Zojer. "Collectively Induced Quantum-Confined Stark Effect in Monolayers of Molecules Consisting of Polar Repeating Units." In: *Journal of the American Chemical Society* 133.46 (Sept. 2011), pp. 18634–18645. ISSN: 0002-7863. DOI: 10.1021/ja203579c. URL: http://dx.doi.org/10.1021/ja203579c (visited on 12/05/2013).

[27] F. Rissner, A. Natan, D. A. Egger, O. T. Hofmann, L. Kronik, and E. Zojer. "Dimensionality effects in the electronic structure of organic semiconductors consisting of polar repeat units." In: *Organic Electronics* 13.12 (Dec. 2012), pp. 3165–3176. ISSN: 1566-1199. DOI: 10.1016/j.orgel.2012.09.003. URL: http://www.sciencedirect.com/science/article/pii/S156611991200417X.

[28] M. L. Sushko and A. L. Shluger. "Intramolecular Dipole Coupling and Depolarization in Self-Assembled Monolayers." In: *Advanced Functional Materials* 18.15 (2008), pp. 2228–2236. ISSN: 1616-3028. DOI: 10.1002/adfm.200701305. URL: http://dx.doi.org/10.1002/adfm.200701305.

[29] O. M. Cabarcos, A. Shaporenko, T. Weidner, S. Uppili, L. S. Dake, M. Zharnikov, and D. L. Allara. "Physical and Electronic Structure Effects of Embedded Dipoles in Self-Assembled Monolayers: Characterization of Mid-Chain Ester Functionalized Alkanethiols on Au{111}." In: *The Journal of Physical Chemistry C* 112.29 (June 2008), pp. 10842–10854. ISSN: 1932-7447. DOI: 10.1021/jp801618j. URL: http://dx.doi.org/10.1021/jp801618j (visited on 12/05/2013).

[30] G. Heimel, I. Salzmann, S. Duhm, and N. Koch. "Design of Organic Semiconductors from Molecular Electrostatics†." In: *Chemistry of Materials* 23.3 (2011), pp. 359–377. ISSN: 0897-4756. DOI: 10.1021/cm1021257. URL: http://dx.doi.org/10.1021/cm1021257 (visited on 11/21/2013).

[31] S. Duhm, G. Heimel, I. Salzmann, H. Glowatzki, R. L. Johnson, A. Vollmer, J. P. Rabe, and N. Koch. "Orientation-dependent ionization energies and interface dipoles in ordered molecular assemblies." In: *Nat Mater* 7.4 (Apr. 2008), pp. 326–332. ISSN: 1476-1122. DOI: 10.1038/nmat2119. URL: http://dx.doi.org/10.1038/nmat2119.

[32] I. Salzmann, S. Duhm, G. Heimel, M. Oehzelt, R. Kniprath, R. L. Johnson, J. P. Rabe, and N. Koch. "Tuning the Ionization Energy of Organic Semiconductor Films: The Role of Intramolecular Polar Bonds." In: *Journal of the American Chemical Society* 130.39 (Sept. 2008), pp. 12870–12871. ISSN: 0002-7863. DOI: 10.1021/ja804793a. URL: http://dx.doi.org/10.1021/ja804793a (visited on 11/21/2013).

[33] G. Heimel, I. Salzmann, S. Duhm, J. P. Rabe, and N. Koch. "Intrinsic Surface Dipoles Control the Energy Levels of Conjugated Polymers." In: *Advanced Functional Materials* 19.24 (2009), pp. 3874–3879. ISSN: 1616-3028. DOI: 10.1002/adfm.200901025. URL: http://dx.doi.org/10.1002/adfm.200901025.

[34] Y. Selzer, L. Cai, M. A. Cabassi, Y. Yao, J. M. Tour, T. S. Mayer, and D. L. Allara. "Effect of Local Environment on Molecular Conduction: Isolated Molecule versus Self-Assembled Monolayer." In: *Nano Letters* 5.1 (Dec. 2004), pp. 61–65. ISSN: 1530-6984. DOI: 10.1021/nl048372j. URL: http://dx.doi.org/10.1021/nl048372j (visited on 11/21/2013).

[35] M. G. Reuter, T. Seideman, and M. A. Ratner. "Molecular Conduction through Adlayers: Cooperative Effects Can Help or Hamper Electron Transport." In: *Nano Letters* 11.11 (Oct. 2011), pp. 4693–4696. ISSN: 1530-6984. DOI: 10.1021/nl202342a. URL: http://dx.doi.org/10.1021/nl202342a (visited on 11/21/2013).

[36] M. G. Reuter, G. C. Solomon, T. Hansen, T. Seideman, and M. A. Ratner. "Understanding and Controlling Crosstalk between Parallel Molecular Wires." In: *The Journal of Physical Chemistry Letters* 2.14 (June 2011), pp. 1667–1671. ISSN: 1948-7185. DOI: 10.1021/jz200658h. URL: http://dx.doi.org/10.1021/jz200658h (visited on 11/21/2013).

[37] M. G. Reuter, M. C. Hersam, T. Seideman, and M. A. Ratner. "Signatures of Cooperative Effects and Transport Mechanisms in Conductance Histograms." In: *Nano Letters* 12.5 (Apr. 2012), pp. 2243–2248. ISSN: 1530-6984. DOI: 10.1021/nl204379j. URL: http://dx.doi.org/10.1021/nl204379j (visited on 11/21/2013).

[38] M. Galperin and A. Nitzan. "Cooperative Effects in Inelastic Tunneling." In: *The Journal of Physical Chemistry B* 117.16 (Oct. 2012), pp. 4449–4453. ISSN: 1520-6106. DOI: 10.1021/jp308222q. URL: http://dx.doi.org/10.1021/jp308222q (visited on 11/21/2013).

[39] Vazquez H., Skouta R., Schneebeli S., Kamenetska M., Breslow R., Venkataraman L., and Hybertsen M.S. "Probing the conductance superposition law in single-molecule circuits with parallel paths." In: *Nat Nano* 7.10 (Oct. 2012), pp. 663–667. ISSN: 1748-3387. DOI: 10.1038/nnano.2012.147. URL: http://dx.doi.org/10.1038/nnano.2012.147.

[40] D. A. Egger, F. Rissner, E. Zojer, and G. Heimel. "Polarity Switching of Charge Transport and Thermoelectricity in Self-Assembled Monolayer Devices." In: *Advanced Materials* 24.32 (Aug. 2012), pp. 4403–4407. ISSN: 1521-4095. DOI: 10.1002/adma.201200872. URL: http://dx.doi.org/10.1002/adma.201200872.

[41] D. Cahen, R. Naaman, and Z. Vager. "The Cooperative Molecular Field Effect." In: *Advanced Functional Materials* 15.10 (2005), pp. 1571–1578. ISSN: 1616-3028. DOI: 10.1002/adfm.200500187. URL: http://dx.doi.org/10.1002/adfm.200500187.

[42] M. J. Frisch, G. W. Trucks, H. B. Schlegel, G. E. Scuseria, M. A. Robb, J. R. Cheeseman, J. A. Montgomery Jr., T. Vreven, K. N. Kudin, J. C. Burant, J. M. Millam, S. S. Iyengar, J. Tomasi, V. Barone, B. Mennucci, M. Cossi, G. Scalmani, N. Rega, G. A. Petersson, H. Nakatsuji, M. Hada, M. Ehara, K. Toyota, R. Fukuda, J. Hasegawa, M. Ishida, T. Nakajima, Y. Honda, O. Kitao, H. Nakai, M. Klene, X. Li, J. E. Knox, H. P. Hratchian, J. B. Cross, V. Bakken, C. Adamo, J. Jaramillo, R. Gomperts, R. E. Stratmann, O. Yazyev, A. J. Austin, R. Cammi, C. Pomelli, J. W. Ochterski, P. Y. Ayala, K. Morokuma, G. A. Voth, P. Salvador, J. J. Dannenberg, V. G. Zakrzewski, S. Dapprich, A. D. Daniels, M. C. Strain, O. Farkas, D. K. Malick, A. D. Rabuck, K. Raghavachari, J. B. Foresman, J. V. Ortiz, Q. Cui, A. G. Baboul, S. Clifford, J. Cioslowski, B. B. Stefanov, G. Liu, A. Liashenko, P. Piskorz, I. Komaromi, R. L. Martin, D. J. Fox, T. Keith, M. A. Al-Laham, C. Y. Peng, A. Nanayakkara, M. Challacombe, P. M. W. Gill, B. Johnson, W. Chen, M. W. Wong, C. Gonzalez, and J. A. Pople. *Gaussian 03, Revision C.02*. Gaussian, Inc., Wallingford, CT, 2004.

[43] J. P. Perdew, K. Burke, and M. Ernzerhof. "Generalized Gradient Approximation Made Simple." In: *Physical Review Letters* 77.18 (Oct. 1996), pp. 3865–3868. URL: http://link.aps.org/doi/10.1103/PhysRevLett.77.3865.

[44] G. Heimel, E. Zojer, L. Romaner, J.-L. Brédas, and F. Stellacci. "Doping Molecular Wires." In: *Nano Letters* 9.7 (July 2009), pp. 2559–2564. ISSN: 1530-6984. DOI: 10.1021/nl9006613. URL: http://dx.doi.org/10.1021/nl9006613 (visited on 11/22/2012).

[45] Z. Ma, F. Rissner, L. Wang, G. Heimel, Q. Li, Z. Shuai, and E. Zojer. "Electronic structure of pyridine-based SAMs on flat Au(111) surfaces: extended charge rearrangements and Fermi level pinning." In: *Physical Chemistry Chemical Physics* 13.20 (2011), pp. 9747–9760. ISSN: 1463-9076. DOI: 10.1039/C0CP02168G. URL: http://dx.doi.org/10.1039/C0CP02168G.

[46] R. M. Martin. *Electronic structure: basic theory and practical methods*. Cambridge university press, 2004. ISBN: 0521782856.

[47] P. Hohenberg and W. Kohn. "Inhomogeneous Electron Gas." In: *Physical Review* 136.3B (Nov. 1964), B864–B871. URL: http://link.aps.org/doi/10.1103/PhysRev.136.B864.

[48] W. Kohn and L. J. Sham. "Self-Consistent Equations Including Exchange and Correlation Effects." In: *Physical Review* 140.4A (Nov. 1965), A1133–A1138. URL: http://link.aps.org/doi/10.1103/PhysRev.140.A1133.

[49] G. Heimel, F. Rissner, and E. Zojer. "Modeling the Electronic Properties of π-Conjugated Self-Assembled Monolayers." In: *Advanced Materials* 22.23 (2010), pp. 2494–2513. ISSN: 1521-4095. DOI: 10.1002/adma.200903855. URL: http://dx.doi.org/10.1002/adma.200903855.

[50] G. Kresse and J. Hafner. "Ab initio molecular dynamics for liquid metals." In: *Physical Review B* 47.1 (Jan. 1993), pp. 558–561. URL: http://link.aps.org/doi/10.1103/PhysRevB.47.558.

[51] Æ. Frisch, M. J. Frisch, and G. W. Trucks. *Gaussian 03 user's reference*. Gaussian, Incorporated, 2003. ISBN: 0972718702.

[52] G. Kresse, M. Marsman, and J. Furthmüller. *VASP the GUIDE*. Computational Physics, Faculty of Physics, Universität Wien, Sensengasse 8, A-1130 Wien, Austria. Sept. 2013. URL: http://cms.mpi.univie.ac.at/vasp/vasp/vasp.html (visited on 01/07/2014).

[53] T. Bučko, J. Hafner, and J. G. Ángyán. "Geometry optimization of periodic systems using internal coordinates." In: *The Journal of Chemical Physics* 122.12 (2005), pp. –. DOI: http://dx.doi.org/10.1063/1.1864932. URL: http://scitation.aip.org/content/aip/journal/jcp/122/12/10.1063/1.1864932;jsessionid=3dl7c6mspn7wm.x-aip-live-01.

[54] P. Császár and P. Pulay. "Geometry optimization by direct inversion in the iterative subspace." In: *Journal of Molecular Structure* 114.0 (1984), pp. 31–34. ISSN: 0022-2860. DOI: 10.1016/S0022-2860(84)87198-7. URL: http://www.sciencedirect.com/science/article/pii/S0022286084871987.

[55] Ö. Farkas and H. B. Schlegel. "Methods for optimizing large molecules. Part III. An improved algorithm for geometry optimization using direct inversion in the iterative subspace (GDIIS)." In: *Physical Chemistry Chemical Physics* 4.1 (Jan. 2002), pp. 11–15. ISSN: 1463-9084. DOI: 10.1039/B108658H. URL: http://pubs.rsc.org/en/content/articlelanding/2002/cp/b108658h (visited on 12/06/2012).

[56] A. Banerjee, N. Adams, J. Simons, and R. Shepard. "Search for stationary points on surfaces." In: *The Journal of Physical Chemistry* 89.1 (Jan. 1985), pp. 52–57. ISSN: 0022-3654. DOI: 10.1021/j100247a015. URL: http://dx.doi.org/10.1021/j100247a015 (visited on 03/18/2014).

[57] Ö. Farkas and H. B. Schlegel. "Methods for optimizing large molecules. II. Quadratic search." In: *The Journal of Chemical Physics* 111.24 (Dec. 1999), pp. 10806–10814. ISSN: 00219606. DOI: doi:10.1063/1.480484. URL: http://jcp.aip.org/resource/1/jcpsa6/v111/i24/p10806_s1 (visited on 12/06/2012).

[58] *p4VASP*. URL: http://www.p4vasp.at/ (visited on 02/20/2014).

[59] A. Kokalj. "Computer graphics and graphical user interfaces as tools in simulations of matter at the atomic scale." In: *Proceedings of the Symposium on Software Development for Process and Materials Design* 28.2 (Oct. 2003), pp. 155–168. ISSN: 0927-0256. DOI: 10.1016/S0927-0256(03)00104-6. URL: http://www.sciencedirect.com/science/article/pii/S0927025603001046.

[60] J. D. Hunter. "Matplotlib: A 2D graphics environment." In: *Computing In Science & Engineering* 9.3 (2007), 90–95.

[61] E. Jones, T. Oliphant, P. Peterson, et al. *SciPy: Open source scientific tools for Python*. 2001. URL: http://www.scipy.org/.

[62] T. E. Oliphant. "Python for Scientific Computing." In: *Computing in Science & Engineering* 9.3 (2007), pp. 10–20. DOI: http://dx.doi.org/10.1109/MCSE.2007.58. URL: http://scitation.aip.org/content/aip/journal/cise/9/3/10.1109/MCSE.2007.58;jsessionid=2ab7h7pe2u7fm.x-aip-live-01.

[63] L. Segev, A. Salomon, A. Natan, D. Cahen, L. Kronik, F. Amy, C. K. Chan, and A. Kahn. "Electronic structure of Si(111)-bound alkyl monolayers: Theory and experiment." In: *Physical Review B* 74.16 (Oct. 2006), p. 165323. URL: http://link.aps.org/doi/10.1103/PhysRevB.74.165323.

[64] D. J. Nelson and C. N. Brammer. "Toward Consistent Terminology for Cyclohexane Conformers in Introductory Organic Chemistry." In: *Journal of Chemical Education* 88.3 (Dec. 2010), pp. 292–294. ISSN: 0021-9584. DOI: 10.1021/ed100172k. URL: http://dx.doi.org/10.1021/ed100172k (visited on 01/18/2014).

[65] S. Atul. *IIT Chemistry: Introductory Topics*. Pearson Education India, 2010. ISBN: 978-81-317-3330-1.

[66] M. Gruber, G. Heimel, L. Romaner, J.-L. Brédas, and E. Zojer. "First-principles study of the geometric and electronic structure of Au13 clusters: Importance of the prism motif." In: *Phys. Rev. B* 77.16 (Apr. 2008), p. 165411. DOI: 10.1103/PhysRevB.77.165411. URL: http://link.aps.org/doi/10.1103/PhysRevB.77.165411.

[67] Ferdinand Rissner. "SAM-Induced Work Function Modification and Energy-Level Alignment at the Interface between Organic Semiconductors." Diploma Thesis. Graz, Austria: Graz University of Technology, Feb. 2009.

[68] P. Peterson. "F2PY: a tool for connecting Fortran and Python programs." In: *Int. J. Comput. Sci. Eng.* 4.4 (2009), pp. 296–305.